7-2021

Experimental and Analysis of Electromagnetic Characterization of Biological and Non-Biological Materials in Microwave, Millimeter-wave, and Terahertz Frequency Bands

Nagma Vohra
University of Arkansas, Fayetteville

Experimental and Analysis of Electromagnetic Characterization of Biological and Non-Biological Materials in Microwave, Millimeter-wave, and Terahertz Frequency Bands

A dissertation submitted in partial fulfillment
of the requirements for the degree of
Doctor of Philosophy in Engineering
with a concentration in Electrical Engineering

by

Nagma Vohra
Guru Nanak Dev University
Bachelor of Technology in Electronics and Communication Engineering, 2014
Vellore Institute of Technology
Master of Technology in Communication Engineering, 2017

July 2021
University of Arkansas

This dissertation is approved for recommendation to the Graduate Council.

Magda El-Shenawee, Ph.D.
Dissertation Director

Jingxian Wu, Ph.D.
Committee Member

Narasimhan Rajaram, Ph.D.
Committee Member

Zhong Chen, Ph.D.
Committee Member

ABSTRACT

The goal of this research is to characterize the electromagnetic properties of biological and non-biological materials at terahertz (THz), millimeter-wave, and microwave frequency bands. The biological specimens are measured using the THz imaging and spectroscopy system, whereas the non-biological materials are measured using the microwave and millimeter-wave free-space system. These facilities are located in the Engineering Research Center at the University of Arkansas. The THz imaging system (TPS 3000) uses a Ti-Sapphire laser directed on the photoconductive antennas to generate a THz time domain pulse. Upon using the Fourier Transform, the spectrum of the pulsed THz signal includes frequencies from 0.1 THz to 4 THz. On the other hand, the free space system uses a PNA network analyzer to produce a signal at frequencies ranging from 10 MHz to 110 GHz.

For the biological specimens, the research focused on imaging the freshly excised breast tumors to detect the cancer on the margins using THz radiation. The tumor margin assessment depends on the THz contrast between cancer, collagen, and fat tissues in the tumor. Three models of breast tumors are investigated in this research: humans, mice (xenograft and transgenic), and Sprague Dawley rats. The results showed good differentiation between the cancerous and non-cancerous tissues in all three models. In addition, an excellent distinction was observed between cancer, collagen, and fat in the formalin-fixed paraffin-embedded (FFPE) block tissue with ~ 90-95% correlation with the pathology images. Furthermore, the FFPE ductal carcinoma in situ (DCIS) tumors are investigated, also using the THz imaging. The THz images of the DCIS samples are compared with those of the FFPE invasive ductal carcinoma (IDC) specimens. The results demonstrated that THz electric field reflection from the IDC were higher than that from the collagen, DCIS, and then the fat tissue region.

Furthermore, a pilot study is conducted to investigate the effect of optical clearance (e.g., glycerol solution) on THz images of freshly excised tumors. The results showed that the glycerol reduced the absorption coefficients of pre-treated tissues compared with those of untreated tissues.

For the non-biological materials, the research focuses on characterizing highly conductive non-magnetic radar absorbing materials (RAM) for the automotive industry. The ingredients of material components in the RAM samples are unrevealed under a non-disclosure agreement (NDA). The material characterization involves the extraction of the complex relative permittivity utilizing the transmission measurement data obtained at the *K*-band (18 GHz to 26.5 GHz) and the *W*-band (75 GHz to 110 GHz). The measurements are obtained using the free-space conical horn antenna system. A transmission line based extraction model is implemented, and the results are validated with the experimental measurements of the S-parameters. The maximum error reported between the measured and the calculated S-parameters was less than 1 dB.

In conclusion, the THz imaging of breast cancer tumors presents a potential margin assessment of other solid tumors, and the microwave, millimeter-wave, and THz spectroscopy of materials demonstrate a potential application in the fifth and sixth generations of wireless communications.

ACKNOWLEDGEMENTS

The terahertz imaging and spectroscopy work for breast cancer tumors is funded by the National Institutes of Health (NIH) award no. R15CA208798 for the project titled "Terahertz Imaging for Margin Assessment of Three Dimensional Breast Cancer Tumors," led by Dr. Magda El-Shenawee (PI), with Dr. Jingxian Wu (Co-PI) and Dr. Narasimhan Rajaram (Co-PI) in collaboration with Dr. Keith Bailey as the consulting pathologist. Funding for the pulsed THz system was obtained through NSF/MRI award no. 1228958, titled "Acquisition of a Terahertz System for Medical and Biological Imaging and Nanomaterial Characterization Research at the University of Arkansas," led by Dr. Magda El-Shenawee (PI), in collaboration with Dr. Gregory Salamo (Co-PI), Dr. Steven Stephenson (Co-PI), Dr. Gilbert Pacey (Co-PI), and Dr. Robert Griffin (Co-PI). The THz imaging work for the ductal carcinoma in situ (DCIS) block samples was funded in part by the Chancellor Discovery Grant 2019 and the Women Giving Circle 2019, led by Dr. Magda El-Shenawee (Co-PI) in collaboration with Dr. Alexander H. Nelson (PI).

An external industrial company funded the free-space material characterization project under a non-disclosure agreement. The maintenance of the free-space system was funded in part through the GAP Chancellor's Innovation Fund under award no. 003184-00001A, led by Dr. Magda El-Shenawee (PI), and in part by the Department of Electrical Engineering at the University of Arkansas.

I would like to express my profound gratitude to my advisor and dissertation director of this work, Dr. Magda El-Shenawee, for her constant support and guidance throughout my Ph.D. The contribution of my advisor has been instrumental in my growth as a researcher and as an engineer.

I would like to thank the committee members of this dissertation, Dr. Narasimhan Rajaram, Dr. Jingxian Wu, and Dr. Zhong Chen, for their support and contribution to this work. I would also like to thank Dr. Jeffry Wolchok for using his lab space and equipments and Dr. Rajaram's students to help procure animal model tumors in this work.

I am thankful to Dr. Keith Bailey for his willing collaboration and pathological assessment for the biological samples used in this work and acknowledge the services provided by the Oklahoma Animal Disease Diagnostic Laboratory for the histopathology process on all the tumor samples handled in this work.

I appreciate and thank my former colleagues, Dr. Tyler Bowman, for his mentorship and THz system training and Dr. Tanny Chavez for her coordination in expanding this work to its current level. I would also like to thank the Terahertz Spectroscopy and Imaging Laboratory members, Jose Santos and Zhijun Gui, for their help in this work.

I am thankful to all the staff members of the electrical engineering department for their help whenever needed. I would like to thank the University of Arkansas for all the resources, opportunities, and platforms it provided me for my personal and professional growth.

Finally, yet importantly, I wish to express my love and gratitude to my family and friends for their constant support, encouragement, never-ending patience, without which this work would never be possible.

DEDICATION

To Mom, Rashmi Vohra, and Dad, Ramesh Vohra

for your endless love and faith, strength and encouragement, throughout this journey

TABLE OF CONTENTS

LIST OF PUBLISHED PAPERS

Chapter 2: N. Vohra, T. Bowman, K. Bailey, M. El-Shenawee, "Terahertz Imaging and Characterization Protocol for Freshly Excised Breast Cancer Tumors," *J. Vis. Exp.* issue. 158, e61007, 2020.

Chapter 3: N. Vohra, T. Bowman, P. M. Diaz, N. Rajaram, K. Bailey, M. El- Shenawee, "Pulsed terahertz reflection imaging of tumors in a spontaneous model of breast cancer," Biomedical Physics and Engineering Express, vol 4, no. 6, pp. 065025, 2018.

Chapter 4: N. Vohra, T. Chavez, J. R. Troncoso, N. Rajaram, J. Wu, P. N. Coan, T. A. Jackson, K. Bailey, and M. El-Shenawee, "Mammary tumors in Sprague Dawley rats induced by N-ethyl-N-nitrosourea for evaluating terahertz imaging of breast cancer," *J. Med. Imag.* vol. 8, no.2, pp. 023504, 2021.

Chapter 5: N. Vohra and M. El-Shenawee, "K- and W-Band Free-Space Characterizations of Highly Conductive Radar Absorbing Materials," in IEEE Transactions on Instrumentation and Measurement, vol. 70, pp. 1-10, 2021, Art no. 8001910.

CHAPTER 1

Introduction

1. Biological Materials: Imaging and Spectroscopy of Breast Cancer Tumors

1.1. Motivation

Cancer is a leading medical concern in the modern world, specifically breast cancer among women. As per the cancer statistics of 2020 by the American Cancer Society [1], the three most common cancers among women in the United States that account for a total of 50 % new diagnoses in 2020 are breast, lung, and colorectal, with breast cancer alone accounting for 30% of those cases. Although the cause of this disease is not specific, over the years, researchers have contributed various studies that might help narrow down the reason. For example, Brian MacMahon [2], in his research on the Epidemiology and causes of breast cancer, correlated the cause of occurrence of breast cancer to breastfeeding, lifetime lactation period, energy-rich diet, menopause, ovarian hormones, ionizing radiation exposure, alcohol consumption, and international variations. However, it is still an estimate; the certainty in this research has not yet been achieved.

Although the cause of breast cancer occurrence might not be known, its early detection plays an essential role in the successful management and treatment of the disease. With the advent of technology, the detection and screening of breast cancer have certainly improved with the years of research. The current diagnosis involves both imaging techniques and molecular biotechnology examination methods [3]. The most common techniques utilized in breast cancer detection and screening are mammography, ultrasonography, magnetic resonance imaging, Positron emission tomography, Optical imaging, CT, and puncture biopsy system [3, 4]. Each method has its advantages and disadvantages [3, 4]. However, the main goal is the early detection of breast cancer

to reduce the metastasis of cancer to the other organs through lymph nodes or the blood. In addition, these screening methods help detect cancer, its size, grade, and position in the breast.

Once the cancer is detected successfully, the next step involves surgical treatment. The two current surgical treatments followed to remove cancer from the breast are lumpectomy with radiation and mastectomy [5]. Mastectomy procedure consists of removing the entire breast and is used chiefly if cancer has spread in the whole breast. In contrast, lumpectomy, also known as breast-conserving therapy (BCT), involves just removing a cancerous lump along with some healthy tissue at its margin. The successful lumpectomy procedure helps to effectively remove breast cancer as a mastectomy procedure but with minor cosmetic damage [6]. The success of the lumpectomy surgery is defined by the status of the tissue at the excised tumor's margin. If the excised tumor has a negative margin—there is no cancer on the tumor margin—the surgery is a success. However, if the margins are positive—there is cancer on the excised tumor margin—the patient has to go through another surgery to remove the rest of the cancer and avoid local recurrence. Unfortunately, there is no defined answer to how much margin width is optimal to minimize local recurrence in patients undergoing BCT [7]. Variations in margin policy have been a topic of controversy among breast surgeons; however, no ink on tumor is the margin definition provided in the National Surgical Adjuvant Breast and Bowel Project (NSABP) B06 study in 1995 [8], and by the American Society of Radiation Oncology in 2014, that established the safety of BCT in invasive carcinoma [9].

1.2. Margin Assessment Techniques: Current State of the Art

The gold standard used for assessing excised tumor margins is the histopathology process, which involves fixating the excised tumor in formalin, followed by dehydration process, embedding it in the paraffin block, and finally sectioning the 3-4 μm thick slices of the tissue. The

sectioned tissue is fixed on a glass slide and stained with the standard hematoxylin and eosin (H&E) ink to analyze under the microscope. This method provides the margin tissue analysis at the microscopic cellular level. However, the limitation of this process is that it takes a few days to weeks to assess the tumor margins. Furthermore, if the margins are positive, the patient has to go through another surgery to avoid recurrence, which leaves the patient with financial, physical, and emotional trauma [10]. Therefore, many other techniques are followed commonly in most clinics to provide the margin assessment intraoperatively to prevent second surgery. A few of these intraoperative techniques are summarized in Table 1 with their mechanisms and limitations.

Among all the current clinically used margin assessment methods, researchers worldwide are investigating many new techniques. For example, the intelligent knife (iKnife) is a surgical knife developed based on the application of rapid evaporative ionization mass

Table 1. Summary of current commonly used techniques for intraoperative margin assessment of breast cancer

Category	Technique	Mechanism	Limitations
Rapid pathology	Frozen sectioning [11]	It involves freezing the excised tumor, followed by an incision of ~3-4 µm thick section and finally performing microscopic analysis of the sliced sections.	1. Not practical of full margin analysis because of tissue sectioning. 2. Increased intraoperative surgery time. 3. Necessity for a specialized pathologist in the operation room.
	Imprint cytology [11]	Involves scraping/cutting the excised tumor margin with a scalpel and gently pressing it on a glass slide; staining the tissue on the slide with hematoxylin and eosin (H&E) stain; and finally performing the microscopic analysis of the stained slide.	1. Necessity for a specialized cytologist in the operation room. 2. Does not distinguish between ductal carcinoma in situ and invasive carcinoma.

Table 1. (Cont.)

Category	Technique	Mechanism	Limitations
Wire Localization	Preoperative needle localization [12]	Using the mammography or ultrasound radiology techniques, the position of the tumor is obtained and a wire is inserted into the tumor. With the help of markers on the skin, distance to the tumor is determined for the best incision site. After excision, a mammogram is taken to confirm the excision of tumor.	1. This method requires same-day insertion of wire into the tumor, which requires coordination between the radiologist and the surgeon. 2. Wire placement may affect incision location, which may results in either undermining or excess removal of tissue.
Gross Assessment	Cavity Shaving [12]	Involves the removal of additional tissue margins after the excision of the original tumor.	1. Makes it difficult to measure the final tumor width and the final margin width. 2. The excessive tissue removal results in deforming the breast shape.
Imaging	Micro-computed tomography (micro-CT) [13]	The excised specimen is placed on the micro-CT scanner that passes X-rays through the excised tumor. The tumor is rotated 360° during the scanning process to obtain multi-planar, cross-sectional images.	1. It requires ~ 15 minutes of scanning time. 2. Need for a specialized radiologist in the surgical room to assess the obtained CT images. 3. This method is limited in differentiating between variable tissue density regions in the excised tumor.
	Magnetic Resonance Imaging [14]	After the removal of tumor, saline is placed in the breast cavity and MRI with gadolinium is performed. MRI evaluates the permeability of blood vessels in this process. Any residual tumor or uncertain margins are then re-excised.	1. Time consuming and expensive technique. 2. MRI cannot identify microcalcification, which is an important mammographic sign of DCIS.

Table 1. (Cont.)

Category	Technique	Mechanism	Limitations
Imaging	Ultrasonography [15]	This technique uses high frequency ultrasound that differentiates between healthy and cancerous tissues based on their acoustic properties.	1. Limited ability to scan the entire breast. 2. Time consuming review of large number of the images by the surgeon during the surgery.
	Positron emission tomography (PET) [4]	It is a nuclear medicine imaging method. Malignant cells tend to have increased glucose metabolism than normal breast cells and that is the basis of contrast in the PET scan images.	1. It is an invasive technique, as a radionuclide is introduced in the body for the imaging. 2. Expensive and Time consuming. 4. Yields poor resolution
Spectroscopy	Margin Probe [11]	It uses a single use hand held probe that operates at radiofrequency. The probe is held at the multiple locations on the excised tumor margin to obtain the spectroscopy analysis of the tissue.	1. Expensive technique as it adds an additional cost of the probe. 2. Invasive and Time consuming to examine the margins at several different locations. 3. Only detects cancer where the probe is placed.
	Bioimpedance spectroscopy [16]	It utilizes an impedance analyzer with a probe that records impedance of the tissue at the point where probe is placed at different frequencies. The difference between the impedance values of cancer and healthy tissues provide the margin assessment using this technique.	1. Invasive technique. 2. Requires the cutting of the margins to get a flat surface for correct impedance measurements. 3. Requires to wipe out any extra fluid or blood on the tissue that might interfere with the impedance measurements.

spectrometry. This device aims to provide the tissue's real-time molecular composition while it is being excised [17]. Among others, there are some optical imaging and spectroscopy techniques for margin assessment. These include fluorescence imaging [18], Raman spectroscopy [19], optical spectral imaging [20], and optical coherence tomography [21]. Although most of these techniques [17-21] achieved good accuracy in cancer detection, these have not been clinically used yet. It could be either due to the undergoing research or due to some innate limitations, such as limited speed, inability to quickly cover a large tissue area, an additional cost of the device, or the need for an expert operator. Thus, new technology is required that provides a reliable, cheap, faster, and easy assessment of the tumor margins intraoperatively.

1.3. Terahertz Radiations for Biological Tissues

The Terahertz (THz) gap is a region that refers to a frequency band ranging from 0.1 to 4 THz in the electromagnetic spectrum that lies between the microwaves and visible spectrum. The reason for its suitability to be used on biological tissues is its wavelength. Compared to the near-infrared (NIR) or optical radiations, the THz signal has longer wavelengths. The signal's wavelength is further related to the signal scattering, which occurs when it hits a particle of the same size as the incident wavelength. In biological tissues, the scattering could happen due to the variations in the refractive index of the tissue, extracellular constituents, and mammary cells, which are of comparable size as the wavelength of NIR or optical waves [22-23]. However, the THz wavelengths are several orders larger than the size of most biological structures; therefore, the scattering in biological tissues is weaker at THz wavelengths than visible and NIR wavelengths [22-23]. Thus, it provides the images obtained at THz frequencies with better contrast between different regions than the NIR or optical imaging techniques. Additionally, due to the longer wavelengths, the penetration depth of the THz signal is relatively more and, thus, it can provide in-depth information of the biological tissue [22, 23] that may aid the tissue assessment process.

Another advantage is that THz radiation carries very little energy as compared to the higher frequency radiations, e.g., X-rays. The energy is so less that it has no potential to ionize the materials on which it is incident, which makes it suitable for biological materials as it will not damage or change the properties of the tissues before pathology assessment [24]. Furthermore, due to higher frequency, THz provides higher resolution images with more details than microwave images.

1.4. Application of Terahertz Spectroscopy and Imaging in Biomedical Field

Terahertz is an emerging technique that has shown promising results in biomedical applications [25-30]. In the existing terahertz systems, data from the sample can be obtained in two different ways—transmission spectroscopy/imaging or reflection spectroscopy/imaging [30]. In transmission mode, the THz signal transmitted through the sample is recorded at the receiver antenna. Whereas in reflection mode, the THz signal reflected from the sample's surface is recorded at the receiver antenna. To perform the transmission measurements of the fresh tissue, the tissue thickness has to be optimal (usually in hundreds of micrometers); otherwise, the signal is attenuated due to the larger thickness of the tissue. However, reflection mode has its advantage over transmission mode, as it does not require tissue shaving to get the optimal thickness and can be used to scan the whole tissue surface to produce a THz image [30].

The application of THz imaging and spectroscopy is not only limited to cancerous diseases but has also been investigated for various non-cancerous human diseases or injuries [31-36]. For example, a study conducted by Omar B. Osman et al., using terahertz spectroscopy for differentiating burn wounds in an in vivo porcine model, reported the accurate classification of deep partial- and superficial partial-thickness burns from the collected reflected spectral data [36].

Another study by Lin Ke et al. [31] demonstrates the use of THz imaging and spectroscopy, in an ex vivo experiment on a rabbit model to detect the density and distribution of the corneal scar tissues. They introduced four different scars on the corneal tissue of the rabbit model through laser ablation and performed imaging using the THz system. They also imaged a healthy corneal tissue as a control sample and compared the results. It is reported that the healthy tissue showed smooth uniformed absorption, as compared to the scarred tissues that showed many absorption peaks spread from 1 THz to 3 THz, primarily due to the structure and composition change that happened in the scar center [31].

The THz spectroscopy has also been investigated for brain tissue excised from a mouse model of Alzheimer's disease (AD) [34]. In this study, Lingyan Shi et al. performed THz spectroscopy on 150 µm and 250 µm thick AD tissues. The reported absorption coefficient and refractive index plots from 0.5 THz to 2.5 THz demonstrate a clear differentiation between the AD disease tissue and the normal brain tissue of the same thickness. The study also reports the occurrence of three dominating absorption peaks allied to torsional–vibrational modes in AD tissue, at ~ 1.44, 1.8, and 2.114 THz, which were not observed in normal tissue.

Furthermore, the application of THz imaging has also been investigated in a study by G.G. Hernandez-Cardoso et al. for the early detection of diabetic foot syndrome [32]. This work reports the use of THz reflection imaging in differentiating between the diabetic syndrome feet and healthy feet based on the hydration level. As a result, it is concluded that the water content in the diabetic feet is less than the normal feet. Furthermore, the diabetic feet demonstrate a level of deterioration, which helped achieve the difference between healthy and diabetic syndrome feet using the THz imaging.

Among others, many studies report the use of THz imaging and spectroscopy techniques in the assessment of different types of cancerous tissues [37-52]. The discussion on a few of these studies is presented here. For example, Young Bin Ji et al., [39], in a study using a mice model, demonstrates THz reflectometry imaging (TRI) in the detection of grade II, III, and IV gliomas. Along with the TRI imaging technique implemented in this study, MRI, GFP fluorescence imaging, pathology imaging, optical coherence imaging, and ppIX fluorescence imaging techniques were also implemented for the same tissue. It was concluded in the paper that the TRI images provided the best contrast among all imaging methods, with cancer regions presenting high THz reflection signals compared with normal brain tissue regions in the tumor.

Prostate cancer is another cancer application where THz has proven its success. For example, Ping Zhang et al. [41] used the THz reflection imaging and spectroscopy technique in their study to diagnose prostate cancer. They used four paraffin-embedded block tumors, which consisted of prostate cancer tissue, normal prostate tissue, and muscle tissue. The obtained results showed that the muscle has a higher absorption coefficient than cancer, followed by normal tissue in the THz range. They also performed principal component analysis (PCA) and least squares support vector machine (LS-SVM) to classify the three tissue types in the samples and presented a 92.2% overall average recognition rate LS-SVM method.

In another study, the THz spectroscopy and imaging technique was used to detect skin melanoma [42] by growing murine B16 melanoma cells in ten BALB/c mice. The reflection imaging was performed on the excised fresh tissues, and results demonstrated a good differentiation between melanoma skin tissue and normal skin tissue. Furthermore, they concluded that the contrast in the images and difference in the refractive index and absorption coefficient values of these tissues was due to the amount of water content in each tissue. An experiment was

conducted in the same study to calculate the water content in the melanoma and normal skin tissues. The results demonstrated a higher water content level in melanoma tissue than normal tissue. These results are valid not only for skin cancer but also for other cancer and non-cancer tissue types [53-55]. Thus, for THz imaging and spectroscopy measurements, water plays a significant role in providing the contrast between different tissue types. In addition, THz is a safer, non-ionizing, and non-invasive imaging technique that shows the potential to be used as an intraoperative cancer assessment tool in the near future.

1.5. Terahertz Imaging and Spectroscopy of Breast Cancer Tumors

This work aims to apply the THz imaging and spectroscopy technique for the margin assessment of breast cancer tumors. The research on the margin assessment of this cancer using THz imaging and spectroscopy techniques started in 2004 [56], where the infiltrating ductal carcinoma (IDC) tumor tissue and ductal carcinoma in situ (DCIS) tumor tissue were imaged and differentiated against fat tissue. Until today, many researchers have contributed to this study. For example, Tyler Bowman et al. in [44] demonstrated the use of both reflection and transmission imaging methods to construct the THz images. In this study, FFPE tissue slides were used containing the paraffin-embedded tissues at 20-µm and 30-µm thickness. The tumors used in this work presented two different types of cancers: IDC and lobular carcinoma (LC). It was concluded in this study that both transmission and reflection imaging methods provide clear differentiation between cancer and healthy tissues, where cancer shows higher reflection and lower transmission compared to normal tissue types. However, it was reported that the reflection imaging provides higher resolution and more clear margins between cancerous, fibro glandular, and fatty tissues in the tumors. Many other studies on the FFPE breast cancer tissues have been investigated which reported similar findings [43, 45, 46, 47, 49]. FFPE tissues are dehydrated tissues; therefore, the

contrast in the THz images of these tissues is not due to the water but due to their electrical properties. In the same work [44], the authors showed refractive index plots of dehydrated cancer, fibroglandular, and fatty tissues, with cancer presenting the highest values (~1.8 at 1 THz), followed by fibroglandular (~1.7 at 1 THz), and fatty tissue showing the lowest of all (~1.5 at 1 THz).

Due to dehydration of the tissue and the absence of water, the THz signal tends to travel longer distances through the FFPE sample than fresh tissue samples. Based on this property of the THz waves, in another article, Tyler Bowman et al. showed the in-depth imaging of the FFPE block tissues [45]. The results in this article demonstrated the ability of THz to produce in-depth cross-sectional images without slicing the tissue, a capability of THz that can aid the pathology process. In the pathology process, the pathologist has to cut the tumor in several 3-4 μm thick slices in order to assess the margins under the microscope, which destroys the bulk tissue. Using the THz in-depth technique can help pathologists to determine the depth to slice the tissue for a potential presence of cancer at its margin to look under the microscope; this will further help preserve the rest of the tissue.

In THz imaging and spectroscopy measurements of freshly excised tissues, a study conducted by Philip C. Ashworth et al. [51] demonstrated the extraction of refractive index and absorption coefficient results. They measured freshly excised human breast cancer and normal tissues using the THz system. The results showed higher refractive index and absorption coefficient values of cancer followed by fibroglandular, and finally, fatty tissues obtained at the frequency ranging from 0.1 THz to 2 THz. However, the refractive index of cancer and collagen was almost equal and overlaps at the 95% confidence intervals of both plots. Additionally, it was reported that the cancerous and non-cancerous tissues were obtained from the excised tumor itself.

In another study, Tyler Bowman et al. [48] performed transmission spectroscopy and reflection imaging of freshly excised human breast cancer and healthy tissues. They used two types of tissues in this study— IDC breast cancer tissues with a very small or no healthy tissue at its margin, obtained via lumpectomy or mastectomy surgeries, and healthy breast tissues obtained via

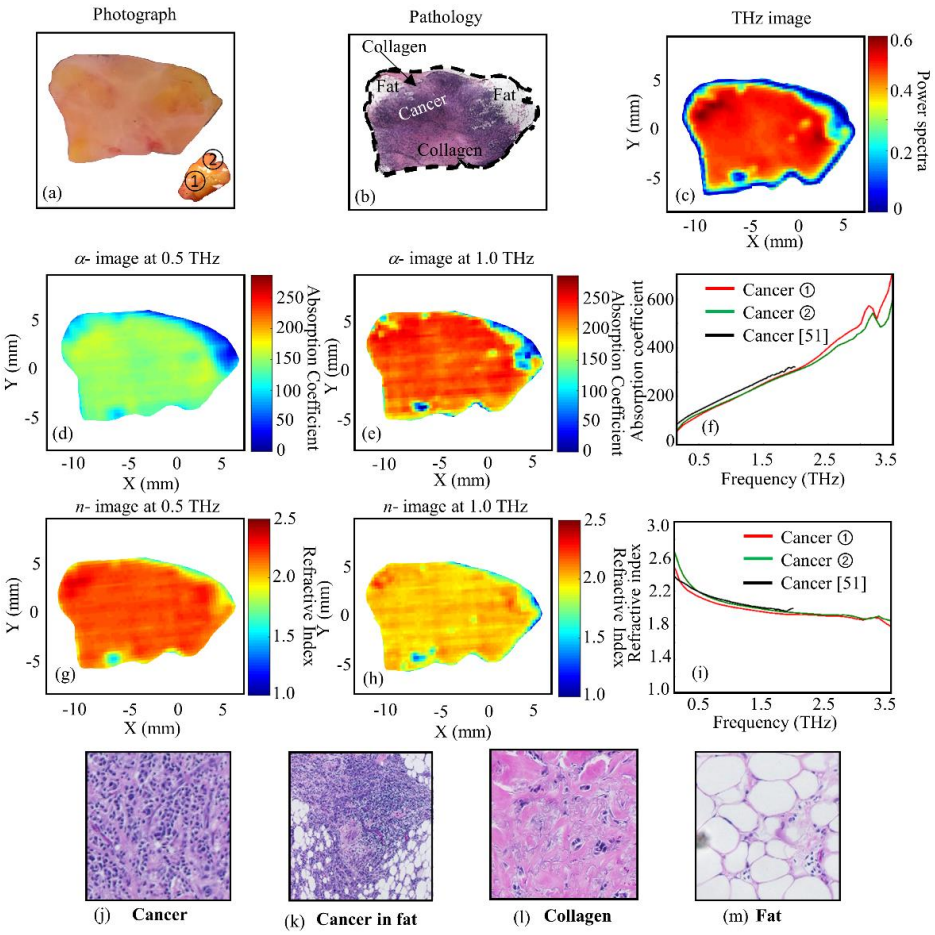

Fig. 1. THz images and spectroscopy of human fresh breast cancer tissue ND15348, (a) The photograph of the fresh tissue, (b) The low power pathology image, (c) The frequency domain THz image in spectral power over the range 0.5-1THz, (d) The reflection absorption coefficient (cm^{-1}) α-image at 0.5 THz, (e) The reflection absorption coefficient (cm^{-1}) α-image at 1.0 THz, (f) The transmission absorption coefficients (cm^{-1}) at points ① and ②, (g) The reflection refractive index *n*-image at 0.5 THz, (h) The reflection refractive index *n*-image at 1.0 THz, (i) The transmission refractive indices at points ① and ②. The high power pathology images for (j) cancer at point ③, (k) cancer at point ④, (l) Collagen, and (m) Fat. Each α- and *n*-image contains 1638 pixels. Figure republished from T. Bowman et al. [48] with permission from SPIE.

breast reduction surgeries. The THz tomographic reflection images and transmission spectroscopy plots were obtained for both cancerous and healthy breast tissues for frequencies ranging from 0.1 THz to 3.5 THz. The results of one of the cancer tissues handled in that work are presented here in Fig. 1. A photograph of the tumor ND15348 is presented in Fig. 1a; a low-power pathology image is presented in Fig. 1b, showing that around 90% of this tumor is cancer tissue with a small region of fatty tissue present at the upper right and upper left side of the cancer. Fig. 1c presents the THz power spectra image obtained at frequencies from 0.5 THz to 1.0 THz. Figs. 1d and 1e illustrate the absorption coefficient images constructed at 0.5 THz and 1 THz, respectively.

The results in these images show that the absorption coefficient of cancer is higher than fat, and it increases with an increase in frequency. This increasing trend can also be seen in the absorption coefficient vs. frequency plot in Fig. 1f. This plot demonstrates the absorption coefficient calculated using transmission spectroscopy of two tissue sections cut from the cancer region at the points marked ① and ② in Fig. 1a. The results obtained for two points were further compared against the digitized data obtained from the study by Philip C. Ashworth et al. [51]. The difference in results occurred primarily because in [51] the data was averaged over 33 samples whereas, in [48] it was just one point. Furthermore, a peak was reported in Fig. 1f, occurring around 3.5 THz. This peak was not observed in any healthy tissue spectroscopy results presented in [48] and could potentially serve as a biomarker for IDC breast cancer tissues in the THz range.

Similarly, the results in Figs. 1f to 1i present the refractive index image and plot for this sample. Here we see an opposite trend where the refractive index value decreases with an increase in frequency. Finally, Figs. 1j to 1n present the high-power microscopic pathology images of different tissue regions in this sample. This work handled the cancer tissues that were lacking enough healthy tissue at its margin. Even if cancer had healthy tissue at its margin, it was only fat

and lacked the presence of collagen. The challenge here is to differentiate between cancer and collagen present in the same tumor because the properties of these two tissue types are very close in the THz range [48, 51].

However, obtaining the freshly excised tumors from human subjects is difficult unless you collaborate with a hospital itself. There are biobanks, such as, National Disease Research Interchange (NDRI), Cooperative Human Tissue Network (CHTN), iSpecimen Marketplace, etc., that help academic researchers by providing the freshly excised human cancerous tissues within 24 hours of excision. However, these tissue sources are costly, and the frequency of receiving the tumor tissues is very low (one in a few months). Adding to that, the margins of the excised tumor are significant to the surgeons and pathologists for assessing it correctly. Pathologists do not give out the cancer tissue with surgical margins to the biobanks. The only tissue type that these biobanks have more access to is the cancer tissue with no surgical margin. Therefore, the lack of availability of tissues with margins hinders the research investigation on breast cancer margin assessment using THz techniques.

1.6. Laboratory Animal Models for Cancer Assessment

To overcome the limitation of unavailable freshly excised human breast cancer tumors and to investigate the margin assessment on actual cancer tissues with adjacent healthy margins, the animal models have provided an easy platform [57]. There are many animal species, mammals as well as non-mammals, such as chickens [58], zebrafish [59], rabbits, monkeys, dogs, pigs, [60], rats [61], mice [62], and non-human primates [63], that have been used as experimental models for the cancer research. Ideally, an animal model for cancer research should have a similar physiology as humans, and should be very simple and cheap. Among all these animal species, mouse and rat models have been more frequently used in research protocols performed in

American laboratories [64]. This is because of the advantages mice and rats offer when compared with other species. It is easy to accommodate them because of their small size; their physiology and genetic characteristics are well researched; they are relatively less expensive, and are quickly approved by the Institutional Animal Care and Use Committee (IACUC). Most importantly, they possess similar mammalian characteristics like physiology, anatomy, and genetic behavior as humans [61].

There are many existing methods by which mammary tumors can be induced in mouse and rat models [65]. Some of these processes involve—genetically modifying the model to produce mammary tumors [66], hormone induction [67], implantation of human cancer cell lines [68], and chemical induction [69]. In the previous study in our group on breast cancer margin assessment using THz imaging, we used a xenograft mouse model to grow mammary tumors after implanting the E0771 breast adenocarcinoma cells in the mouse mammary pad [46, 47]. The study reported THz imaging of 11 mice that produced tumors of size ~ 1cm in diameter. The THz imaging and statistical model results correctly assessed cancer in these tumors. However, the growth of these tumors lacked the presence of fibroglandular tissue. For successful investigation of margin assessment using THz imaging, the presence of fibroglandular tissue in the animal model tumors is of significant importance [68]. Therefore, in this work, we investigated the mouse mammary tumor virus- polyoma middle T antigen (MMTV-PyMT) transgenic mouse model and an N-ethyl-N-nitrosourea (ENU) injected Sprague Dawley rat model for the terahertz margin assessment of freshly excised breast cancer tumors.

1.7. Water: An Aid and a Barricade for Terahertz Imaging of Freshly Excised Tumors

As mentioned earlier, the amount of water content varies with each biological tissue in the human body [54]. Additionally, the THz signal is strongly absorbed by intermolecular bonds, e.g.,

hydrogen bonds present in water, which implies that it is susceptible to the amount of water content in the material. Thus, it serves as a differentiating factor, providing contrast between different tissue types when imaged at THz frequencies. However, water has also been a barrier when differentiating between cancer and collagen tissues in freshly excised human breast cancer tumors. As reported in [48], the differentiation between the electrical properties of freshly excised cancer tissue and healthy collagen tissues is very little due to the amount of water in them. Therefore, the differentiation between these regions in the THz images of breast cancer tumors is difficult to observe. Not only is this challenge reported in THz, but it also exists in other imaging techniques, such as optical imaging [70, 71]. The presence of water obstructs the pathway of the incident signal and thus disallows the penetration of the signal for tissue assessment.

1.8. Optical Clearing Agents

To increase the signal penetration and improve the contrast between different tissue types, many researchers in the optical imaging field have reported using glycerol solution as an optical clearing agent. The glycerol is a biocompatible hygroscopic viscous solution with an absorption coefficient much smaller than water in the THz frequency range [72]. In an experiment conducted by H.Q. Zhong et al. [73], the healthy and cancerous human breast tissues were treated with the 60% glycerol solution prior to the imaging to increase the penetration depth of the optical signal. The results showed OCT image enhancement upon treating the tissue with a 60% concentration of glycerol solution [73]. Another study by A.S. Kolesnikov et al. [74] monitored the THz signal penetration in an in-vitro muscle tissue upon dehydration using glycerol solution. The results showed the ability of the glycerol solution to form free water flow out of the tissue and hence increase the signal penetration [74]. Similarly, Seung Jae Oh et al. [75] reported the THz signal penetration enhancement through a freshly excised skin tissue that was treated with glycerol.

In this work, we used the 60% glycerol solution to treat breast cancer tumors to improve the contrast between cancer and collagen tissues by controlling the water level in both. Since efforts using the glycerol solution on freshly excised human breast cancer tissues are still in progress, results have not been published yet. However, preliminary results have appeared in an IEEE conference proceeding [76]. The details of this work are added to Appendix A in this dissertation.

2. Non-Biological Materials: Microwave and Millimeter-wave Characterization of Radar Absorbing Materials

2.1. Motivation

With the inclusion of radar systems in the automotive industry, the interest to manufacture radar-absorbing materials has increased in recent years. As known, the newly introduced car models are equipped with radar-based advanced driver assistance systems (ADAS) like—Collision Warning and Collision Avoidance (CW/CA), Adaptive Cruise Control (ACC), assisted lane change, Collision Mitigation Braking (CMS), and automated parking assist—which provide high volume production with low-cost potential. The radar sensors for these advanced systems are primarily deployed to function in the 24–26 GHz (short-range) and 76–77 GHz (long-range) allocated frequency bands [77]. However, the deployment of ADAS systems has led to an increase in the number of automotive radar sensors operating simultaneously in a compact space, which results in signal interference that can lead to a reduced signal-to-noise ratio or ghost targets [78]. Furthermore, the coupling between transmitting and receiving antennas and reflections from the adjacent metal structures of the vehicle can cause electromagnetic interference (EMI) in the automotive radar system. One potential solution to all these problems is utilizing high-frequency radar absorbing materials (RAMs) to cover the electronics in automobiles. RAM attenuates the

electromagnetic (EM) radiations by dissipating the incident EM energy into heat [79], [80]. However, shielding from the EM waves depends on the critical properties of the engineered composite materials [81]-[83]. Therefore, the electromagnetic characterization of the RAM material versus frequency is of significant importance.

2.2. Microwave and Millimeter-Wave Measurement Techniques

The well-known existing material characterization methods used to extract the electrical properties of the dielectric materials depend on high accuracy measurements [84-86]. These methods can considerably be divided into two main categories: resonant cavity techniques and transmission/reflection (T/R) techniques. In the former case, very accurate electromagnetic (EM) characterization is achievable, but it is limited to a single frequency measurement of materials with moderate resonance damping [87], [88]. In the latter case, commercial T/R devices, such as—coaxial cables [89, 90], waveguides [91-93], or free space propagation [104-119] —can be employed to perform the characterization of materials. These methods provide wideband material characterization in contrast to resonant cavity techniques. In both coaxial cable and waveguide techniques, the material is characterized in the dominant mode propagation band of the device. Moreover, the coaxial cable technique requires the shape of the material to be adaptive to the concentric corona of the cable, which leads to a complex manufacturing process [93]. Similarly, in the waveguide technique, the sample under test is fabricated concerning the waveguide size for the measurements. However, the major drawback of this technique is that the size of the waveguide dimensions decreases as the frequency increases. Therefore, fabricating the sample to the specific size at high frequencies becomes critical.

In contrast, the free space technique provides high accuracy contactless, non-destructive broadband measurements of highly conductive materials, independent of accurate sample

matching. It is a nondestructive measurement technique preferred over the other methods for many applications, precisely, for applications in the aerospace and automobile industries. It allows the broadband characterization of materials without the requirement of specific and accurate sample matching.

2.3. Development of Free-Space Non-Destructive Measurement Technique

The non-destructive measurement technique was first implemented in the 1940s [94, 95] for material characterization, and since then, with the advent of technology, it has been implemented in many different applications for the extraction of dielectric material properties. Until the 1980s, the non-destructive measurement procedures were based on waveguide methods [96-102]; therefore, researchers were not able to perform wideband measurements at higher frequencies due to the requirement of optimum waveguide size. However, in 1987, A. L. Cullen proposed a new non-destructive measurement technique that allowed measurements at broader frequency ranges [103]. This technique allowed measurements in the free space where the signal was transmitted through the air and directly passed through the sample placed between two antennas.

Later in 1989, D. K. Ghodgaonkar et al. demonstrated a free-space microwave system custom-built at Pennsylvania State University [104]. The system presented in this work consisted of two conical horn lens antennas that provided the bandwidth ranging from 14.5 GHz to 17.5 GHz. The transmitting and receiving antennas consisted of dielectric focused beam lenses, which provided the beam spot radius of ~ one wavelength when projected on the sample. The antennas were connected to the HP 8510B network analyzer that recorded the frequency domain S-parameters for the metal-backed reflection measurements of the samples. The well-known transmission line model was implemented to extract the dielectric constant and loss tangent of

three samples— fused quartz, Teflon, and PVC—which were measured at frequencies ranging from 14.5 GHz to 17.5 GHz.

Further, in 1990, V. V. Varadan et al. [105] reported the extension of their free-space system which was upgraded to provide measurements for higher frequencies from 5 to 100 GHz. This upgraded system provided transmission and reflection measurements at normal and oblique incident antenna positions. In the same year, they published another article that demonstrated the use of this upgraded system for the measurements of different thickness samples until 40 GHz frequency [106]. The results were reported with an error of less than 5% at mid-band. The paper also reported the measurement of a very thin and flexible sample. They used the sandwich technique for the measurements, where the sample was placed between two equal thickness quartz plates to avoid sample sagging and bending during the measurements. To extract the S-parameters of the actual sample from the measured S-parameters of the quartz-sample-quartz assembly, they implemented a decomposition technique [106].

Since then, many other studies are reported in the literature [104-119] that implemented free-space measurement techniques at several different microwave and millimeter-wave frequency bands to extract the dielectric properties of the unknown materials. However, to the best of the author's knowledge, no study has yet been reported that used the free-space measurement technique to extract the relative permittivity of very highly conductive materials in the W-band. Therefore, in this work, we propose using a free-space method to characterize the highly conductive carbon-based non-magnetic radar absorbing materials at K- and W-bands to be used in short-range radar (SRR) and long-range radar (LRR) systems integrated into automobiles.

2.4. Free-Space Measurement System at the University of Arkansas

The microwave and millimeter-wave free-space measurement system used in this work is shown in Fig. 2. It is composed of transmitting and receiving conical horn antennas with bandwidth ranging from 10 MHz to 110 GHz. The antennas and the sample holder are mounted on a ± 2 µm precision positioning system fixed on a large aluminum table, as shown in Fig. 2a. This positioning system provides four degrees of freedom for the antenna movement in X, Z, theta, and phi directions [118]. At the same time, the sample holder stage is only restricted to the motion in Y-direction. The system is connected to an Agilent PNA E8361C network analyzer, an N5260A millimeter-wave controller, and two millimeter-wave frequency extenders to obtain the measurements for frequencies ranging from 10 MHz to 110 GHz.

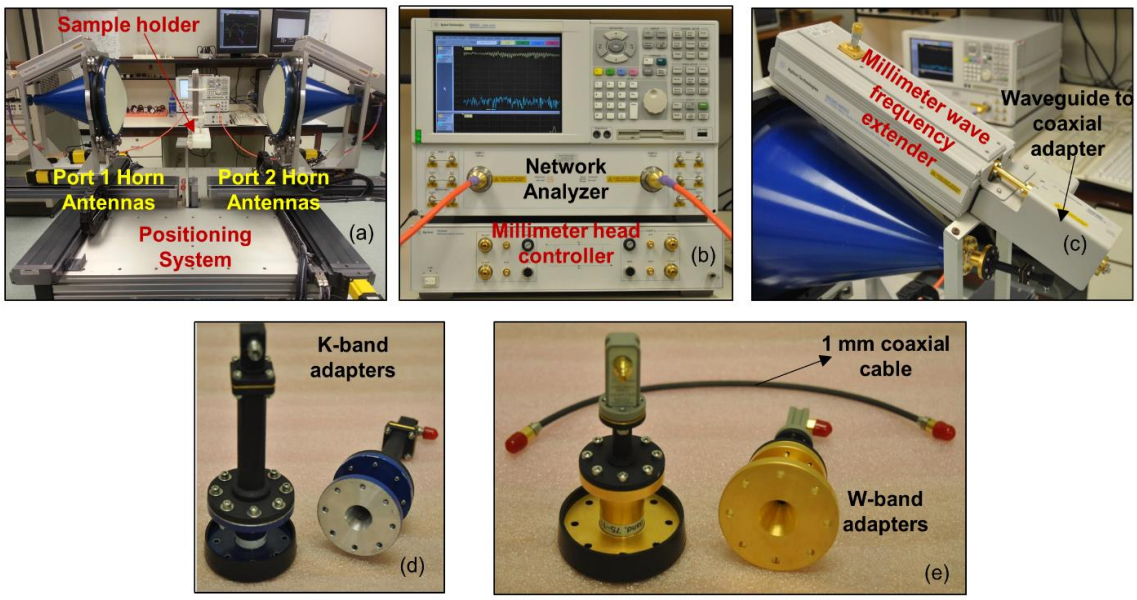

Fig. 2. Microwave and millimeter wave free-space measurement system. (a) Experimental measurement system composed of two horn lens antennas, sample holder, and a network analyzer mounted on a positioning system, (b) An Agilent PNA E8361C network analyzer and millimeter wave controller, (c) Millimeter wave frequency extenders to extend the frequency range of the network analyzer from 67 GHZ to 110 GHz, (d) *K*-band co-axial to waveguide adapters for each horn antenna, (e) *W*-band co-axial to waveguide adapters for each horn antenna along with a 1 mm coaxial cable that connects the horn antenna to the frequency extender.

As known, the radiation from the horn antennas grow outwardly, and by the time it reaches the target, the energy is no longer concentrated in one spot. To avoid such a phenomenon, two equal plano-convex dielectric lenses are mounted back to back on the conical horn antenna to focus the antenna beam in the center of the sample. The distance between both transmitting and receiving horn antennas is ~61 cm and the focal distance to diameter ratio of the lens is one with the diameter of the lens equal to ~30.5 cm. To hold the planar sample for measurements, a specially fabricated sample holder is placed at the common focal plane of both antennas.

The PNA E8361C network analyzer used in this work, as shown in Fig. 2b, can generate the incident signal at frequencies ranging from 10 MHz to 67 GHz. It is equipped with a set of 1.85 mm female coaxial gold connectors that connect the network analyzer to the rest of the system using the 60-inch co-axial cables (orange cables), as shown in Fig. 2b. To feed the antennas with the required frequency signal, a coaxial-to-waveguide adapter is used that converts the coaxial line signal received from the network analyzer to the required microwave/mm-wave frequency signal. This adapter includes a coaxial line to rectangular waveguide adapter, followed by a rectangular waveguide to circular waveguide adapter. These adapters are designed for the specific frequency ranges at which only TE_{10} dominant mode is excited within the rectangular waveguide section. The successful verification of the dominant mode excitation for various coaxial-to-waveguide adapters was performed in our lab by the graduate student Clifford E. Kintner; the verification test methods and results are presented in [119]. To cover the whole bandwidth range of the conical horn antennas shown in Fig. 2a, a total of eight pairs of the coaxial-to-waveguide adapters are used that cover the frequency range from C-band (4-8 GHz) to the W-band (75-110 GHz). In this work, the measurements are performed in K-band and W-band only; thus, the K-band adapters (1.85 mm

female connector) and W-band adapters (1 mm female connector) are used to feed the antenna, as shown in Fig. 2d and 2e.

For frequency bands higher than 67 GHz, the horn antennas are connected to the millimeter-wave frequency extenders, as shown in Fig. 2c, which provide frequencies ranging from 67 GHz to 110 GHz. The frequency extender has a WR-10 waveguide to 1 mm coaxial adapter that connects it to the horn antenna via coaxial-to-waveguide adapter using the 1 mm cable, as shown in Fig. 2e. The frequency extenders are further connected to the network analyzer via the N5260A millimeter-wave head controller shown in Fig. 2b. The millimeter-wave head controller provides the low-frequency signal to the frequency extenders which, using the inbuilt multiplexers, convert this signal to the high frequency, specifically from 67 GHz to 110 GHz. The horn antenna then transmits the mm-wave frequency signal in the free-space towards the receiver antenna. The received signal at the receiver antenna is fed back to the frequency extender the same way through the adapter and 1 mm coaxial cable. There it is down-converted to a low-frequency signal to feed it back to the network analyzer through the same connections for further analysis.

In this work, we measured a total of 51 samples, at both K-band and W-band, in both transmission and reflection mode methods. The transmission and reflection mode S-parameters are measured using the PNA network analyzer, and the relative permittivity is extracted utilizing the algorithm developed in this work. The extracted relative permittivity of these samples is further verified by back calculating the transmission and reflection S-parameters. The details of this work are provided in Chapter 5 in this dissertation.

3. Overview of Dissertation Chapters

This dissertation follows the progression of experimental and analysis of the electromagnetic characterization of biological materials in the terahertz frequency band and non-

biological materials in the microwave and millimeter-wave frequency bands. Chapter 1 has provided an overall introduction to the literature background, methods, and materials used throughout this work. Each subsequent chapter of this work corresponds to a single published paper in a peer-reviewed journal. The chapters and citations with their corresponding reference number for this chapter are as follows:

Chapter 2 [120]: N. Vohra, T. Bowman, K. Bailey, M. El-Shenawee, "Terahertz Imaging and Characterization Protocol for Freshly Excised Breast Cancer Tumors," *J. Vis. Exp.* issue. 158, e61007, 2020.

Chapter 3 [121]: N. Vohra, T. Bowman, P. M. Diaz, N. Rajaram, K. Bailey, M. El- Shenawee, "Pulsed terahertz reflection imaging of tumors in a spontaneous model of breast cancer," Biomedical Physics and Engineering Express, vol 4, no. 6, pp. 065025, 2018.

Chapter 4 [122]: N. Vohra, T. Chavez, J. R. Troncoso, N. Rajaram, J. Wu, P. N. Coan, T. A. Jackson, K. Bailey, M. El-Shenawee, "Mammary tumors in Sprague Dawley rats induced by N-ethyl-N-nitrosourea for evaluating terahertz imaging of breast cancer," *J. Med. Imag.* vol. 8, no.2, pp. 023504, 2021.

Chapter 5 [123]: N. Vohra and M. El-Shenawee, "K- and W-Band Free-Space Characterizations of Highly Conductive Radar Absorbing Materials," in IEEE Transactions on Instrumentation and Measurement, vol. 70, pp. 1-10, 2021, Art no. 8001910.

Lastly, Chapter 6 will provide overall concluding remarks and key challenges observed throughout the dissertation.

References

[1] R. L. Siegel, K. D. Miller, and A. Jemal, "Cancer statistics, 2020," *CA: a cancer journal for clinicians*, vol. 70, no. 1, pp. 7-30, 2020.

[2] B. MacMahon, "Epidemiology and the causes of breast cancer," *Int J Cancer*, vol. 118, no. 10, pp. 2373-2378, 2006.

[3] Z. He, Z. Chen, M. Tan, S. Elingarami, Y. Liu, T. Li, Y. Deng, N. He, S. Li, J. Fu, and W. Li, "A review on methods for diagnosis of breast cancer cells and tissues," *Cell Proliferation*, vol. 53, no. 7, pp. e12822, 2020.

[4] S. V. Sree, E. Y. Ng, R. U. Acharya, and O. Faust, "Breast imaging: A survey," *World journal of clinical oncology*, vol. 2, no. 4, pp. 171–178, 2011.

[5] A. G. Waks and E. P. Winer, "Breast cancer treatment: A review," *JAMA, vol.* 321, no. 3, pp. 288–300, 2019.

[6] M. A. Rahman, F. Arjuman, S. Alam, M. I. Khalil, Q. Habibullah, K. A. B. M. Abdullah Al Hasan, F. Afroz, and N. N. Aymon, "Lumpectomy versus mastectomy in breast cancer: comparison of postoperative consequences and treatment progress," *Cancer Research Journal*, vol. 9, no. 1, pp. 79-84, 2021.

[7] M. Pilewskie, and M. Morrow, "Margins in Breast Cancer: How much is enough?," *Cancer*, vol. 124, no. 7, pp. 1335-1341, 2018.

[8] B. Fisher, S. Anderson, C. K. Redmond, N. Wolmark, D. L. Wickerham, and W. M. Cronin, " Reanalysis and results after 12 years of follow-up in a randomized clinical trial comparing total mastectomy with lumpectomy with or without irradiation in the treatment of breast cancer," *N Engl J Med*. Vol. 333, no. 22, pp.1456-1461, 1995.

[9] M. S. Moran, S. J. Schnitt, A. E. Giuliano, J. R. Harris, S. A. Khan, J. Horton, S. Klimberg, M. Chavez-MacGregor, G. Freedman, N. Houssami, P. L. Johnson, and M. Morrow, "Society of surgical oncology-american society for radiation oncology consensus guideline on margins for breast-conserving surgery with whole-breast irradiation in stages I and II invasive breast cancer," *Int. J. Radiat. Oncol.*, vol. 88, no. 3, pp. 553–564, 2014.

[10] B. W. Maloney, D. M. McClatchy, B. W. Pogue, K. D. Paulsen, W. A. Wells, and R. J. Barth, "Review of methods for intraoperative margin detection for breast conserving surgery," *J. Biomed. Opt.*, vol. 23, no. 10, pp. 100901, 2018.

[11] J. J. Keating, C. Fisher, R. Batiste, and S. Singhal, "Advances in intraoperative margin assessment for breast cancer," *Curr. Surg. Rep.*, vol. 4, no. 15, pp. 1-8, 2016.

[12] C. Reyna and S. M. DeSnyder, "Intraoperative margin assessment in breast cancer management," *Surg. Oncol. Clinics of North America*, vol. 27, no. 1, pp. 155-165, 2018.

[13] J. Schwarz and H. Schmidt, "Technology for intraoperative margin assessment in breast cancer," *Ann. Surg. Oncol.*, vol. 27, pp. 2278-2287, 2020.

[14] R. M. Mann, N. Cho, and L. Moy, "Breast MRI: State of the art," *Radiology*, vol. 292, no. 3, pp. 520-536, 2019.

[15] R. J. Hooley, L. M. Scoutt, and L. E. Philpotts, "Breast ultrasonography: State of the art," *Radiology*, vol. 268, no. 3, pp. 642-659, 2013.

[16] Z. Du, H. Wan, Y. Chen, Y. Pu, and X. Wang, "Bioimpedance spectroscopy can precisely discriminate human breast carcinoma from benign tumors," *Medicine*, vol. 96, no. 4, pp. e5970, 2017.

[17] B. Vaqas, S. J. Cameron, J. L. Alexander, K. S. O'Neill, J. M. Kinross, and Z. Takats, "Chapter 7 - The iKnife: Development and clinical applications of rapid evaporative ionization mass spectrometry," *The Handbook of Metabolic Phenotyping- Elsevier*, pp. 219-236, 2019.

[18] L. J. Lauwerends, P. B. A. A. v. Driel, R. J. B. de Jong, J. A. U. Hardillo, S. Koljenovic, G. Puppels, L. Mezzanotte, C. W. G. M. Löwik, E. L. Rosenthal, A. L. Vahrmeijer, and S. Keereweer, "Real-time fluorescence imaging in intraoperative decision making for cancer surgery," *The Lancet Oncology*, vol. 22, no. 5, pp. e186-e195, 2021.

[19] W. C. Zúñiga, V. Jones, S. M. Anderson, A. Echevarria, N. L. Miller, C. Stashko, D. Schmolze, P. D. Cha, R. Kothari, Y. fong, and M. C. Storrie-Lombardi, "Raman Spectroscopy for Rapid Evaluation of Surgical Margins during Breast Cancer Lumpectomy," *Sci. Rep.*, vol. 9, no. 14639, 2019.

[20] U. M. Pal, M. Saxena, G. K. A.Vishnu, D. Parsana, B. S. R. Sarvani, M. Varma, M. Jayachandra, V. Kurpad, D. Baruah, G. Gogoi, J. S. Vaidya, and H. J. Pandya, "Optical spectroscopy-based imaging techniques for the diagnosis of breast cancer: A novel approach," *Applied Spectroscopy Reviews*, vol. 55, no. 8, pp. 778-804, 2020.

[21] R. Ha, L. C. Friedlander, H. Hibshoosh, C. Hendon, S. Feldman, S. Ahn, H. Schmidt, M. K. Akens, M. Fitzmaurice, B. C. Wilson, and V.L. Mango, "Optical Coherence Tomography: A Novel Imaging Method for Post-lumpectomy Breast Margin Assessment—A Multi-reader Study," *Academic Radiology*, vol. 25, no. 3, pp. 279-287, 2018.

[22] P. Y. Han, G. C. Cho, and X.-C. Zhang, "Time-domain transillumination of biological tissues with terahertz pulses," *Opt. Lett.*, vol. 25, no. 4, pp. 242–244, Feb. 15, 2000.

[23] G. J. Wilmink and J. E. Grundt, "Current state of research on biological effects of terahertz radiation," *J. Infrared Milli-Terahertz Waves*, vol. 32, pp. 1074–1122, 2011.

[24] P. H. Siegel, "Terahertz technology in biology and medicine," *IEEE Trans. Microw. Theory Tech.*, vol. 52, no. 10, pp. 2438–2447, Oct. 2004.

[25] O.A. Smolyanskaya, N.V. Chernomyrdin, A.A. Konovko, K.I. Zaytsev, I.A. Ozheredov, O.P. Cherkasova, M.M. Nazarov, J.-P. Guillet, S.A. Kozlov, Yu. V. Kistenev, J.-L. Coutaz, P. Mounaix, V.L. Vaks, J.-H. Son, H. Cheon, V.P. Wallace, Yu. Feldman, I. Popov, A.N. Yaroslavsky, A.P. Shkurinov, and V.V. Tuchin, " Terahertz biophotonics as a tool for studies of dielectric and spectral properties of biological tissues and liquids," *Progress in Quantum Electronics*, vol. 62, pp. 1-77, 2018.

[26] X. Yang, X. Zhao, K. Yang, Y. Liu, Y. Liu, W. Fu, and Y. Luo, "Biomedical Applications of Terahertz Spectroscopy and Imaging," *Trends in Biotechnology*, vol. 34, no. 10, pp. 810-824, 2016.

[27] G. R. Musina, P. V. Nikitin, N. V. Chernomyrdin, I. N. Dolganova, A. A. Gavdush, G. A. Komandin, D. S. Ponomarev, A. A. Potapov, I. V. Reshetov, V. V. Tuchin, and K. I. Zaytsev, "Prospects of terahertz technology in diagnosis of human brain tumors – A review," *Journal of Biomedical Photonics & Engineering*, vol. 6, no. 2, pp. 020201, 2020.

[28] Y. Peng, C. Shi, X. Wu, Y. Zhu, and S. Zhuang, “Terahertz Imaging and Spectroscopy in Cancer Diagnostics: A Technical Review,” *BME Frontiers*, vol. 2020, article ID 2547609, 11 pages, 2020.

[29] Q. Sun, Y. He, K. Liu, S. Fan, E. Parrott, and E. Pickwell-MacPherson, “Recent advances in terahertz technology for biomedical applications,” *Quant Imaging Med Surg*., vol. 7, no. 3, pp. 345-355, 2017.

[30] M. El-Shenawee, N. Vohra, T. Bowman, and K. Bailey, “Cancer detection in excised breast tumors using terahertz imaging and spectroscopy,” *Biomedical Spectroscopy and Imaging*, vol. 8, no. 1-2, pp. 1-9, 2019.

[31] L. Ke, Q. Y. S. Wu, N. Zhang, H. W. Liu, E. P. W. Teo, J. S. Mehta, and Y. C. Liu, “Ex vivo sensing and imaging of corneal scar tissues using terahertz time domain spectroscopy,” *Spectrochimica Acta Part A: Molecular and Biomolecular Spectroscopy*, vol. 255, 119667, 2021.

[32] G. Hernandez-Cardoso, S. Rojas-Landeros, M. Alfaro-Gomez, A. I. Hernandez-Serrano, I. Salas-Gutierrez, E. Lemus-Bedolla, A. R. Castillo-Guzman, H. L. Lopez-Lemus, and E. Castro-Camus, “Terahertz imaging for early screening of diabetic foot syndrome: A proof of concept,” *Sci Rep*, vol. 7, 42124, 2017.

[33] A. I. Nikitkina, P. Bikmulina, E. R. Gafarova, N. V. Kosheleva, Y. M. Efremov, E. A. Bezrukov, D. V. Butnaru, I. N. Dolganova, N. V. Chernomyrdin, O. P. Cherkasova, A. A. Gavdush, and P. S. Timashev, "Terahertz radiation and the skin: a review," *J. Biomed. Opt*., vol. 26, no. 4, 043005, 2021.

[34] L. Shi, P. Shumyatsky, A. Rodríguez-Contreras, and R. Alfano, “Terahertz spectroscopy of brain tissue from a mouse model of Alzheimer's disease,” *J. Biomed. Opt*., vol. 21, no. 1, 15014, 2016.

[35] H. Zhao, Y. Wang, L. Chen, J. Shi, K. Ma, L. Tang, D. Xu, J. Yao, H. Feng, and T. Chen, "High-sensitivity terahertz imaging of traumatic brain injury in a rat model," *J. Biomed. Opt*., vol. 23, no. 3, 036015, 2018.

[36] O. B. Osman, T. J. Tan, S. Henry, A. Warsen, N. Farr, A. M. McClintic, Y. N. Wang, S. Arbabi, and M. Hassan Arbab, "Differentiation of burn wounds in an in vivo porcine model using terahertz spectroscopy," *Biomed. Opt. Express*, vol. 11, pp. 6528-6535, 2020.

[37] S. Yamaguchi, Y. Fukushi, O. Kubota, T. Itsuji, T. Ouchi, and S. Yamamoto, *“*Brain tumor imaging of rat fresh tissue using terahertz spectroscopy,” *Sci. Rep.*, vol. 6, article no. 30124, 2016.

[38] O. Cherkasova, Y. Peng, M. Konnikova, Y. Kistenev, C. Shi, D. Vrazhnov, O. Shevelev, E. Zavjalov, S. Kuznetsov, and A. Shkurinov, “Diagnosis of Glioma Molecular Markers by Terahertz Technologies,” *Photonics*, vol. 8, no. 22, pp. 1-30, 2021.

[39] Y. B. Ji, S. J. Oh, S. G. Kang, J. Heo, S. H. Kim, Y. Choi, S. Song, H. Y. Son, S. H. Kim, J. H. Lee, S. J. Haam, Y. M. Huh, J. H. Chang, C. Joo, and J. S. Suh, "Terahertz reflectometry imaging for low and high grade gliomas," *Sci. Rep.*, vol. 6, article no. 36040, 2016.

[40] Y. B. Ji, S. H. Kim, K. Jeong, Y. Choi, J. H. Son, D. W. Park, S. K. Noh, T. In. Jeon, Y. M. Huh, S. Haam, S. K. Lee, S. J. Oh, and Ji. S. Suh, "Terahertz spectroscopic imaging and properties of gastrointestinal tract in a rat model," *Biomed. Opt. Express*, vol. 5, pp. 4162-4170, 2014.

[41] P. Zhang, S. Zhong, J. Zhang, J. Ding, Z. Liu, Y. Huang, N. Zhou, W. Nsengiyumva, and T. Zhang, "Application of Terahertz Spectroscopy and Imaging in the Diagnosis of Prostate Cancer," *Curr. Opt. Photon*, vol. 4, pp. 31-43, 2020.

[42] D. Li, Z. Yang, A. Fu, T. Chen, L. Chen, M. Tang, H. Zhang, N. Mu, S. Wang, G. Liang, and H. Wang, "Detecting melanoma with a terahertz spectroscopy imaging technique," *Spectrochimica Acta Part A: Molecular and Biomolecular Spectroscopy*, vol. 234, article no. 118229, 2020.

[43] T.C. Bowman, M. El-Shenawee, and L.K. Campbell. "Terahertz Imaging of Excised Breast Tumor Tissue on Paraffin Sections." *IEEE Trans. on Ant. and Propag*., vol. 63, no. 5, pp. 2088-2097, 2015.

[44] T. Bowman, M. El-Shenawee, and L.K. Cambell, "Terahertz transmission vs reflection imaging and model-based characterization for excised breast carcinomas" *Biomed. Opt. Express*, vol. 7, no. 9, pp. 3756-3783, 2016.

[45] T. Bowman, Y. Wu, J. Gauch, L. K. Campbell, and M. El-Shenawee, "Terahertz Imaging of Three-Dimensional Dehydrated Breast Cancer Tumors," *J. Infrared Milli. Terahz. Waves*, vol. 38, no. 6, pp. 766-786, 2017.

[46] T. Bowman, T. Chavez, K. Khan, J. Wu, A. Chakraborty, N. Rajaram, K. Bailey, and M. El-Shenawee, "Pulsed terahertz imaging of breast cancer in freshly excised murine tumors," *J. Biomed. Opt*., vol. 23, no. 2, pp. 026004, 2018.

[47] T. Chavez, T. Bowman, J. Wu, K. Bailey, and M. El-Shenawee, "Assessment of Terahertz Imaging for Excised Breast Cancer Tumors with Image Morphing," *J. Infrared Milli. Terahz Waves*, vol. 39, no. 12, 1283–1302, 2018.

[48] T. Bowman, N. Vohra, K. Bailey, and M. El-Shenawee, "Terahertz tomographic imaging of freshly excised human breast tissues," *J. Med. Imag.*, vol. 6, no. 2, article no. 023501, 2019.

[49] T. Chavez, N. Vohra, J. Wu, K. Bailey, and M. El-Shenawee, "Breast Cancer Detection With Low-Dimensional Ordered Orthogonal Projection in Terahertz Imaging," in *IEEE Transactions on Terahertz Science and Technology*, vol. 10, no. 2, pp. 176-189, 2020.

[50] A. J. Fitzgerald, V. P. Wallace, M. J. Linan, L. Bobrow, R. J. Pye, A. D. Purushotham, and D. D. Arnone, “Terahertz Pulsed Imaging of human breast tumors,” *Radiology*, vol. 239, no. 2, pp. 533–540, 2006.

[51] P. C. Ashworth, E. P. MacPherson, E. Provenzano, S. E. Pinder, A. D. Purushotham, M. Pepper, and V. P. Wallace, “Terahertz pulsed spectroscopy of freshly excised human breast cancer,” *Opt. Express*, vol. 17, no. 15, pp. 12444–12454, 2009.

[52] A. J. Fitzgerald, S. Pinder, A. D. Purushotham, P. O’Kelly, P. C. Ashworth, and V. P. Wallace, “Classification of terahertz-pulsed imaging data from excised breast tissue,” *J. Biomed. Opt*., vol. 17, no. 1, article no. 016005, 2012.

[53] J. H. Chen, H. E. Avram, L. E. Crooks, M. Arakawa, L. Kaufman, and A. C. Brito, “In vivo relaxation times and hydrogen density at 0.063-4.85 T in rats with implanted mammary adenocarcinomas,” *Radiology*, vol. 184, no. 2, pp. 427-434, 1992.

[54] K. F. Ross and R. E. Gordon, “Water in malignant tissue, measured by cell refractometry and nuclear magnetic resonance,” *J. Microsc.*, vol. 128, pp. 7-21, 1982.

[55] K. Lee, K. Jeoung, S. H. Kim, Y. B. Ji, H. Son, Y. Choi, Y. M. Huh, J. S. Suh, and S. J. Oh, “Measuring water contents in animal organ tissues using terahertz spectroscopic imaging. *Biomed Opt Express*,” vol. 9, no. 4, pp. 1582-1589, 2018.

[56] A. J. Fitzgerald, V. P. Wallace, R. Pye, M. Jimenez-Linan, L. Bobrow, A. D. Purushotham, and D. D. Arnone, "Terahertz imaging of breast cancer, a feasibility study," *Infrared and Millimeter Waves, Conference Digest of the 2004 Joint 29th International Conference on 2004 and 12th International Conference on Terahertz Electronics, 2004.*, pp. 823-824, 2004.

[57] Z. Li, W. Zheng, H. Wang, Y. Cheng, Y. Fang, F. Wu, G. Sun, G. Sun, C. Lv, and B. Hui, “Application of Animal Models in Cancer Research: Recent Progress and Future Prospects,” *Cancer Manag. Res*., vol. 13, pp. 2455-2475, 2021.

[58] A. K. Gheorghescu, B. Tywoniuk, J. Duess, N. V. Buchete, and J. Thompson, “Exposure of chick embryos to cadmium changes the extra-embryonic vascular branching pattern and alters expression of VEGF-A and VEGF-R2,” *Toxicol Appl. Pharmacol*., vol. 289, no. 1, pp. 79-88, 2015.

[59] J. Ren, S. Liu, C. Cui, and P. T. Dijke, “Invasive Behavior of Human Breast Cancer Cells in Embryonic Zebrafish,” *J Vis Exp*., vol. 122, article no. 55459, 2017.

[60] A. Tsubura, Y. C. Lai, H. Miki, T. Sasaki, N. Uehara, T. Yuri, and K. Yoshizawa, “Review: Animal models of N-Methyl-N-nitrosourea-induced mammary cancer and retinal degeneration with special emphasis on therapeutic trials,” *In Vivo*, vol. 25, no. 1, pp. 11-22, 2011.

[61] A. Alvarado, A. I. Faustino-Rocha, B. Colaço, and P. A. Oliveira, “Experimental mammary carcinogenesis - Rat models,” *Life Sci*., vol. 173, pp. 116-134, 2017.

[62] H. C. Manning, J. R. Buck, and R. S. Cook, “Mouse Models of Breast Cancer: Platforms for Discovering Precision Imaging Diagnostics and Future Cancer Medicine,” *J. Nucl. Med*., vol. 57, pp. 60S-8S, 2016.

[63] F. N. Dewi and J. M. Cline, “Nonhuman primate model in mammary gland biology and neoplasia research,” *Lab Anim. Res., vol.* 37, no. 3, 2021.

[64] L. Carbone, “Estimating mouse and rat use in American laboratories by extrapolation from Animal Welfare Act-regulated species,” *Sci. Rep.*, vol. 11, no. 493, 2021.

[65] M. A. Bazm, L. Naseri, and M. Khazaei, “Methods of inducing breast cancer in animal models: a systematic review*,” WCRJ*, vol. 5, no. 4, pp. e1182, 2018.

[66] A. Doyle, M. P. McGarry, N. A. Lee, and J. J. Lee, “The construction of transgenic and gene knockout/knockin mouse models of human disease,” *Transgenic Res*., vol. 21, no. 3, pp. 327-349, 2012.

[67] J. D. Shull, T. J. Spady, M. C. Snyder, S. L. Johansson, and K. L. Pennington, “Ovary-intact, but not ovariectomized female ACI rats treated with 17beta-estradiol rapidly develop mammary carcinoma,” *Carcinogenesis*, vol. 18, no. 8, pp. 1595-601, 1997.

[68] J. B. Kim, M. J. O'Hare, and R. Stein, “Models of breast cancer: is merging human and animal models the future?” *Breast Cancer Res*., vol. 6, no. 1, pp. 22-30, 2004.

[69] J. S. Howell, “Studies on chemically induced breast tumors in the rat,” *Acta Unio Int Contra Cancrum*., vol. 19, pp. 762-4, 1963.

[70] S. A. Boppart, F.T. Nguyen, A. M. Zysk, E. J. Chaney, J. G. Kotynek, U. J. Oliphant, F. J. Bellafiore, K. M. Rowland, and P. A. Johnson, "Coherent optical imaging and guided interventions in breast cancer: translating technology into clinical applications," *Proc. SPIE 6991, Biophotonics: Photonic Solutions for Better Health Care*, 699102, 2008.

[71] R. L. van Veen, H. J. Sterenborg, A. W. Marinelli, and M. Menke-Pluymers, “Intraoperatively assessed optical properties of malignant and healthy breast tissue used to determine the optimum wavelength of contrast for optical mammography,” *J. Biomed Opt*., vol. 9, no. 6, pp. 1129-36, 2004.

[72] Chapter 1 Glycerol: Properties and Production, The Future of Glycerol, 2nd ed., The Royal Society of Chemistry, 2010.

[73] H. Q. Zhong, Z. Y. Guo, H. J. Wei, J. L. Si, L. Guo, Q. L. Zhao, C. C. Zeng, H. L. Xiong, Y. H. He , and S. H. Liu, “Enhancement of permeability of glycerol with ultrasound in human normal and cancer breast tissues *in vitro* using optical coherence tomography,” *Laser Physics Letters*, vol. 7, no. 5, pp. 388-395, 2010.

[74] A. S. Kolesnikov, E. A. Kolesnikova, A. P. Popov, M. M. Nazarov, A. P. Shkurinov, and V. V. Tuchin, “In vitro terahertz monitoring of muscle tissue dehydration

under the action of hyperosmotic agents," *Quantum Electronics*, vol. 44, no. 7, pp. 633-640, 2014.

[75] S. J. Oh, S. H. Kim, K. Jeong, Y. Park, Y. M. Huh, J. H. Son, and J. S. Suh, "Measurement depth enhancement in terahertz imaging of biological tissues," *Opt. Express*, vol. 21, pp. 21299-21305, 2013.

[76] N. Vohra, K. Bailey, and M. El-Shenawee, "Dehydration Approach for Enhancing Terahertz Detection of Cancer in Freshly Excised Breast Tumors," *Proc. of IEEE-APS/URSI* 2020, Montreal, Quebec, Canada, 5-10 July 2020.

[77] Z. Sun, G. Bebis, and R. Miller, "On-road vehicle detection: A review," *IEEE Trans. Pattern Anal. Mach. Intell.*, vol. 28, no. 5, pp. 694–711, May 2006.

[78] M. Goppelt, H.-L. Blöcher, and W. Menzel, "Automotive radar Investigation of mutual interference mechanisms," *Adv. Radio Sci.*, vol. 8, pp. 55–60, 2010.

[79] D. C. Schleher, Electronic Warfare in the Information Age, London: Artech House, 1999.

[80] S. A. Silva, J. J. Pereira, E. L. Nohara, and M. C. Rezende, "Electromagnetic behavior of microwave absorbing materials based on Ca hexaferrite modified with CoTi ions and doped with La," *Journal of Aerospace Technology and Management*, vol. 1, no. 2, pp. 255-263, 2009.

[81] D. D. L. Chung, "Electromagnetic interference shielding effectiveness of carbon materials," *Carbon*, vol. 39, no. 2, pp. 279-285, 2001.

[82] M. H. Al-Saleh, W. H. Saadeh, and U. Sundararaj, "EMI shielding effectiveness of carbon based nanostructured polymeric materials: A comparative study," *Carbon*, vol. 60, no. 8, pp. 146-156, 2013.

[83] D. Balageas and P. Levesque "EMIR: A photothermal tool for electromagnetic phenomena characterization", *Revue Generale de Thermique*, vol. 37, no. 9, pp. 725-739, 1998.

[84] B. G. M. Helme, "Measurement of the microwave properties of materials," *IEE Colloquium on Industrial Uses of Microwaves*, London, UK, pp. 3/1-3/7, 1990.

[85] L. F. Chen, C. K. Ong, C. P. Neo, V. V. Varadan, V. K. Varadan, Microwave Electronics: Measurement and Materials Characterization, John Wiley & Sons, 2004.

[86] Von Hippel, A.R. Dielectric Materials and Applications; Artech House: Dedham, MA, USA, Volume 2, 1954.

[87] J. Barker-Jarvis, R. G. Geyer, J. H. Grosvenor, M. D. Janezic, C. A. Jones, B. Riddle, C. M. Weil, and J. Krupka, "Dielectric characterization of low-loss materials—A comparison of techniques," *IEEE Trans. Dielectr. Electr. Insul.*, vol. 5, no. 4, pp. 571–577, 1998.

[88] J. Obrzut, C. Emiroglu, O. Kirillov, Y. Yang, and R. E. Elmquist, “Surface conductance of graphene from non-contact resonant cavity,” *Measurement*, vol. 87, pp. 146–151, Jun. 2016.

[89] C. L. Pournaropoulos and D. K. Misra, “The co-axial aperture electromagnetic sensor and its application in material characterization,” *Measurement Science and Technology*, vol. 8, no. 11, pp. 1191-1202, 1997.

[90] S. Mueller, A. Penirschke, C. Damm, P. Scheele, M. Wittek, C. Weil, and R. Jakoby, "Broad-band microwave characterization of liquid crystals using a temperature-controlled coaxial transmission line," *IEEE Transactions on Microwave Theory and Techniques*, vol. 53, no. 6, pp. 1937-1945, 2005.

[91] N. Williams, V. K. Varadan, D. Ghodgaonkar, and V. V. Varadan, “Measurement of transmission and reflection of conductive lossy polymers at millimeter-waves frequencies*,” IEEE Trans. Electromagn. Compat*., vol. 32, no. 3, pp. 236–240, 1990.

[92] S. Sahin, N. K. Nahar, and K. Sertel, “A Simplified Nicolson–Ross–Weir Method for Material Characterization Using Single-Port Measurements,” *IEEE Transactions on Terahertz Science and Technology*, vol. 10, no. 4, pp. 404-410, 2020.

[93] F. Costa, M. Borgese, M. Degiorgi, and A. Monorchio, “Electromagnetic Characterisation of Materials by Using Transmission/Reflection (T/R) Devices,” *Electronics*, vol. 6, no. 95, pp. 1-27, 2017.

[94] D. H. Whiffen and H. W. Thompson, “Dielectric Properteis of Water,” *Trans. Faraday Soc.*, no. D, 1946.

[95] R. L. Smith-Rose, “Radio-Wave Propagation Research in the Department of Scientific and Industrial Research During the Years 1937-46,” *Inst. Electr. Eng*., vol. 94, no. 16, pp. 879-892, 1947.

[96] B. A. Lengyel, "A Michelson-Type Interferometer for Microwave Measurements," *Proceedings of the IRE*, vol. 37, no. 11, pp. 1242-1244, 1949.

[97] W. Culshaw, “A Spectrometer for Millimetre Wavelengths,” *Journal of the Institute of Electrical Engineers*, vol. 100, no. 3, pp. 5-14, 1953.

[98] W. Culshaw, “High Resolution Millimeter Wave Fabry-Perot Interferometer,” *IRE Trans. Microw. Theory Tech.*, vol. 8, no. 2, pp. 182–189, 1960.

[99] W. Culshaw and M. V. Anderson, “Measurement of Permittivity and Dielectric Loss with a Millimetre-wave Fabry-Perot Interferometer,” *Inst. Electr. Eng.*, vol. 109, no. 23S, pp. 820–826, 1962.

[100] A. M. Nicolson, “Broad-Band Microwave Transmission Characteristics from a Single Measurement of the Transient Response,” *IEEE Trans. Instrum. Meas.*, vol. 17, no. 4, pp. 395–402, 1968.

[101] A. M. Nicolson and G. F. F. Ross, “Measurement of the Intrinsic Properties of Materials by Time-Domain Techniques,” *IEEE Trans. Instrum. Meas.*, vol. 19, no. 4, pp. 377–382, 1970.

[102] W. B. Weir, “Automatic Measurement of Complex Dielectric Constant and Permeability,” *Proc. IEEE*, vol. 62, no. 1, pp. 33–36, 1974.

[103] A. L. Cullen, “A New Free-wave Method for Ferrite Measurement at Millimeter 104 Wavelengths,” *Radio Sci.*, vol. 22, no. 7, pp. 1168–1170, 1987.

[104] D. K. Ghodgaonkar, V. V. Varadan, and V. K. Varadan, “A Free-Space Method for Measurement of Dielectric Constants and Loss Tangents at Microwave Frequencies,” *IEEE Trans. Instrum. Meas.*, vol. 38, no. 3, pp. 789–793, 1989.

[105] V. V. Varadan, V. K. Varadan, and D. K. Ghodgaonkar, “5-100GHz free-space microwave characterization setup,” *Proc. SPIE 1307, Electro-Optical Materials for Switches, Coatings, Sensor Optics, and Detectors*, 1990.

[106] D. K. Ghodgaonkar, V. V. Varadan, and V. K. Varadan, “Free-Space Measurement of Complex Permittivity and Complex Permeability of Magnetic Materials at Microwave Frequencies,” *IEEE Trans. Microw. Theory Tech.*, vol. 39, no. 2, pp. 387–394, 1990.

[107] M. S. Hilario, B. W. Hoff, B. Jawdat, M. T. Lanagan, Z. W. Cohick, F. W. Dynys, J. A. Mackey, and J. M. Gaone, “W-Band Complex Permittivity Measurements at High Temperature Using Free-Space Methods,” *IEEE Transactions on Components, Packaging and Manufacturing Technology*, vol. 9, no. 6, pp. 1011-1019, 2019.

[108] Z. Qamar, N. Aboserwal, and J. L. Salazar-Cerreno, “An Accurate Method for Designing, Characterizing, and Testing a Multi-Layer Radome for mm-Wave Applications,” *IEEE Access*, vol. 8, pp. 23041-23053, 2020.

[109] T. Ozturk, A. Elhawil, I. Uluer, and M. T. Guneser, “Development of extraction techniques for dielectric constant from free-space measured S-parameters between 50 and 170 GHz,” *J. Mater Sci.: Mater. Electron*, vol. 28, pp. 11543–11549, 2017.

[110] T. Ozturk, O. Morikawa, I. Ünal, and I. Uluer, “Comparison of Free Space Measurement Using a Vector Network Analyzer and Low-Cost-Type THz-TDS Measurement Methods Between 75 and 325 GHz,” *J. Infrared Milli. Terahz. Waves*, vol. 38, pp. 1241–1251, 2017.

[111] H. Ahmed, J. Hyun, and J-Ryul. Lee, “Development of scanning single port free space measurement setup for imaging reflection loss of microwave absorbing materials,” *Measurement*, vol. 125, pp. 114-122, 2018.

[112] Z. Akhter and M. J. Akhtar, "Free-Space Time Domain Position Insensitive Technique for Simultaneous Measurement of Complex Permittivity and Thickness of Lossy Dielectric Samples," *IEEE Transactions on Instrumentation and Measurement*, vol. 65, no. 10, pp. 2394-2405, 2016.

[113] V. V. Varadan, K. A. Jose and V. K. Varadan, "In situ microwave characterization of nonplanar dielectric objects," *IEEE Transactions on Microwave Theory and Techniques*, vol. 48, no. 3, pp. 388-394, 2000.

[114] F. C. Smith, B. Chambers, and J. C. Bennett, "Methodology for accurate free-space characterisation of radar absorbing materials," *Proc. Inst. Elect. Eng.—Sci., Meas., Technol.*, vol. 141, no. 6, pp. 538–546, 1994.

[115] D. V. Blackham, "Free space characterization of materials," *Proc. Antenna Meas. Techn. Assoc. Symp.*, vol. 15, pp. 58–60, 1993.

[116] A. M. Hassan, J. Obrzut, and E. J. Garboczi, "A Q-Band FreeSpace Characterization of Carbon Nanotube Composites," *IEEE Trans. Microwave Theory & Tech*, vol. 64, no. 11, pp. 3807-3819, 2016.

[117] N. Vohra, L. R. Rodriguez-Aguilar, J. S. Batista, and M. El-Shenawee, "Free-Space Characterization of Radar Absorbing Non-Magnetic Materials in the W-Band," *Proc. of ARFTG 2020*, San Antonio, TX, 26-29 Jan 2020.

[118] N. Vohra, J. S. Batista, and M. El-Shenawee, "Characterization of Radar Absorbing Materials at 75 GHz – 90 GHz using Free-Space System," *Proc. of IEEE-APS/URSI* 2020, Montreal, Quebec, Canada, 5-10 July 2020.

[119] C. E. Kintner, "Free-Space Measurements of Dielectrics and Three-Dimensional Periodic Metamaterials," University of Arkansas, 2017.

[120] N. Vohra, T. Bowman, K. Bailey, and M. El-Shenawee, "Terahertz Imaging and Characterization Protocol for Freshly Excised Breast Cancer Tumors," *J. Vis. Exp.* issue. 158, e61007, 2020.

[121] N. Vohra, T. Bowman, P. M. Diaz, N. Rajaram, K. Bailey, and M. El- Shenawee, "Pulsed terahertz reflection imaging of tumors in a spontaneous model of breast cancer," Biomedical Physics and Engineering Express, vol 4, no. 6, pp. 065025, 2018.

[122] N. Vohra, T. Chavez, J. R. Troncoso, N. Rajaram, J. Wu, P. N. Coan, T. A. Jackson, K. Bailey, and M. El-Shenawee, "Mammary tumors in Sprague Dawley rats induced by N-ethyl-N-nitrosourea for evaluating terahertz imaging of breast cancer," *J. Med. Imag.* vol. 8, no.2, pp. 023504, 2021.

[123] N. Vohra and M. El-Shenawee, "K- and W-Band Free-Space Characterizations of Highly Conductive Radar Absorbing Materials," *IEEE Transactions on Instrumentation and Measurement*, vol. 70, pp. 1-10, Art no. 8001910, 2021.

CHAPTER 2

Terahertz Imaging and Characterization Protocol for Freshly Excised Breast Cancer Tumors

Abstract

This manuscript presents a protocol to handle, characterize, and image freshly excised human breast tumors using pulsed terahertz imaging and spectroscopy techniques. The protocol involves terahertz transmission mode at normal incidence and terahertz reflection mode at an oblique angle of 30°. The collected experimental data represent time domain pulses of the electric field. The terahertz electric field signal transmitted through a fixed point on the excised tissue is processed, through an analytical model, to extract the refractive index and absorption coefficient of the tissue. Utilizing a stepper motor scanner, the terahertz emitted pulse is reflected from each pixel on the tumor providing a planar image of different tissue regions. The image can be presented in time or frequency domain. Furthermore, the extracted data of the refractive index and absorption coefficient at each pixel are utilized to provide a tomographic terahertz image of the tumor. The protocol demonstrates clear differentiation between cancerous and healthy tissues. On the other hand, not adhering to the protocol can result in noisy or inaccurate images due to the presence of air bubbles and fluid remains on the tumor surface. The protocol provides a method for surgical margins assessment of breast tumors.

Video Link

The video component of this article can be found at https://www.jove.com/video/61007/

Introduction

Terahertz (THz) imaging and spectroscopy has been a rapidly growing area of research in the past decade. The continued development of more efficient and consistent THz emitters in the range of 0.1 THz–4 THz has made their applications grow significantly [1]. One area where THz has shown promise and significant growth is the biomedical field [2]. THz radiation has been shown to be nonionizing and biologically safe at the power levels generally used to analyze fixed tissues [3]. As a result, THz imaging and spectroscopy has been used to classify and differentiate various tissue features such as water content to indicate burn damage and healing [4], liver cirrhosis [5], and cancer in excised tissues [6, 7]. Cancer assessment in particular covers a broad range of potential clinical and surgical applications, and has been investigated for cancers of the brain [8], liver [9], ovaries [10], gastrointestinal tract [11], and breast [7, 12-19].

THz applications for breast cancer are primarily focused on supporting breast conserving surgery, or lumpectomy, via margin assessment. The objective of a lumpectomy is to remove the tumor and a small layer of surrounding healthy tissue, in contrast to full mastectomy, which removes the entire breast. The surgical margin of the excised tissue is then assessed via pathology once the sample has been fixed in formalin, sectioned, embedded in paraffin, and mounted in 4 µm–5 µm slices on microscope slides. This process can be time-consuming and requires a secondary surgical procedure at a later time if a positive margin is observed [20]. Current guidelines by the American Society of Radiation Oncology define this positive margin as having cancer cells contacting the surface-level margin ink [21]. THz imaging for high-absorption hydrated tissue is primarily limited to surface imaging with some varying penetration based on tissue type, which is sufficient for meeting the surgical needs of rapid margin assessment. A quick analysis of margin conditions during the surgical setting would greatly decrease surgical costs and

follow-up procedure rate. To date, THz has proven effective in differentiating between cancer and healthy tissue in formalin-fixed, paraffin-embedded (FFPE) tissues, but additional investigation is needed to provide reliable detection of cancer in freshly excised tissues [7].

This protocol details the steps for performing THz imaging and spectroscopy on freshly excised human tissue samples obtained from a biobank. THz applications built on freshly excised human breast cancer tissues have seldom been used in published research [7, 18, 22, 23], especially by research groups not integrated with a hospital. The use of freshly excised tissues is likewise rare for other cancer applications, with most non-breast human cancer examples being reported for colonic cancer [24, 25]. One reason for this is that FFPE tissue blocks are far easier to access and handle than freshly excised tissue unless the THz system being used for the study is part of the surgical workflow. Similarly, most commercial laboratory THz systems are not prepared to handle fresh tissue, and those that do are still in the stages of using cell line growth or have only started to look at excised tissue from animal models. To apply THz to an intraoperative setting requires that imaging and characterization steps be developed for fresh tissue in advance so that the analysis does not interfere with the ability to perform standard pathology. For applications that are not inherently meant to be intraoperative, the characterization of fresh tissue is still a challenging step that must be addressed to work towards in vivo applications and differentiation.

The objective of this work is to provide a guideline for THz application for freshly excised tissue using a commercial THz system. The protocol was developed on a THz imaging and spectroscopy system [26] for murine breast cancer tumors [13, 17, 19] and was extended to human surgical tissue obtained from biobanks [7, 18]. While the protocol was generated for breast cancer, the same concepts can be applied to similar THz imaging systems and other types of solid-tumor cancers that are treated with surgery where success depends on margin assessment [27]. Due to a

fairly small amount of published THz results on freshly excised tissues, this is the first work to the authors' knowledge to focus on the protocol of fresh tissue handling for THz imaging and characterization.

PROTOCOL

This protocol follows all the requirements set by the Environmental Health and Safety department at the University of Arkansas.

1. Set Up the Tissue Handling Area

1. Take a stainless-steel metal tray and cover it with the biohazard bag as shown in **Figure 1**. Any handling of the biological tissues will be performed within the tray area (i.e., the tissue handling area).
2. Prepare laboratory tweezers, tissue wipes, paper towels, filter paper pack, tissue dye bottles, bleach bottle, and ethanol bottle around the tray for easy access when required. Keep any used tissues, wipes, and gloves on the biohazard material surface to dispose of at the end of the protocol.
3. Fill a 50 mL centrifuge tube with up to 45 mL of 10% neutral buffered formalin and place it

Figure 1: Setup of tissue handling area.

in the centrifuge storage tray near the tissue handling tray.

2. Handling Fresh Breast Cancer Tumor for THz Transmission Spectroscopy

CAUTION: Before handling any live tissues, put on nitrile hand gloves, eye protection goggles, a face mask, and a lab coat. Always use laboratory tweezers to handle tissues and avoid touching them directly with the hands. All work with fresh tissue outside of a sealed container or the scanning stage should be conducted at the tissue handling area established in step 1.1.

NOTE: All tissues handled in this work were shipped in Dulbecco's Modified Eagle's medium (DMEM) and antibiotic solution from the biobank.

1. Remove the bulk tumor from the DMEM solution and place it in a Petri dish on the tissue handling area (see **Figure 2A**).
2. From gross inspection, identify distinct tumor regions from which to slice small pieces for transmission characterization. Cut a 0.5 mm thick segment of tumor from the identified points using a stainless steel low profile blade, as shown in **Figure 2B**. Place this sliced section between two quartz windows with a spacer of 0.1 mm thickness in a liquid sample holder, as shown in **Figure 2C**.

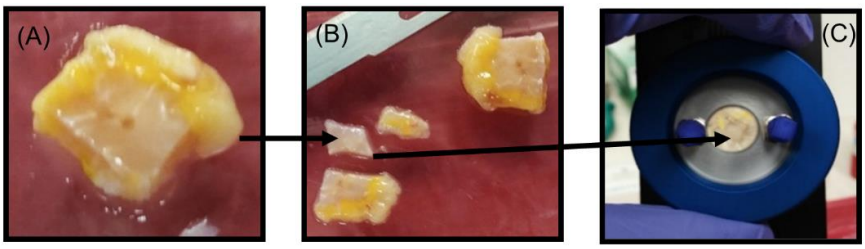

Figure 2: Tumor sectioning for the THz transmission spectroscopy measurements. (**A**) Photograph of the bulk tumor. (**B**) Photograph of the small sections (0.5 mm) of the tumor cut from the bulk tumor. (**C**) The sliced tumor section placed in the liquid sample holder between the two quartz windows with a 0.1 mm polytetrafluoroethylene spacer for spectroscopy measurement. Figure republished from T. Bowman et al. 18 with permission from SPIE.

3. THz Transmission Spectroscopy Measurements

1. Set the transmission spectroscopy module inside the THz core chamber by aligning the

module handles over the mounting posts in the core system and sliding the stage down into the system. Tighten the two mounting screws in the upper right and lower left corners of the module as shown in **Figure 3A**.

2. Purge the system with dry nitrogen gas at 5 L/min (LPM) during the entire spectroscopy procedure to remove water vapor from the sample space.
3. Open the THz transmission spectroscopy measurement software from the desktop connected to the THz system. It will open up the main window.
4. Click on the Scan tab on the top of the window. A Spectra Scan Setup window will appear. From the drop-down menu of the **Measurement Mode** tab on the top right of the window, select **Transmission** to set up transmission spectroscopy. If the peak is not automatically visible, check the **Enable** option under the **Manual Peak Search** tab and manually step the optical delay to bring the peak into view.
5. **After 30 min of purging, record an air reference signal by following the steps below**.
    1. Under the **Scan Settings** tab in the spectra scan setup window, input an appropriate **Name** for the reference file, set **Num Scans** to 1,800, and set the **Start Delay** (**s**) to 0. Leave the other settings as their default values.

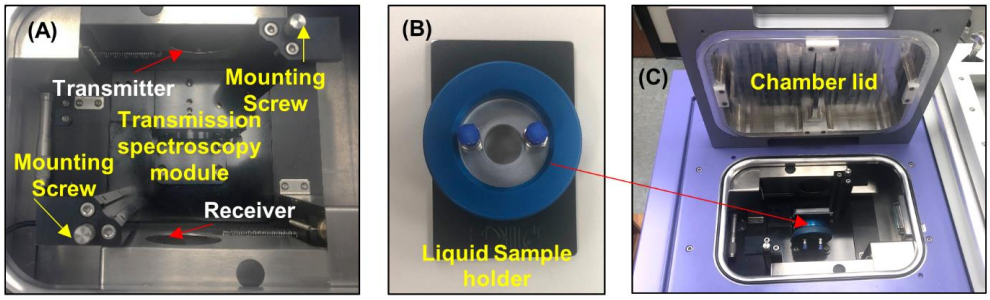

Figure 3: THz transmission spectroscopy module setup. (**A**) THz core chamber with the transmission module mounted on it. (**B**) A photograph of the liquid sample holder. (**C**) The sample holder placed inside the core chamber for the measurements.

    2. Click on **Measure Reference** in the scan setup window to take the air reference measurement. Then click on **Measure Sample** to measure the transmission signal

through air as a sample average of 1,800 signals over ~1 min.

6. **Measure the two quartz windows in the liquid sample holder as shown in Figure 3B**.
    1. Place the two quartz windows in the liquid sample holder without a spacer in between.
    2. Open the THz core chamber. Mount the liquid sample holder on the transmission spectroscopy module, as shown in **Figure 3C**. Close the chamber.
    3. Click on the **Scan** tab on the main window. Repeat steps 3.5.1–3.5.2 for the quartz sample, but update **Start Delay** (**s**) to 900. This allows time to purge any water vapor before measurement.
    4. If the quartz is desired as a reference for additional samples, click on the **Clear Reference** tab under the **Scan Settings**. This clears the air reference. Then click on the **Measure Reference** tab to record the quartz measurements as a new reference.
7. Place the sliced tumor section between the two quartz windows inside the liquid sample holder and position the holder inside the chamber for a single point transmission measurement of the tissue. To record the measurement, repeat step 3.6.3.
8. Take the liquid sample holder out of the chamber when the measurements are completed and bring it to the area designated for tissue handling. Disassemble the liquid sample holder, wipe the tumor section from the quartz windows with the tissue wipes, and place the used tissue wipes in the same tray to dispose in the biohazard bag along with the other biohazard waste.
9. Repeat steps 2.2, 3.7, and 3.8 as necessary to characterize additional tumor slices. When the measurements are completed, go to the main window and click on the **File** tab to save the measurement data. Close the software window.

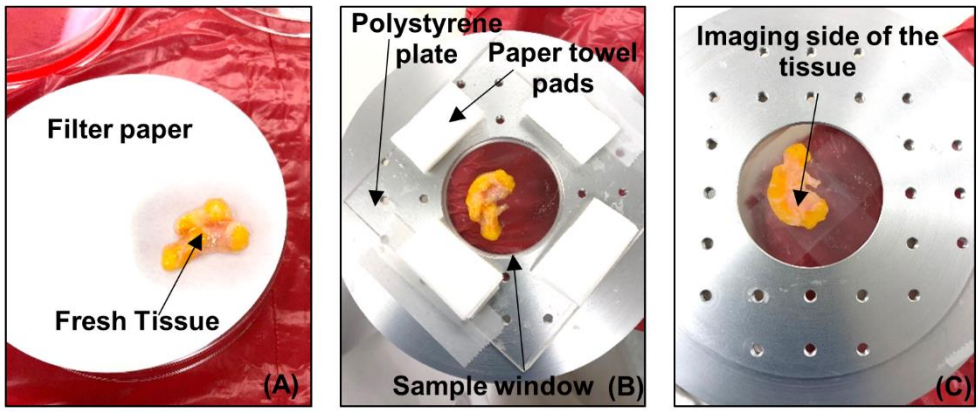

Figure 4: Fresh tumor sample preparation for THz imaging. (**A**) Tumor placed on filter paper to dry. (**B**) Tumor placed on polystyrene plate over the imaging window with tissue wipe pads to absorb excess fluids. (**C**) Tumor viewed from below to track orientation and check for air bubbles.

4. Handling Fresh Breast Cancer Tumor for THz Reflection Mode Imaging

1. Remove the fresh tumor sample from the DMEM and antibiotics solution and place it on a Petri dish. Using gross inspection, select a side of the tumor to be imaged that is sufficiently flat and has little blood and few blood vessels. Avoid imaging tissue with blood or blood vessels if possible.
2. Place the tumor with the side to be imaged on grade 1 filter paper to dry the excess DMEM and clear the tissue of fluid or secretions from the tumor, as shown in **Figure 4A**. Reposition the tumor on the filter paper to a dry spot as the paper saturates. Dry the tumor for ~5 min.
3. Unmount the transmission spectroscopy module and set the reflection imaging module (RIM) mirror base on the THz core system as shown in **Figure 5A**. Upon setting the mirrors, mount the RIM scanning stage above the mirror base and screw it into the core system (see **Figure 5B**).
4. Purge the system with dry nitrogen gas at 5 LPM for 30 min prior to the imaging procedure to remove water vapor from the sample compartment. After 30 min, reduce the amount of dry nitrogen gas to 3 LPM for the rest of time the system is in use.

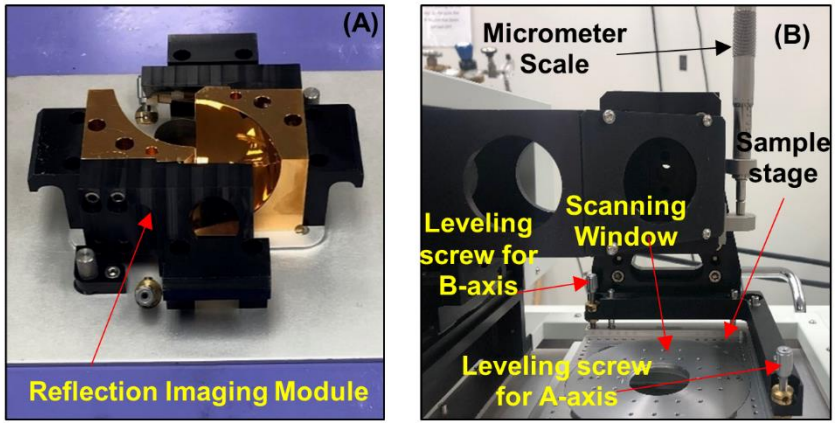

Figure 5: System setup for reflection imaging. (**A**) Reflection imaging module mirror base. (**B**) Scanning stage.

5. Place a polystyrene plate of thickness ~1.2 mm on the scanning window of diameter ~37 mm. Center the scanning window along with the polystyrene plate on the sample stage.

NOTE: Other thicknesses and plate materials are suitable for step 4.5 but should have a uniform thickness and be of low enough absorption to not impede the THz signal.

6. Open the THz reflection imaging measurement software from the desktop connected to the THz system. A window will pop up showing several dialog icons for specific functions and two sub windows for THz field plots, (arbitrary units' a.u.) against the time and frequency, respectively.

7. To set the parameters for the RIM set-up, click on the **Image Parameter Dialog** icon at the top of the window. An **Image Acquisition Parameters** window will pop up. Select **RIM** from the drop-down menu of the **Template** tab for reflection imaging set up. Hit **OK** and go back to the main window of the software.

8. On the main window, click on the **Fixed-point Scan** icon. This will activate the THz antennas to start sending the incident THz signal and receiving the reflected THz signal from a single point on the polystyrene plate.

9. Click on the **Motor Stage Dialog** icon on the top of the main window. The motor control window will open up. Adjust the optical delay axis by clicking on the **forward/reverse direction arrows** to center the reflected pulse from the polystyrene in the main window.

NOTE: After adjusting the optical delay axis, two pulses should appear on the window, as shown in **Figure 6**: one from the lower interface of the polystyrene plate (primary reflection), and one from the upper interface of the polystyrene plate (secondary reflection).

10. **Window out the primary reflection from the polystyrene plate and keep the secondary reflection in the window, which will contribute to the reflections from the tissue during the imaging procedure. This is done in two steps**.

    1. First, click on the **DAQ Settings** button at the top of the main window to open the DAQ settings dialog window. Change the optical delay value from 5 V (default) to 4 V.
    2. Second, adjust the scanning stage's vertical position with the micrometer scale on the scanning stage until the minima of the secondary pulse is the strongest. Adjust the optical delay of the axis in the **Motor Control Window** to put the primary reflection outside of the range of the reflected signal being measured.

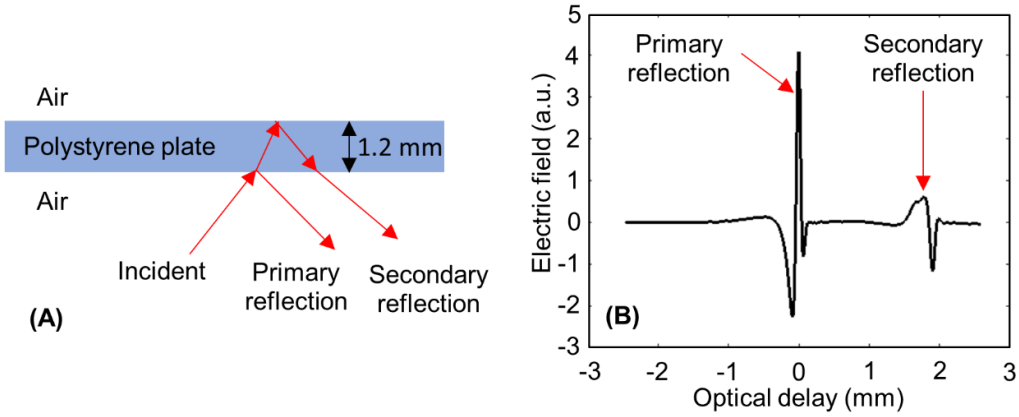

Figure 6: THz reflections from the lower and upper interfaces of the polystyrene plate. (**A**) THz signal incident to and reflected from a 1.2 mm thick polystyrene plate. (**B**) Measured primary and secondary THz time domain signals from the polystyrene.

NOTE: For a 1.2 mm thick polystyrene plate, the primary reflection is windowed out when the secondary reflection minimum peak is approximately -0.3 mm on the optical delay axis of the time domain window.

11. **Level the sample stage and record the reference signal**.

    1. Select two points on each axis (A-axis and B-axis) that denote locations on the polystyrene plate near the edge of the sample window. For example, for the A-axis ranging from -15 mm–15 mm, the two position points can be -10 mm and 10 mm; and for the B-axis ranging from -15 mm–15 mm, the two position points can be -10 mm and 10 mm.
    2. Click on the **Motor Control Dialog** button to open the motor control window. Reposition the motor control window and the main software window so that the time domain signal is visible while adjusting the motor positions. Set both the A-axis and B-axis to 0 mm.
    3. Level the A-axis using following steps. A -10 mm–10 mm range is used as an example.
    4. In the **Motor Control Window**, change the value of the A-axis from 0 to -10 and hit **Enter**. The stage moves to the -10 mm position on the A-axis and a shift in the signal position on the main window is observed.
    5. Use the adjustable micrometer scale on the scanning stage shown in **Figure 5B** to move the minimum peak of the signal back to the position set in step 4.10.2.
    6. Change the A-axis value to +10 and hit enter. The stage will now move from the -10 mm position to the +10 mm position on the A-axis and a shift in the signal is observed again. Note the direction and the distance that the signal shifted from its previous position and change the A-axis value again to -10. The signal will go back to the position set in step 4.11.5.

7. Rotate the leveling screw on the A-axis of the scanning stage, as shown in **Figure 5B** and shift the signal to double the distance in the same direction it moved from the original position. Use the micrometer on the scanning stage to shift the signal back to the original position (-0.3 mm for 1.2 mm of polystyrene).
8. Repeat steps 4.11.6–4.11.7 until the signal at +10 and -10 are equal and the peak for both positions is focused at the original position (-0.3 mm on the optical axis).

12. Once the leveling of the A-axis is achieved, change the A-axis value to 0 and repeat the same procedure for the B-axis. Start by changing the value of the B-axis on the motor control window from 0 to the most positive value (for example +10 mm). Also, while leveling, use the leveling screw on the B-axis of the scanning stage, which is shown in **Figure 5B**.
13. Once both axes are leveled, return both the A-axis and the B-axis to 0 mm. Close the **Motor Control Window** and verify that the signal is in its original position in case it is shifted a little.
14. **Record this signal as the reference**.
    1. Go to the set **DAQ Properties window**. Change the averaging value to 5 and keep all other parameters as default.
    2. Click on **New Reference**. The averaging counter in the top right of the window will count from 0–20. Once the counter reaches 20, change the averaging value to 1 and click **OK**. The reflected signal from the polystyrene will be saved as the reference for any scans taken later.

    NOTE: If only the THz imaging procedure has to be performed, then it is best to perform steps 4.3–4.14 before taking the tumor tissue out of the DMEM solution.

15. **Mount the tumor on the polystyrene plate covering the scanning stage window**.
    1. Remove the imaging window from the scanning stage and bring it to the tissue handling area. Place the tumor on a polystyrene plate, as shown in **Figure 4B**.
    2. Ensure that there are no significant air bubbles between the plate and the tumor. If air bubbles are observed, press the tumor with tweezers or lift the tumor and gently roll it onto the polystyrene until the air gaps are minimized.
    3. Place absorptive spacers at regular intervals around the test sample as shown in **Figure 4B**. Place another polystyrene plate above the tumor and press gently in order to make the tumor surface as flat as possible. Tape down this polystyrene-tumor-polystyrene arrangement on the sample window.
16. Flip the sample window as shown in **Figure 4C**, and take photos of the tumor to keep a record of its orientation. Return the sample window with the tumor to the scanning stage.
17. Click on the **Image Parameter Dialog** button to open the **Image Acquisition Parameters** window. Set the values of **Axis1min**, **Axis1max**, **Axis2min**, and **Axis2max** to fully enclose the position of the tumor in the imaging window.

    NOTE: By default, Axis1 is the A-axis and Axis2 is the B-axis.
18. Set **Axis1step** and **Axis2step** to 0.2 mm for the imaging scan.

    NOTE: Setting the **Axis1step** and **Axis2step** will set the stepper motors' step size to 200 µm increments during the scanning process. The total scan time can be estimated in the **Image Acquisition Parameters** window.
19. Click on the **Measure** tab on the main window and select the **Flyback 2D Scan** option. In the window that pops up, indicate the directory and file name under which to save the scan data.

5. Postprocessing the Fresh Tissue in Preparation for Histopathology Procedure

1. Upon completion of the scanning process, remove the sample window, polystyrene plates, and sample from the core THz system and move them to the area designated for hazardous waste. Remove the tumor from the polystyrene plate and place it on a flat piece of cardboard of a size comparable to that of the tumor. Make sure the orientation of the tumor is the same as it was on the polystyrene, with the imaging face touching the cardboard.

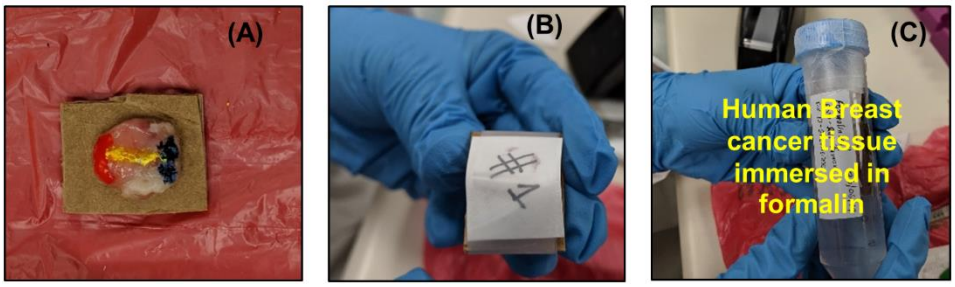

Figure 7: Post processing on the tumor after THz imaging. (**A**) Tumor placed face down on cardboard holder and dyed with tissue marking dye. (**B**) Filter paper placed over tumor and taped to maintain contact. (**C**) Stained tumor fixed on the cardboard immersed in 10% neutral buffered formalin solution and sealed with parafilm.

2. Dip a cotton swab in red tissue dye and stain the left side of the tumor down to where the edge of the tumor contacts the cardboard. Similarly, stain the right side of the tumor with blue tissue dye. Stain the exposed surface of the tumor with a line of yellow tissue dye connecting the red stain to the blue stain to denote the back of the sample, as shown in **Figure 7A**.

   NOTE: To prevent the ink from staining the formalin solution, apply only a thin layer to the tissue. This can be accomplished by dabbing the cotton swab on a different surface before staining the tissue or using a clean cotton swab to wipe off any excess dye. Avoid letting the dye contact the skin or clothing. This tumor-staining process is conducted as a reference to provide information about the tumor's imaging side and its orientation to the pathologist.

3. Let the ink dry for around 3–4 min. Cut a piece of filter paper with the same approximate dimensions as the cardboard. Place it on the tumor and wrap a piece of tape completely around

the filter paper and cardboard as shown in **Figure 7B**. The tape and filter paper should secure the tumor against the cardboard without applying any significant pressure.

4. Immerse the stained tissue affixed to the cardboard in 10% neutral buffered formalin solution and seal the centrifuge tube using a paraffin film, as shown in **Figure 7C**. Designate the sample number, date, tissue type, and tumor number for the sample on the tube label. Send the tumor to the pathologist for further histopathology processing.

6. Hazardous Waste Disposal

1. Collect all the waste from the tissue handling tray along with the biohazard bag used to cover

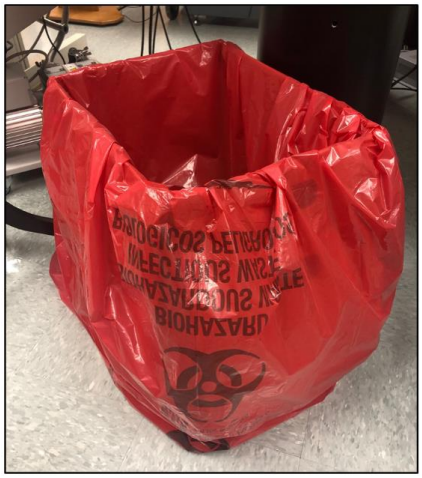

Figure 8: Photograph of the biohazardous waste bag.

the tray and put it in a new biohazard bag, as shown in **Figure 8**. Bring the bag to the designated biohazardous waste area in the building and set an appointment with the Environmental Health and Safety (EH&S) department for the waste pickup. Clean the tissue handling tray and the surrounding area on the table with 10% bleach solution and ethanol.

2. Take the liquid sample holder with the spacers and quartz windows, sampling window on which tumor was mounted, polystyrene plates, and laboratory tweezers to the washing area. Rinse all materials with water and then 10% bleach solution, wiping with paper towels as necessary to remove tissue debris. Rinse again with water, scrub with alconox solution, and

rinse thoroughly. For glass and plasticware, rinse in 70% isopropyl alcohol and set aside to dry.

NOTE: Once the tumor is in formalin and the sample space is clean, data processing can be handled at the same time as imaging or a later time.

7. Data Processing to Construct THz images

1. Export the saved .tvl data files from the THz system. The raw data files obtained from the system are written in Python and are best read in Python before saving as MATLAB data files.
2. To construct the THz image of the scanned fresh tissue, convert the raw time domain reflection imaging data into the frequency domain using Fourier transform on the third dimension of the raw data matrix (i.e., the time dimension). Also take the Fourier transform of the reference data.

   NOTE: A typical frequency domain spectrum should provide data ranging from 0.1 THz–4 THz.
3. Normalize the sample data with the reference data and perform the power spectra based on the integration of the normalized data over the frequency range from f1 = 0.5 THz to f2 = 1.0 THz using the following equation [19]:

$$Power\ Spectra\ = \int_{f_1}^{f_2} \left|E_{sample}\right|^2 / \left|E_{reference}\right|^2 df_{THz} \qquad (1)$$

NOTE: Here E_{sample} is the frequency domain reflection imaging data of the tissue sample and $E_{reference}$ is the frequency domain of a single point reflection data of the reference signal.

4. Construct the two-dimensional image by plotting the calculated power spectra data at each point in the matrix defined by the A-axis and Baxis. This is known as the power spectra THz image.

   NOTE: The method to obtain a tomographic THz image instead is detailed in steps 7.5–7.7.

5. For characterization, calculate the theoretical frequency-dependent reflection for a range of potential tissue properties using the following equation [18]:

$$\left(\frac{E_{samp}}{E_{ref}}\right)_T = \frac{\tilde{\Gamma}_{T,2,samp}}{\tilde{\Gamma}_{T,2,ref}} = \left(\frac{\rho_{T,23} - \rho_{T,31}e^{-j2\tilde{k}_3 \cos\theta_3 d_3}}{1 + \rho_{T,23}\rho_{T,31}e^{-j2\tilde{k}_3 \cos\theta_3 d_3}}\right) / \rho_{T,21} \quad (2)$$

NOTE: Here $\rho_{T,ij}$ is the complex Fresnel reflection coefficient between region i and region j; d_j is the thickness of region j; and θ_j is the angle of propagation in region j related to the angle of incidence by Snell's Law. is the complex propagation coefficient in region j, where ω is the angular frequency, c is the speed of light in vacuum, n_j is the real part of the refractive index, and $\alpha_{abs,j}$ is the absorption coefficient [18] . Region 1 is air, Region 2 is the polystyrene plate, and Region 3 is the tissue.

6. Calculate the reflection in equation (2) for a range of user-defined refractive indexes and absorption coefficients for Region 3 (n_3 and $\alpha_{abs,3}$) and compare with the measured signal at each point to calculate the combined mean squared error for the magnitude and phase.

   NOTE: The solution for the refractive index and absorption coefficient is the pair of values that give the lowest error.

7. Construct the tomographic THz image from the extracted refractive index and absorption coefficient data (n_3 and $\alpha_{abs,3}$) at each pixel. Analyze the tumor regions by comparing with the pathology slide image obtained from the pathologist. Representative results are shown in **Figure 9**, with examples of insufficient adherence to the protocol in **Figure 10** and **Figure 11**.

8. Extraction of Electrical Properties of the Tissue Using Transmission Spectroscopy Data

1. On the main window of the THz transmission spectroscopy measurement software, go to the **File** tab and click on the **Export** option. A window will pop up to select the **Data Type** and **Sample** to export. Choose **Transmittance** and **Transmittance Phase** data types for the quartz and tissue sample measurements.
2. Calculate the theoretical frequency-dependent transmission for a range of potential tissue properties using the following equation [15]:

$$\frac{E_{samp}}{E_{ref}} = \tilde{\tau} e^{(\gamma_1 - \gamma_3)d} \tag{3}$$

   NOTE: Here is the ratio between Fresnel transmission coefficients for the sample and reference setups; γ_1 and γ_3 are the complex propagation constants of air and tissue, respectively; and d is the thickness of the tissue. The propagation constant in general is defined as $\gamma = j\frac{\omega}{c}\tilde{n}$, $\tilde{n}$ is the complex refractive index defined as $\tilde{n} = n - j\frac{c}{\omega}\frac{\alpha_{abs}}{2}$, where n is the real part of the refractive index; c is the speed of light; ω is the angular frequency; and α_{abs} is the absorption coefficient [15].
3. Calculate the combined mean squared error between the magnitude and phase of the transmission in equation (3) and the measurement data from the system for a range of user-defined n and α_{abs} values.

   NOTE: The solution for the refractive index and absorption coefficient is the pair of values that give the lowest error.
4. Plot the extracted refractive index and absorption coefficient data against the frequency range from 0.15–3.5 THz. Representative results are shown in **Figure 12**.

Representative Results

The THz imaging results [18] obtained following the abovementioned protocol of human breast cancer tumor specimen #ND14139 received from the biobank are presented in **Figure 9**. According to the pathology report, the #ND14139 tumor was a I/II grade infiltrating ductal

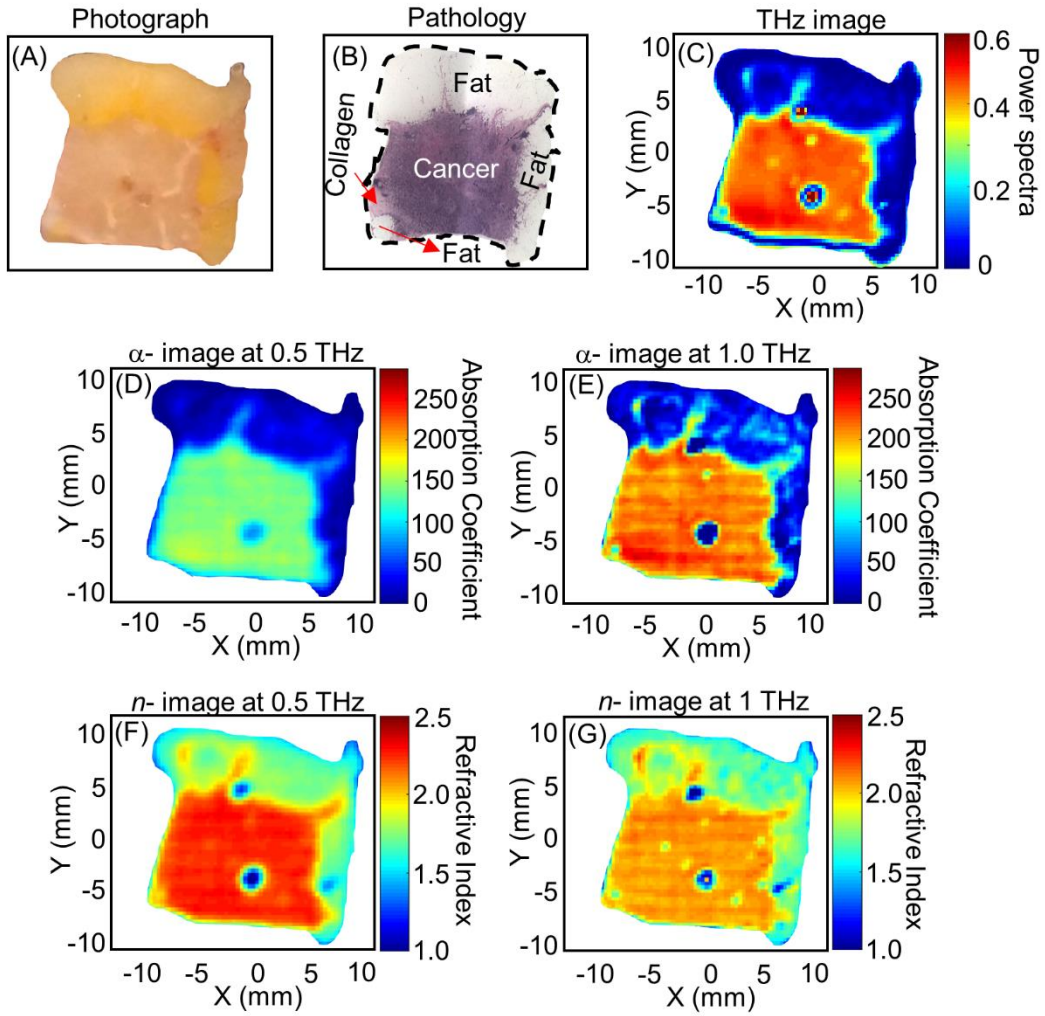

Figure 9: Analysis of breast cancer tumor #ND14139 using THz imaging technique. (**A**) Photograph of the tumor. (**B**) Low power pathology image of the tumor. (**C**) THz power spectra image over the frequency range 0.5 THz–1.0 THz. (**D**) THz tomographic absorption coefficient image obtained at 0.5 THz. This image was constructed using the extracted absorption coefficient data at each pixel from the raw reflection imaging data of the tumor. (**E**) Absorption coefficient image obtained at 1.0 THz. (**F**) Refractive index image (n- image) obtained at 0.5 THz. This image was constructed using the extracted refractive index data at each pixel from the raw reflection imaging data of the tumor. (**G**) Refractive index image (n- image) obtained at 1.0 THz. Figure republished from T. Bowman et al. [18] with permission from SPIE.

carcinoma (IDC) obtained from a 49-year-old woman via a left breast lumpectomy surgery procedure. The photograph of the tumor is shown in **Figure 9A**, the pathology image in **Figure 9B**, and the THz power spectra image obtained using equation (1) in the protocol is shown in **Figure 9C**. The assessment of the pathology image was done by our consulting pathologist at Oklahoma State University. Upon correlating the THz image with the pathology image, it was clear that the cancer region (i.e., the red color region in **Figure 9C**) showed higher reflection than the fat region (i.e., the blue color region in **Figure 9C**). The blue circle close to the center of the cancer region in Figure 9C w as due to the presence of an air bubble beneath the tumor during the imaging process.

Tomographic images based on the electrical properties of the tumor obtained using the above discussed model for each pixel (2,477 pixels in total) are also presented. The tomographic images based on the absorption coefficient (cm^{-1}) data (α- images) and refractive index (n- image) data of the tumor obtained at frequency 0.5 THz and 1.0 THz are shown in **Figure 9D**, **9E**, **9F**, and **9G**, respectively. As the frequency increased, the calculated absorption coefficient (cm^{-1}) values for the cancer and fat pixels increased, with cancer pixels showing higher values than fat at both frequencies. In contrast, the refractive index of both tissues decreased as the frequency increased. It should be noted that the measured phase became subject to micrometer-scale variations in the imaging stage leveling, polystyrene plate thickness, and stepper motor jitter as the frequency increased. For example, the horizontal lines observed in **Figure 9E** and **9G** were due to the small phase shift introduced by the stepper motors during the scanning process, which was not observed at lower frequencies.

The THz results discussed in **Figure 9** were obtained by successfully following the described protocol. Insufficient handling of the tissue can lead to misleading imaging results. For

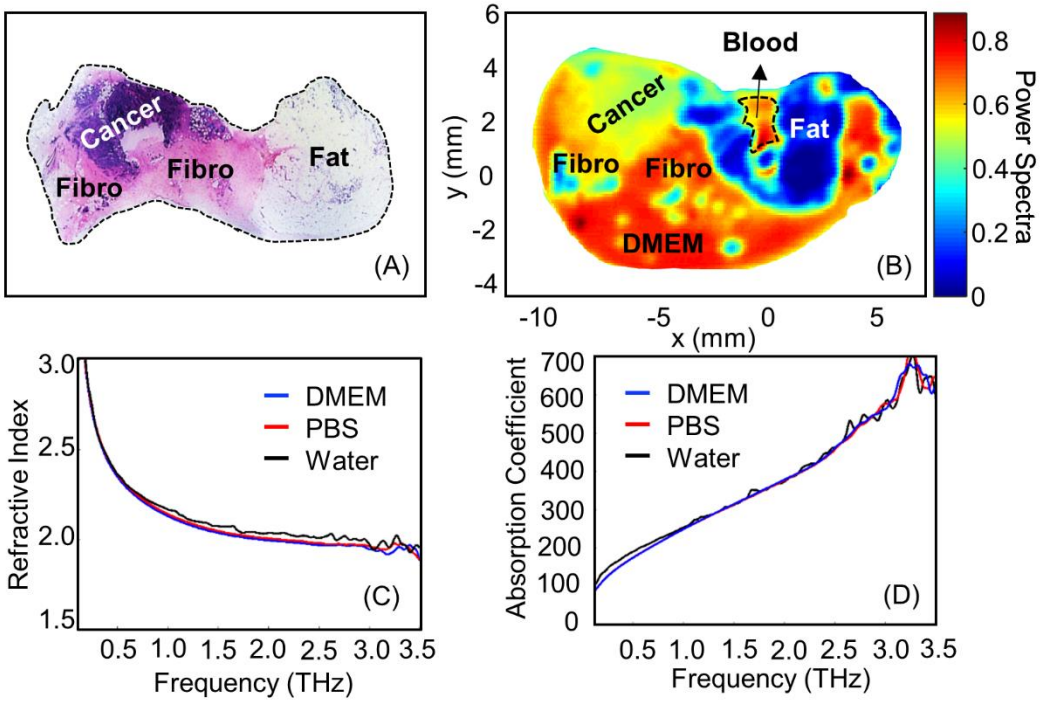

Figure 10: The effect on tumor imaging taken out of the DMEM solution without drying using filter paper. (**A**) Low power pathology image of the tumor #ND10405. (**B**) THz power spectra image of tumor #ND10405 over the frequency range 0.5 THz–1.0 THz. (**C**) The transmission refractive index plot for DMEM, PBS, and water ranging from 0.15 THz–3.5 THz. (**D**) The transmission absorption coefficient (cm –1) plot for DMEM, PBS, and water ranging from 0.15 THz–3.5 THz. Figure 10A, 10B are republished from T. Bowman et al. 28 with permission from IEEE and Figure 10C, Figure 10D are republished from N. Vohra et al. [19] with permission from IOP Publishing, Ltd.

example, the THz imaging results in **Figure 10** for human breast cancer tumor #ND10405 show the effects of insufficient drying. Excess DMEM solution in the tissue dominated the THz power spectra image of the tumor in **Figure 10B** [28] with high reflection that did not correlate to the pathology image shown in **Figure 10A** [28]. This led to a false positive result, suggesting a larger presence of cancer in the tumor. DMEM showed a similarly high refractive index and absorption coefficient to water, as seen in **Figure 10C** [19] and **10D** [19], so it is highly recommended to dry the tumor properly before imaging.

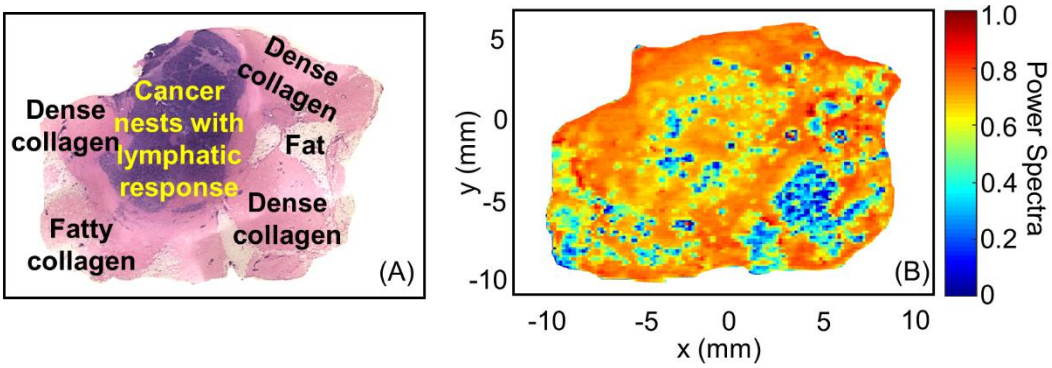

Figure 11: The artifacts in the THz image caused by the presence of air bubbles between the polystyrene plate and tumor. (**A**) Low power pathology image of tumor #ND11713. (**B**) THz power spectra image of tumor #ND11713 over the frequency range from 0.5–1.0 THz.

Another example of insufficient adherence to the protocol is shown for tumor #ND11713 in **Figure 11**. In this case, the air bubbles between the polystyrene plate and the tumor were not removed when the tumor was placed on the plate for the imaging procedure. This resulted in several spots of low reflection across the THz image in **Figure 11B**, which prevented accurate comparison to the pathology in **Figure 11A**. Thus, if any air bubbles are observed after placing the tumor on the plate, press it with the tweezers or lift the tumor and gently roll it onto the polystyrene until ai r gaps are removed.

Transmission spectroscopy results [18] for the same sample (# ND14139) are presented in **Figure 12**. Tumor sections were taken from points ① and ② in **Figure 12A** and characterized following the protocol. Both selected points were taken from the cancer tissue region in the tumor according to the pathology image in **Figure 12B**. The extracted absorption coefficient and refractive index for both tumor sections are presented in **Figure 12C**, **D**. Both points showed good agreement for the whole frequency range. The black curve from 0.15–2 THz in **Figure 12C** and **Figure 12D** represents data obtained from the literature [23] to compare the results obtained in our work.

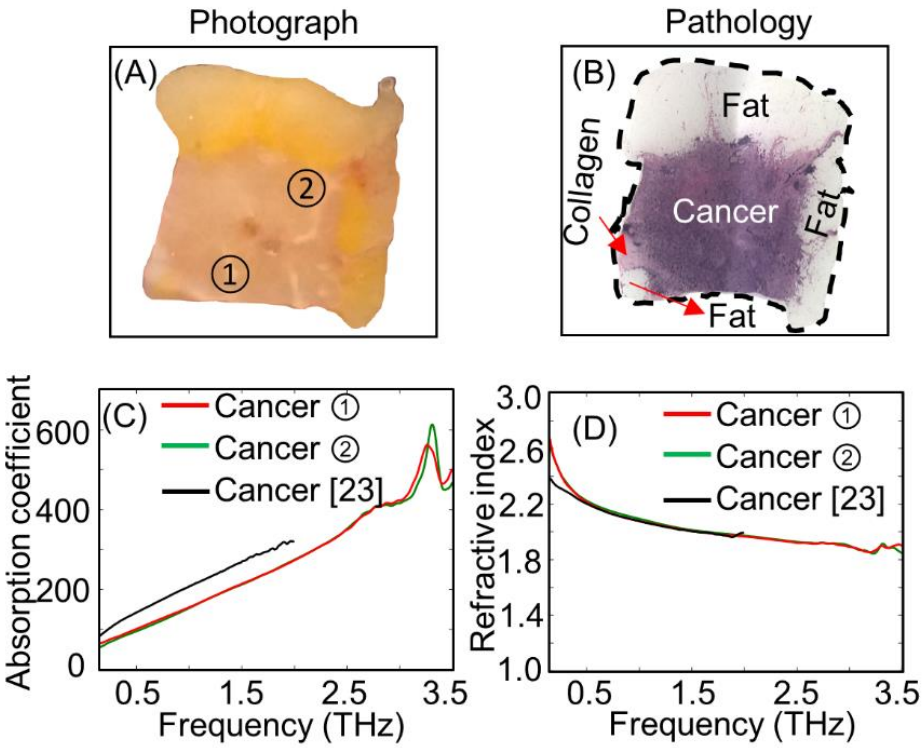

Figure 12: The characterization of breast cancer tumor #ND14139 using THz transmission spectroscopy. (**A**) The photograph of the tumor with two selected points marked and from where the 0.5 mm thick sections of the tumor were cut for the transmission spectroscopy measurements. (**B**) Low power pathology image of the tumor. (**C**) The transmission absorption coefficient (cm –1) plot ranging from 0.15–3.5 THz at points and . (**D**) The transmission refractive index plot ranging from 0.15–3.5 THz at points and . Figure republished from T. Bowman et al. [18] with permission from SPIE.

Discussion

Effective THz reflection imaging of fresh tissue is primarily dependent on two critical aspects: 1) the proper consideration of tissue handling (sections 2.2 and 2.2.4.15); and 2) the stage setup (primarily section 2.2.4.11). Insufficient drying of the tissue can result in increased reflection and inability to visualize regions due to high reflections of DMEM and other fluids. Meanwhile, poor tissue contact with the imaging window creates rings or spots of low reflection in the THz reflection image that obscure the results. Extra effort should be taken to ensure good tissue contact with the imaging window, including repositioning the tissue to obtain a better interface. For tissue

characterization, additional considerations for the stage setup must be carefully implemented. Improper balancing of the stage by even a few microns can cause significant shifts in the calculated refractive index and absorption coefficient of the tissue. This can also be a result of applying too much pressure to the tissue when mounting it on the imaging window, which can cause bowing of the polystyrene plate. For accurate calculations, the reference signal selected for characterization must also be obtained from the same phase plane of the image to avoid artificial phase shift.

The primary area where the protocol can be modified is in the dielectric materials used to mount the tissue, such as quartz (sections 3.6–3.7) and polystyrene (starting in section 4.5). As long as the selected window materials are uniformly thick and of low enough absorption to have good signal interaction with the tumor, other materials can be substituted. Materials should be evaluated ahead of time to determine whether they provide an adequate phase plane. Alternatively, for systems where the imaging window will be fixed, a nonuniform window thickness can be addressed by characterizing the phase shift calculated from an empty window scan. There is also some room for modification in how the tissue is mounted for shipment to the pathologist. While tissue marking dyes are used here out of convention, the important aspect is to have a method in place that enables comparison between the THz imaging and the pathology. The primary troubleshooting concerns for the protocol will involve obtaining a good THz signal and establishing proper windowing, which will depend on the specific system being used.

A primary limitation of any fresh tissue handling technique is the time that the tissue is exposed to air. This protocol was designed such that the tissue could remain exposed for no more than 1 hour to avoid decomposition prior to the pathology assessment. This is also reflected in the selection of the step size of the image. The THz system in this protocol can reach any step size from 50–500 μm in 50 μm increments, though the maximum spatial resolution of the system is

around 80 µm due to the spectral content of the THz signal. The 200 µm step in the protocol provided sufficient detail while maintaining a reasonable scan time of ~30 min. Assessment of the tumor samples by our consulting pathologist determined that this amount of air exposure does not cause damage to the tissue in an observable way at the cellular level. However, materials such as gelatin can be used to provide clear THz imaging without excessive drying, and may be investigated for future updates to the protocol [29] . For efficient use of time, steps like purging the system with dry nitrogen and setting up the imaging or spectroscopy can be performed before the tissue is removed from the DMEM. This is also important for future intraoperative applications where the time taken for imaging is a key factor in implementing the THz imaging into the surgical workflow.

Using this protocol intraoperatively represents a potential significant decrease in the time to assess the surgical margins of the tumor from several days or weeks to few a minutes. This will be accomplished when the hardware of the THz system is improved to use THz cameras instead of stepper motor scanners in the future. At present the most similar method employed intraoperatively is specimen radiography, which takes transmission X-ray images of excised tumors for interpretation by a radiologist to determine whether there is cancer on the tissue surface. The described imaging protocol provides a means of direct imaging of the tissue surface. The protocol for the freshly excised breast cancer tumors can also be used for the characterization and imaging of any other type of freshly excised solid tumor [8-11]. While this manuscript focuses on imaging freshly excised breast tumors following the described protocol, THz imaging of the associated formalin-fixed paraffin embedded tissue blocks has also been successfully validated with pathology [14-17, 19]. Imaging protocols similar to the one proposed here could be developed for pathology support in analyzing embedded tissues as well.

Disclosures

The authors declare that they have no conflict of interest.

Acknowledgments

This work was funded by the National Institutes of Health (NIH) Award # R15CA208798 and in part by the National Science Foundation (NSF) Award # 1408007. Funding for the pulsed THz system was obtained through NSF/MRI Award # 1228958. We acknowledge the use of tissues procured by the National Disease Research Interchange (NDRI) with support from the NIH grant U42OD11158. We also acknowledge the collaboration with Oklahoma Animal Disease Diagnostic Laboratory at the Oklahoma State University for conducting the histopathology procedure on all the tissues handled in this work.

References

1. Burford, N. M. & El-Shenawee, M. O. Review of terahertz photoconductive antenna technology. *Optical Engineering* 56 (1), 010901 (2017).

2. Sun Q, He Y, Liu K, Fan S, Parrott EPJ, Pickwell-MacPherson E. Recent advances in terahertz technology for biomedical applications. *Quant Imaging Med Surg*. 7(3), 345-355 (2017).

3. Wilmink, G. J., Rivest, B. D., *et al.* In vitro investigation of the biological effects associated with human dermal fibroblasts exposed to 2.52 THz radiation. *Lasers in Surgery and Medicine* 43 (2), 152–163 (2011).

4. Arbab, M. H., Winebrenner, D. P., Dickey, T. C., Chen, A., Klein, M. B. & Mourad, P. D. Terahertz spectroscopy for the assessment of burn injuries in vivo. *Journal of Biomedical Optics* 18 (7), 077004 (2013).

5. Sy, S., Huang, S., *et al.* Terahertz spectroscopy of liver cirrhosis: investigating the origin of contrast. *Physics in Medicine and Biology* 55 (24), 7587–7596 (2010).

6. Yu, C., Fan, S., Sun, Y. & Pickwell-Macpherson, E. The potential of terahertz imaging for cancer diagnosis: A review of investigations to date. *Quantitative Imaging in Medicine and Surgery* 2 (1), 33–45 (2012).

7. El-Shenawee, M., Vohra, N., Bowman, T. & Bailey, K. Cancer detection in excised breast tumors using terahertz imaging and spectroscopy. *Biomedical Spectroscopy and Imaging* 8, (1–2), 1–9 (2019).

8. Yamaguchi, S., Fukushi, Y., Kubota, O., Itsuji, T., Ouchi, T. & Yamamoto, S. Brain tumor imaging of rat fresh tissue using terahertz spectroscopy. *Scientific Reports* 6 (30124), 1–6 (2016).

9. Rong, L., Latychevskaia, T., *et al.* Terahertz in-line digital holography of human hepatocellular carcinoma tissue. *Scientific reports* 5 (8445), 1–6 (2015).

10. Park, J. Y., Choi, H. J., Nam, G., Cho, K. & Son, J. In Vivo Dual-Modality Terahertz / Magnetic Resonance Imaging Using Superparamagnetic Iron Oxide Nanoparticles as a Dual Contrast Agent. *IEEE Transactions on Terahertz Science and Technology* 2 (1), 93–98 (2012).

11. Ji, Y. Bin, Park, C. H., *et al.* Feasibility of terahertz reflectometry for discrimination of human early gastric cancers. *Biomedical Optics Express* 6 (4), 1413–1421 (2015).

12. Bowman, T., Walter, A., Shenderova, O., Nunn, N., McGuire, G., & El-Shenawee, M. A Phantom Study of Terahertz Spectroscopy and Imaging of Micro- and Nano-diamonds and Nano-onions as Contrast Agents for Breast Cancer," *Biomedical Physics and Engineering Express* 3 (5), 055001 (2017).

13. Chavez, T., Bowman, T., Wu, J., Bailey, K. & El-Shenawee, M. Assessment of Terahertz Imaging for Excised Breast Cancer Tumors with Image Morphing. *Journal of Infrared, Millimeter, and Terahertz Waves* 39 (12), 1283-1302 (2018).

14. Bowman, T. C., El-Shenawee, M. & Campbell, L. K. Terahertz Imaging of Excised Breast Tumor Tissue on Paraffin Sections. *IEEE Transactions on Antennas and Propagation* 63 (5), 2088–2097 (2015).

15. Bowman, T., El-Shenawee, M. & Campbell, L. K. Terahertz transmission vs reflection imaging and model-based characterization for excised breast carcinomas. *Biomedical Optics Express* 7 (9), 3756-3783 (2016).

16. Bowman, T., Wu, Y., Gauch, J., Campbell, L. K. & El-Shenawee, M. Terahertz Imaging of Three-Dimensional Dehydrated Breast Cancer Tumors. *Journal of Infrared, Millimeter, and Terahertz Waves* 38 (6), 766-786 (2017).

17. Bowman, T., Chavez, T., *et al.* Pulsed terahertz imaging of breast cancer in freshly excised murine tumors. *Journal of Biomedical Optics* 23 (2), 026004 (2018).

18. Bowman, T., Vohra, N., Bailey, K. & El-Shenawee, M. Terahertz tomographic imaging of freshly excised human breast tissues. *Journal of Medical Imaging* 6 (2), 023501 (2019).

19. Vohra, N., Bowman, T., Diaz, P. M., Rajaram, N., Bailey, K. & El-Shenawee, M. Pulsed Terahertz Reflection Imaging of Tumors in a Spontaneous Model of Breast Cancer. *Biomedical Physics and Engineering Express* 4 (6), 065025 (2018).

20. Jacobs, L. Positive margins: the challenge continues for breast surgeons. *Annals of Surgical Oncology* 15 (5), 1271–1272 (2008).

21. Moran, M. S., Schnitt, S. J., *et al.* Society of Surgical Oncology--American Society for Radiation Oncology Consensus Guideline on Margins for Breast-Conserving Surgery With Whole-Breast Irradiation in Stages I and II Invasive Breast Cancer. *International Journal of Radiation Oncology* 88 (3), 553–564 (2014).

22. Fitzgerald, A. J., Wallace, V. P., Jimenez-Linan, M., Bobrow, L., Pye, R. J. & Purushotham, A. D. Terahertz Pulsed Imaging of human breast tumors. *Radiology* 239 (2), 533–540 (2006).

23. Ashworth, P. C., Pickwell-MacPherson, E., *et al.* Terahertz pulsed spectroscopy of freshly excised human breast cancer. *Optics Express* 17 (15), 12444–12454 (2009).

24. Doradla, P., Alavi, K., Joseph, C. & Giles, R. Detection of colon cancer by continuous-wave terahertz polarization imaging technique. *Journal of Biomedical Optics* 18 (9), 090504 (2013).

25. Reid, C. B., Fitzgerald, A., *et al.* Terahertz pulsed imaging of freshly excised human colonic tissues. *Physics in Medicine and Biology* 56 (1), 4333–4353 (2011).

26. Teraview. https://teraview.com/ (2019).

27. Orosco, R. K., Tapia, V. J., *et al.* Positive Surgical Margins in the 10 Most Common Solid Cancers. *Scientific Reports* 8 (1), 1–9 (2018).

28. Bowman, T., Chavez, T., Khan, K., Chakraborty, A., Wu, J., Bailey, K. & El-Shenawee, M. Statistical signal processing for quantitative assessment of pulsed terahertz imaging of human breast tumors. *2017 42nd International Conference on Infrared, Millimeter, and Terahertz Waves (IRMMW-THz)*, Cancun, 1-2 (2017).

29. Gavdush, A. A., Chernomyrdin, N. V., Malakhov, K. M., Beshplav, S. T., Dolganova, I. N., Kosyrkova, A. V., Nikitin, P. V., Musina, G. R., Katyba, G. M., Reshetov, I. V., Cherkasova, O. P., Komandin, G. A., Karasik, V. E., Potapov, A. A., Tuchin, V. V., & Zaytsev, K. I. Terahertz spectroscopy of gelatin-embedded human brain gliomas of different grades: a road toward intraoperative THz diagnosis. *J. Biomed. Opt.* 24 (2), 027001 (2019).

CHAPTER 3

Pulsed Terahertz Reflection Imaging of Tumors in a Spontaneous Model of Breast Cancer

Abstract

We report the use of reflection-mode terahertz (THz) imaging in a transgenic mouse model of breast cancer. Unlike tumor xenografts that are grown from established cell lines, these tumors were spontaneously generated in the mammary fat pad of mice, and are a better representation of human breast cancer. THz imaging results from 7 tumors that recapitulate the compartmental complexity of breast cancer are presented here. Imaging was first performed on freshly excised tumors within an hour of excision and then repeated after fixation with formalin and paraffin. These THz images were then compared with histopathology to determine reflection-mode signals from specific regions within tumor. Our results demonstrate that the THz signal was consistently higher in cancerous tissue compared with fat, muscle, and fibrous tissue. Almost all tumors presented in this work demonstrated advanced stages where cancer infiltrated other tissues like fat and fibrous stroma. As the first known THz investigation in a transgenic model, these results hold promise for THz imaging at different stages of breast cancer.

1. Introduction

Breast cancer accounts for 30% of all new cancer diagnoses [1] and is the most frequently diagnosed cancer in women in the United States [2]. For early-stage breast cancer, the current standard of care is breast-conserving surgery (BCS) followed by chemotherapy. Unfortunately, a dire limitation to this procedure is the incomplete local excision of the tumor, resulting in positive margins at the time of final pathology [3]. This leads to approximately 20% of patients requiring

further surgery to attain clear margins [4]. In light of this, there is a critical need for an intra-operative imaging technology that can reliably evaluate the margins for possible presence of cancerous tissue. Such an evaluation requires the ability to accurately differentiate between normal and cancerous tissue as well as between different components of breast tissue – fat, muscle, and fibrous tissue.

Nearly 20 years ago, Hu *et al* employed terahertz (THz) imaging and demonstrated its capacity to differentiate between fat and muscle within porcine tissue [5]. Since then, THz technology has taken great strides, and noteworthy research has unveiled its significant potential for biomedical applications. Investigators have demonstrated the sensitivity of THz imaging in differentiating between different types of tissue present in both formalin-fixed, paraffin-embedded (FFPE) and fresh samples [6-13]. THz radiation is very sensitive to polar substances, such as water and hydration state. Therefore, THz waves can provide a better contrast for soft tissues than X-rays [14]. Physiologic changes associated with tumors generally lead to increased water content and decreased lipid concentration compared with normal tissue [15]. This suggested that water content and lipid concentration might lead to strong changes in the terahertz reflection. Nevertheless, a number of studies have imaged biologic samples that were fixed in formalin, dehydrated, and paraffin embedded for histopathologic examination and still found contrast between tumor and the surrounding normal tissue [7-13] suggesting that in addition to lipid changes, other factors such as increased cell density or the presence of certain proteins may also be responsible for contrast [16].

However, imaging of fresh human tissue from breast and other types of cancer outside of a surgical context is challenging. To circumvent this obstacle, many investigators have turned to mouse-model tumor xenografts to carry out their studies. Chen *et al* performed *in vivo* THz

imaging on a subcutaneous xenograft mouse model and successfully detected early breast cancer [17]. They were also able to differentiate between cancerous and fatty tissue within fresh *ex vivo*. Also, Bowman *et al* successfully performed THz imaging and statistical analysis of fixed and fresh xenograft breast tumors [18]. A reflection-type THz imaging system was used on an orthotopic glioma rat model to demonstrate that the THz reflection intensity was higher in brain tumors than in the surrounding normal tissue [19], [20].

Although these studies have provided a wealth of information, tumor xenograft models fall short in closely mimicking the stages of cancer progression and underlying mechanisms. A recent study from our group demonstrated the ability of THz imaging to clearly distinguish between cancerous and fatty tissue in breast tumor xenografts grown from murine breast cancer cells [18]. However, the xenograft models were devoid of fibrous tissue, and therefore could not adequately represent human tissue. Transgenic mouse models offer a promising alternative to the conventional xenograft models for imaging, biological, and therapeutic investigations. Whereas xenograft models based on human breast cancer cells require the impairment of the immune system, genetically engineered mice provide a competent immune system where the tumor can grow, and its development can be followed from early time points [21]. The MMTV-PyMT transgenic mouse model has been widely used to investigate breast cancer due to its metastatic potential and how closely it reflects the many changes and aspects of human breast cancer progression. In this model, the promoter/enhancer mouse mammary tumor virus long terminal repeat (MMTV LTR) drives the expression of the oncoprotein polyoma middle T antigen (PyMT), resulting in the development of multifocal adenocarcinomas within the mammary epithelium, and also in metastatic lesions within the lymph nodes and lungs [22].

Plodinec *et al* investigated the nanomechanical signatures of normal and benign samples from both human breast biopsies and MMTV-PyMT mammary tissue. In contrast to the human breast samples, they found that healthy mammary fat pad tissue from this transgenic mouse model exhibited extensive amounts of adipose tissue (70-80%). At the early cancer stage, they observed basement membrane degradation, and the absence of collagen I at the soft core of the tumor. They noted that collagen I was instead increasingly present towards the periphery of the tumor. Furthermore, they monitored the loss of integrin β1 expression in the MMTV-PyMT specimens at different tumor progressions stages, and found that the fibrous tissue was lost significantly early [23]. Similar findings were reported by Lin *et al*, wherein they noted the loss of β1-integrins was strongly associated with the MMTV-PyMT tumor progression [24]. They also observed that adipocytes formed the majority of the mouse mammary glands and they were located very close to the epithelial structures. This was very different from the human breast tissue, where extensive extracellular connective tissue stroma was present, resulting in the adipocytes being less proximal to the ductal epithelium. Almholt *et al* likewise observed that adipose tissue surrounded the epithelium in the MMTV-PyMT mouse gland in great amounts, whereas the human mammary epithelium was instead surrounded by a specialized fibroblastoid stroma not adjacent to the adipocytes [25].

In spite of these structural differences, the MMTV-PyMT breast cancer model has been proven to be a reliable model for metastatic breast cancer, sharing many more similarities than differences with human luminal breast cancer on a molecular and histological level [22,24,26]. While the MMTV-PyMT model possesses a high percentage of adipose tissue, it still results in a tumor microenvironment where some fibrous tissue is present. Moreover, this transgenic mouse model poses a level of complexity that more closely mimics that of human breast cancer tissue,

and therefore presents a better model for investigating the THz reflection signatures acquired from breast tissue components in the native microenvironment.

The objective of this study is to determine the THz reflection differentiation between cancer and noncancerous (fibrous, fat, and muscle) tissue in a spontaneous model of breast cancer. Specifically, we use the MMTV-PyMT mouse model of breast cancer to obtain spontaneously generated breast tumors for THz imaging. To the best of our knowledge, this is the first time THz imaging has been investigated for imaging freshly excised breast cancer tumors derived from a transgenic mouse model. In addition to providing new knowledge about THz reflection from fat, fibrous and muscle tissue in orthotopic breast tumors, these results also lay the groundwork for investigating THz imaging at different stages of breast cancer progression.

This work is organized as follows: methodology including terahertz imaging system and mice tumor sample preparation in Sec. 2; the experimental results of THz image correlation with pathology in Sec. 3; and discussion and concluding remarks in Sec. 4.

2. Methodology

2.1. Mice tumor sample preparation

Protocols for all mouse experiments were approved by the Institutional Animal Care & Use Committee (IACUC) of the University of Arkansas. Four MMTV-PyMT mice between 3-4 weeks of age were purchased from The Jackson Laboratories. Mice were maintained under standard 12-hour light/dark cycles with regular access to food and water. Tumors were excised at between 5 and 11 weeks.

Upon excision of the tumor, the tissue was immersed in phosphate buffered saline (PBS) or in Dulbecco`s Modified Eagle Medium (DMEM). DMEM is often utilized in biobanks when

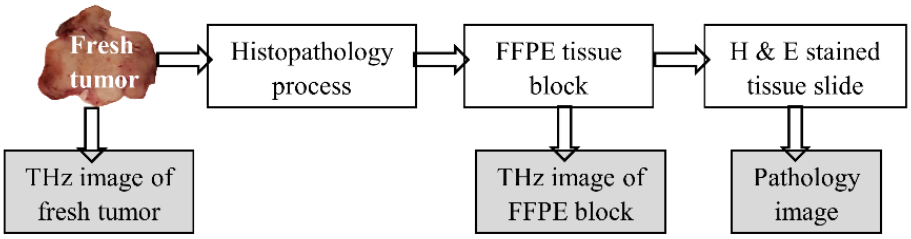

Fig. 1. Summary of imaging procedure of transgenic tumors.

handling human breast tissue and is investigated here to study potential changes in THz imaging from refrigeration and shipping of fresh tissue. Tissues in PBS were imaged an hour after excision, while tissues in DMEM were stored in a refrigerator and imaged within 24 hours, mimicking overnight shipping from a biobank. Upon conducting THz spectroscopy of DMEM and PBS, it was found that they have THz signature similar to water (see Appendix). Therefore, the choice of solution when immersing fresh tissue did not affect the imaging. After being removed from medium, the tissue was dried using filter paper and positioned between two polystyrene plates with slight pressure to make its surface as flat as possible. The tissue sample was then positioned on the THz imaging scanner window prepared for the reflection mode (see Fig. 2). After THz imaging, the tissue was immersed in formalin and shipped to the Oklahoma Animal Disease Diagnostic Laboratory (OADDL), where it was embedded in paraffin for histopathology. Formalin fixed paraffin embedded (FFPE) tissue slices of 3-4 μm thickness were stained with hematoxylin and eosin (H&E) to produce the pathology image. The thickness of the fresh tissues handled in this work is approximately 5 mm while that of the corresponding FFPE tissues is between 3-4 mm due to possible shrinkage incurred during formalin fixation and slicing during the histopathology procedure. Subsequent THz imaging was performed on the FFPE block. The tissues in blocks were mounted on standard plastic pathology cassettes which prevented transmission imaging without destructive sectioning of the samples, so reflection imaging is observed here. The procedure is

described in the diagram of Fig. 1. THz imaging of both fresh and FFPE tissue will be presented in Section 3 in order to compare the image contrast based on the water content in the tissue.

2.2. Experimental Terahertz Imaging System

Terahertz imaging in this work is performed using a commercial THz system from TeraView, Ltd shown in the diagram in Fig. 2a. An 800 nm pulse from a Ti:Sapphire laser is passed through a beam splitter. One path of the laser is used to excite a biased THz emitter consisting of a gold bowtie antenna on a GaAs substrate, which emits a resulting time domain pulse in the THz range seen in Fig. 2b. The Fourier transform of the pulse is shown in Fig. 2c, demonstrating the spectral power of the pulse from 0.1 to 4 THz. The incident pulse is directed using mirrors to reflect off the sample under test, then a second set of mirrors directs the reflected signal to a THz receiver with the same construction as the emitter. The second path of the laser excites the receiver after passing through an optical delay line such that the incident THz field generates a current on the receiver measured by the computer. The sample stage moves in set increments using stepper motors to obtain the reflected signal at each point. For all results presented in this work the step size of the motor was 200µm while the spot size of the beam on the tissue surface at each point was function of frequency, e.g. at 1 THz the radius of the beam spot size is ~0.7271mm and at 2 THz it is ~0.3554mm.

Following the acquisition of the THz signal at each point, the THz image is produced by one of two methods. For fresh tissue samples mounted between polystyrene plates (see Fig. 2a), a power spectrum integration of the reflected frequency domain signal is taken at each point using the equation:

$$spectral\,power = \int_{f_1}^{f_2} |E_{samp}(f_{THz})|^2 / |E_{ref}(f_{THz})|^2 \, df_{THz} \quad , \qquad (1)$$

where E_{samp} is the measured sample signal, E_{ref} is the reference reflection signal from the air-polystyrene interface, and f_1 and f_2 are the selected frequencies over which to perform the integration. This kind of power integration has been suggested as a principal signal component to provide distinction between tissue regions [27]. The authors previously found this calculation to provide consistently good images for freshly excised xenograft mice tumors for an integration range from 0.5 to 1.0 THz, so the same frequency range will be used here [18]. For imaging the FFPE tissue, the top of the tissue block is positioned directly on the scanning window of the system. In this case, the THz images are obtained by taking the peak value of the reflected time domain electric field signal normalized against the peak signal measured from a gold mirror reference.

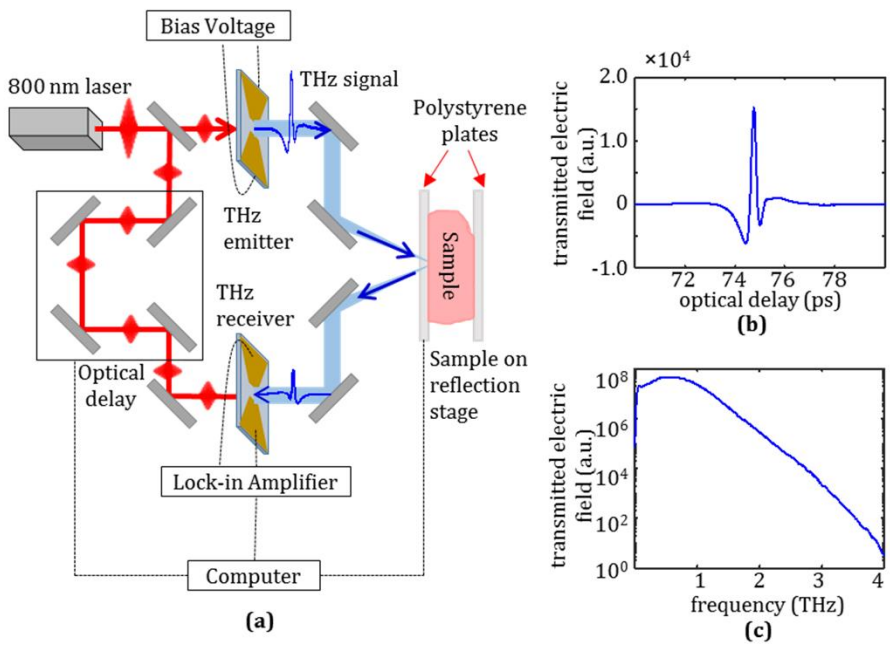

Fig. 2. (a) Terahertz imaging system diagram for the reflection mode of fresh tumors, (b) Incident time domain THz pulse, and (c) frequency domain signal following Fourier transform.

3. Experimental Results

In this work, 15 breast tumors were excised from 4 transgenic mice and imaged using the THz imaging system. As predicted from literature [22], the transgenic mice tumors share complex

structures in their tissues with multiple regions of cancer, cancer infiltrated fat, fat, cystic areas, fibro, and others as will be discussed in this Section. This contrasts with previously studied tumor xenografts, which consisted mostly of cancer and fat [18]. Seven tumors are selected here, as described in Table 1, to present the THz reflection imaging results for both freshly excised tumor tissue and FFPE tissue block for each tumor. The tumors are numbered from 1-7 with an additional code referring to the sequence of excision. In all results presented here, we observed that the histopathology process altered the tumor tissue shape and size, causing the THz images of fresh tissue and the pathology images to be different. The 15 tumor tissues were scanned over a full year from June 2017 to July 2018 and showed consistent contrast in all images as will be seen below.

Table. 1: Summary of presented tumors

Sample no.	Tumor 1 (14-A)	Tumor 2 (15-A)	Tumor 3 (15-D)	Tumor 4 (15-E)	Tumor 5 (15-B)	Tumor 6 (14-C)	Tumor 7 (12-A)
Photo of fresh tissue	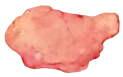	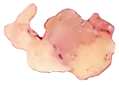	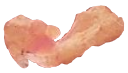	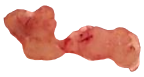			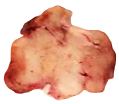
Size (mm)	~14×9×5	~19×12×5	~21×8×5	~25×8×5	~16×11×5	~18×14×5	~20×17×5
Solution	PBS	PBS	DMEM	DMEM	PBS	DMEM	PBS

3.1. Tumor 1

The results of Fig. 3 represent THz imaging of Tumor 1 (14-A). Fig. 3a shows the THz image of the freshly excised tumor represented in the frequency domain spectral power between 0.5 and 1.0 THz. Adding frequencies above 1THz to the spectral power did not improve the results.

Fig. 3b shows the normalized THz time-domain peak from the FFPE tissue block. The low power pathology image of tissue sliced at 3-4 μm from the top surface of the FFPE block is shown in Fig. 3c. The pixels in the pathology image marked as ①-⑦ are selected from different tissue types based on the pathology report. The high power images of the surrounding regions of these pixels are shown in the figure. The time domain signals (from FFPE THz imaging data) at different tissue types marked as ①-⑦ are plotted in Fig. 3d showing the difference in THz signal magnitude of each type. The spectra of the reflected electric field signals of Fig. 3d are demonstrated in Fig. 3e. All THz reflected signals are normalized with respect to the reflected signal from the gold mirror. The baseline noise of the system is usually around ± 0.01 to ± 0.035 for the raw measured electric field without normalization. For the reference peaks taken across the scans in this work, this correlates to a noise level of about ± 0.0005 to ± 0.00175 in the normalized scan values, which is insignificant compared to the normalized measured data from the tissue.

The results of Fig. 3d demonstrate that the magnitude of the reflected THz signal from the cancer region is more than that of any other region in the tissue. This can be seen in the THz images of both fresh and FFPE tissue in Figs. 3a-b, where the cancer region (represented in red color in the image color bar) dominates the tumor. The THz image of the FFPE tissue is particularly effective in differentiating between the cancer and other regions. For example, the cancer with glandular secretions can be seen as yellowish-red region and the cancer infiltrated in fat can be seen as yellow-greenish region in Fig. 3b. The dark blue region in this image represents the cystic region in the cancer. Although fibrous, muscle, and brown fat regions show almost similar reflection in the THz image, they are well differentiated from cancer. For the THz image of fresh tissue in Fig. 3a, the cancerous and non-cancerous regions are well differentiated. The dark blue boundary in the image of fresh tumor represents an edge effect due to the difference in surface level of the

tissue with respect to the polystyrene slide, which is not the case with the FFPE tissue. Considering the complexity of the transgenic mouse tumor shown in Fig. 3, a good agreement between the THz and pathology images is demonstrated, with slightly better results for the FFPE tissue than that of fresh tissue. It should be noted that THz imaging of all fresh tissues was conducted blindly with respect to the pathology, where the histopathological imaging was processed afterward.

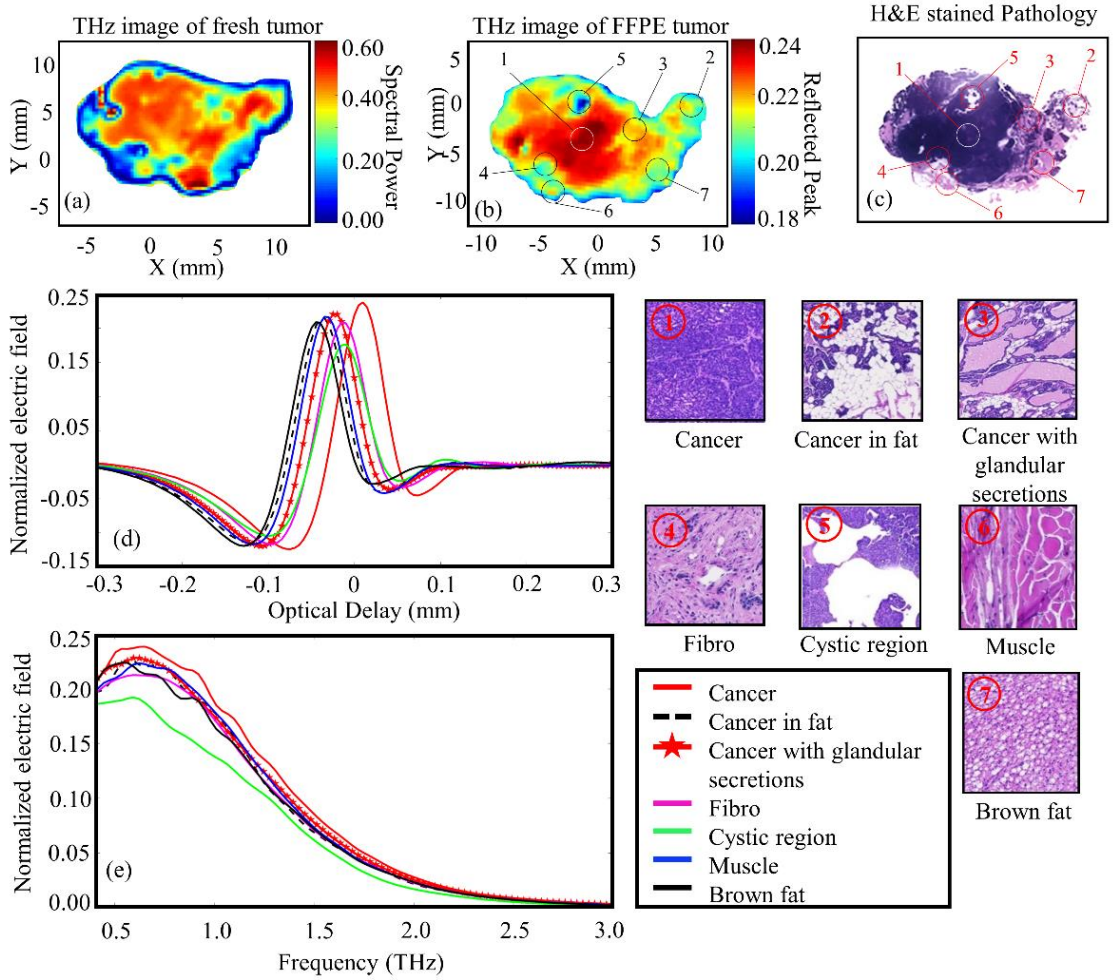

Fig. 3. THz reflection images of transgenic mice breast tumor 1(14-A), (a) Frequency domain THz image of freshly excised tumor represented by spectral power, (b) Time domain THz image of FFPE tumor tissue block represented by peak value, (c) Low power pathology image (d) Time domain signals of normalized reflected electric field at selected pixels ①-⑦, (e) Spectrum of normalized reflected electric field of the signals shown in (d). The high power pathology images of surrounding regions of ①-⑦ are shown. All THz signals are normalized with respect to a reference signal reflected from a gold mirror.

3.2. Tumor 2

The results of Fig. 4 represent THz imaging of Tumor 2 (15-A). From Fig. 4c it can be seen that most of tumor 2 is cancer (the red color in Figs. 4a and 4b image color bars). Meanwhile, other regions show intensity differentiation in the THz image in Fig. 4b. For example, muscle ⑥ shows a yellowish-red color, cancer in fat ② appears cyan, the cystic area in the cancer ⑤ is yellow, the glandular secretions ④ show a greenish-blue color, and brown fat ⑦ shows a light blue color. It should be noted here that the differentiation in THz images for fresh (Fig. 4a) and tissue block (Fig. 4b) is primarily due to the difference in the imaging surfaces which results in different features in the image. For example, the cancer in fat region in Fig. 4c ② shows dark blue color in Fig. 4a which demonstrates the presence of more fat in that region. After the histopathology slicing of the block, another tissue layer of cancer infiltrated in the fat becomes visible in Fig. 4b (② in Fig. 4c). There are additional regions of low reflection across the center of the tissue in Fig. 4a which are due to air bubbles that arise while mounting the fresh tissue on the polystyrene plate for scanning rather than from fat. One differentiation that THz imaging could not demonstrate in this tumor is between cancer and salivary glands, indicated by ① and ③ in Fig. 4c. These two regions do not show any color difference in the THz images in both Figs. 4a and Fig.4b. The presence of salivary gland in this tumor is due to the natural tendency of transgenic mice tumors to grow around the neck of the mouse, and salivary gland would not exist in human breast tumors. In conclusion, we can see that the THz image in Fig. 4b is a better representation of the pathology image of Fig. 4c compared with the fresh tumor image in Fig. 4a.

3.3. Tumor 3

The results of Fig. 5 represent THz imaging of Tumor 3 (15-D). Tumor 3 is consistent with the previous samples in proving the capability of THz imaging in differentiating tissue types.

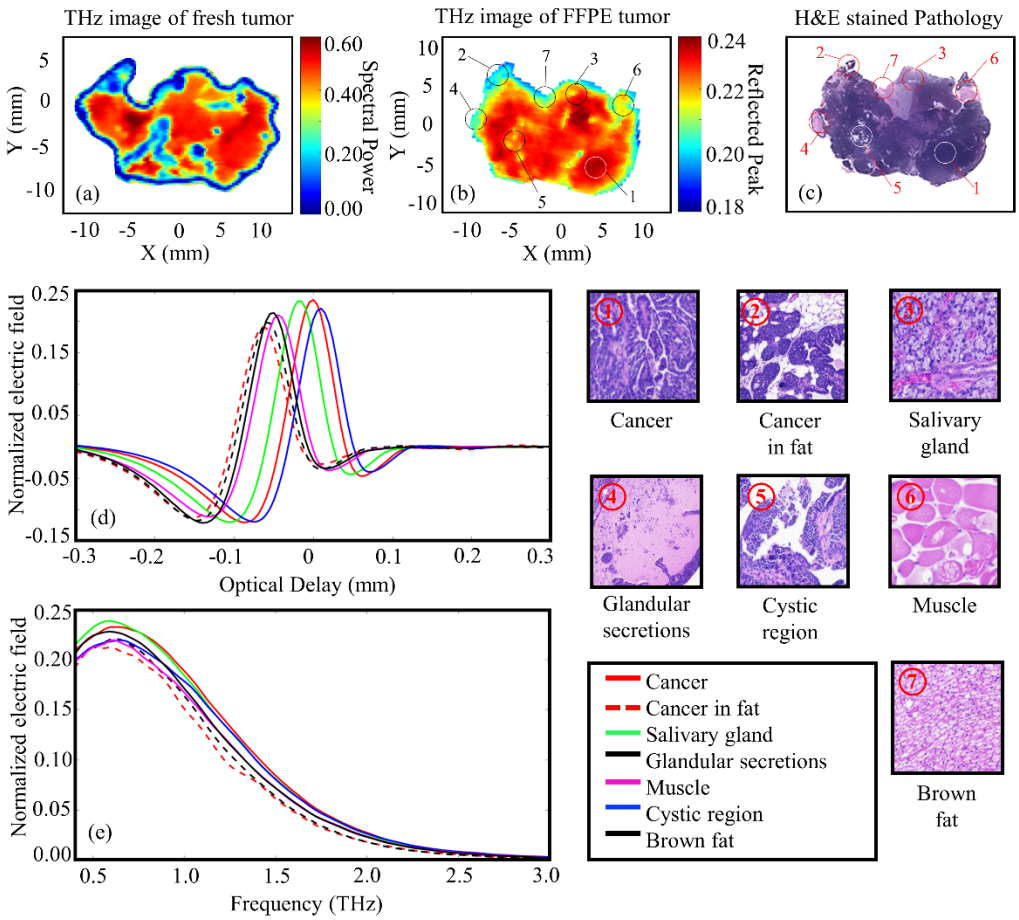

Fig. 4. THz reflection images of transgenic mice breast tumor 2 (15-A), (a) Frequency domain THz image of freshly excised tumor represented by spectral power, (b) Time domain THz image of FFPE tissue block represented by peak value, (c) Low power pathology image (d) Time domain signals of normalized reflected electric field at selected pixels ①-⑦, (e) Spectrum of normalized reflected electric field of the signals shown in (d). The high power pathology images of surrounding regions of ①-⑦ are shown. All THz signals are normalized with respect to a reference signal reflected from a gold mirror.

The red color in the THz images in Fig. 5a and 5b denotes the cancer region. The yellowish-blue region in both Fig. 5a and 5b indicates cancer infiltrated in fat ②. The dark blue region in Fig. 5a signifies the presence of fat tissue which is totally infiltrated with cancer in the FFPE tissue (Fig. 5b) upon conducting the histopathology process on the fresh tissue. The high reflections observed diagonally along the center of the image in Fig. 5a is most likely due to excess fluid beneath the tissue while it was freshly excised. The higher reflection from this fluid was spread over the areas

that would normally be muscle ③ in Fig. 5b. There is also a possibility that the surface of the tissue has changed significantly from where the THz fresh image was taken (Fig. 5a) to where the pathology image was taken (Fig. 5c), resulting in different features in these images. From Figs. 5d and 5e, we can see that the signal for the fibro-fatty ⑤ and brown fat ④ regions show almost equal amplitudes, which can also be seen in the THz image in Fig. 5b. Likewise, the signal amplitudes of muscle ③ and the cancer in fat ② regions are similar, leading to displaying similar

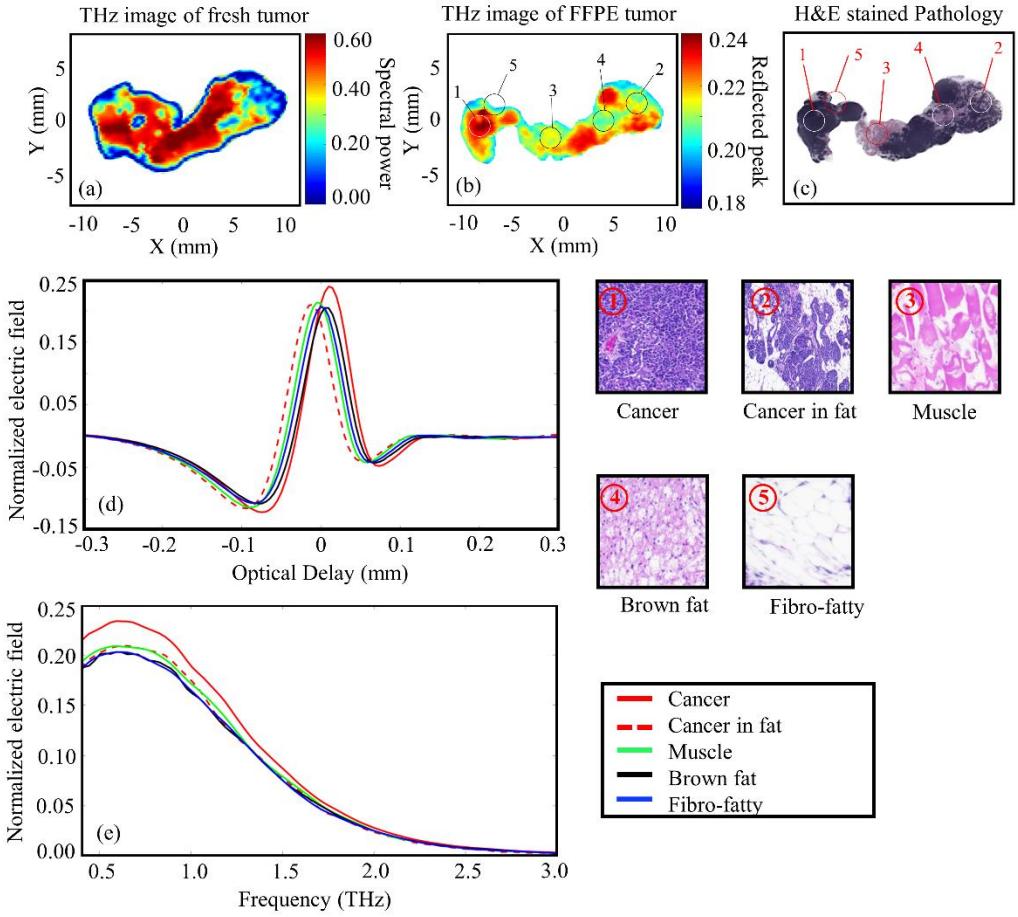

Fig. 5. THz reflection images of transgenic mice breast tumor 3 (15-D), (a) Frequency domain THz image of freshly excised tumor represented by spectral power, (b) Time domain THz image of FFPE tumor tissue block represented by peak value, (c) Low power pathology image (d) Time domain signals of normalized reflected electric field at selected pixels ①-⑤, (e) Spectrum of normalized reflected electric field of the signals shown in (d). The high power pathology images of surrounding regions of ①-⑤ are shown. All THz signals are normalized with respect to a reference signal reflected from a gold mirror.

color intensities in THz image of Fig. 5b. However, despite their similarities to each other, all these regions show significant differentiation from the cancer region ①.

3.4. Tumor 4

The results of Fig. 6 represent THz imaging of Tumor 4 (15-E). The results demonstrate a more advanced cancer stage which has undergone necrosis (designated based on the pathology report) that is seen in the form of several cracks (lumens) in the interior of the solid cancer region

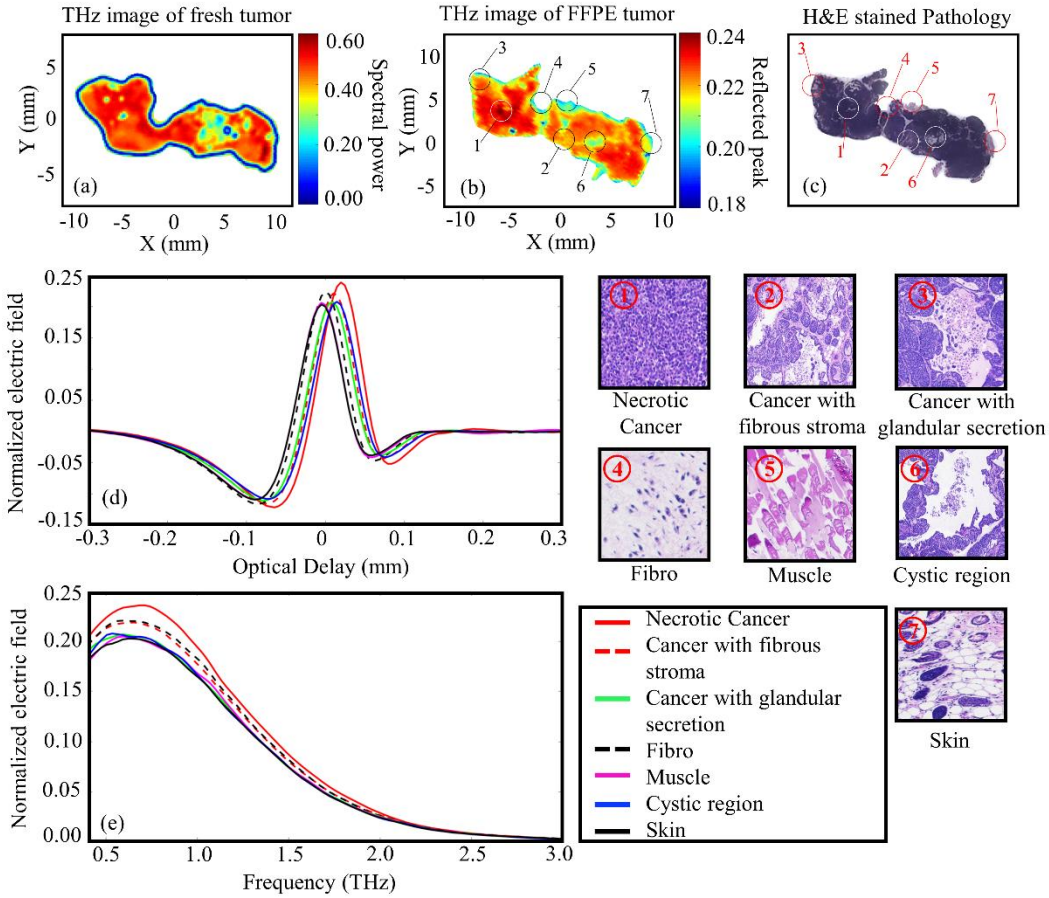

Fig. 6. THz reflection images of transgenic mice breast tumor 4 (15-E), (a) Frequency domain THz image of freshly excised tumor represented by spectral power, (b) Time domain THz image of FFPE tissue block represented by peak value, (c) Low power pathology image (d) Time domain signals of normalized reflected electric field at selected pixels ①-⑦, (e) Spectrum of normalized reflected electric field of the signals shown in (d). The high power pathology images of surrounding regions of ①-⑦ are shown. All THz signals are normalized with respect to a reference signal reflected from a gold mirror.

in the pathology image Fig. 6c. These cracks are displayed as cystic gaps ⑥. These cystic gaps show significant contrast (green color) in the THz image in Fig. 6b. At this stage, cancer starts producing glandular structures ③ filled with some secretions which can be seen as yellowish-red color in Fig. 6b. The regions of cancer with fibrous stroma ② and dense fibrous ④ regions in the tissue show almost similar signal amplitudes in Fig. 6d. This can primarily be due to the cell densities of the two regions. One unique feature compared to the previous samples is that the THz image in Fig. 6b shows the presence of skin ⑦ in the tumor tissue as reported in Fig. 6c. The skin could not be clearly seen in the THz image of fresh tissue in Fig. 6a but folded down during the histopathology process. The yellow-greenish and blue color regions in Fig. 6a are due to air bubbles that occurred during settling the tissue on the polystyrene plate. The fresh tissue image shows a high reflection over the entire tissue which is primarily due to the fact that most of the tumor is cancerous. This could also be due to fluid pooled beneath the tissue due to secretions from the necrotic cancer during the pressure made on the tissue when positioned between two polystyrene plates.

3.5. Tumor 5

The results of Tumor 5 (15-B) are presented in Fig. 7. Like previous results, the red color in the THz images represents the highest reflected amplitude which belongs to the cancer tissue ①. The regions of high reflections in the Fig. 7a is primarily due to blood and PBS on the surface of tissue that was not properly absorbed using filter paper. In some cases, the excised tumors continue to release fluids even after drying, causing the reflection to be stronger than other noncancerous regions in the tumor. This is a remaining challenge in imaging freshly excised tumors. The THz image of the fresh tissue shows clear differentiation between cancer and fat (② as seen in pathology image) where fat is the blue color in the lower right part of Fig. 7a. This

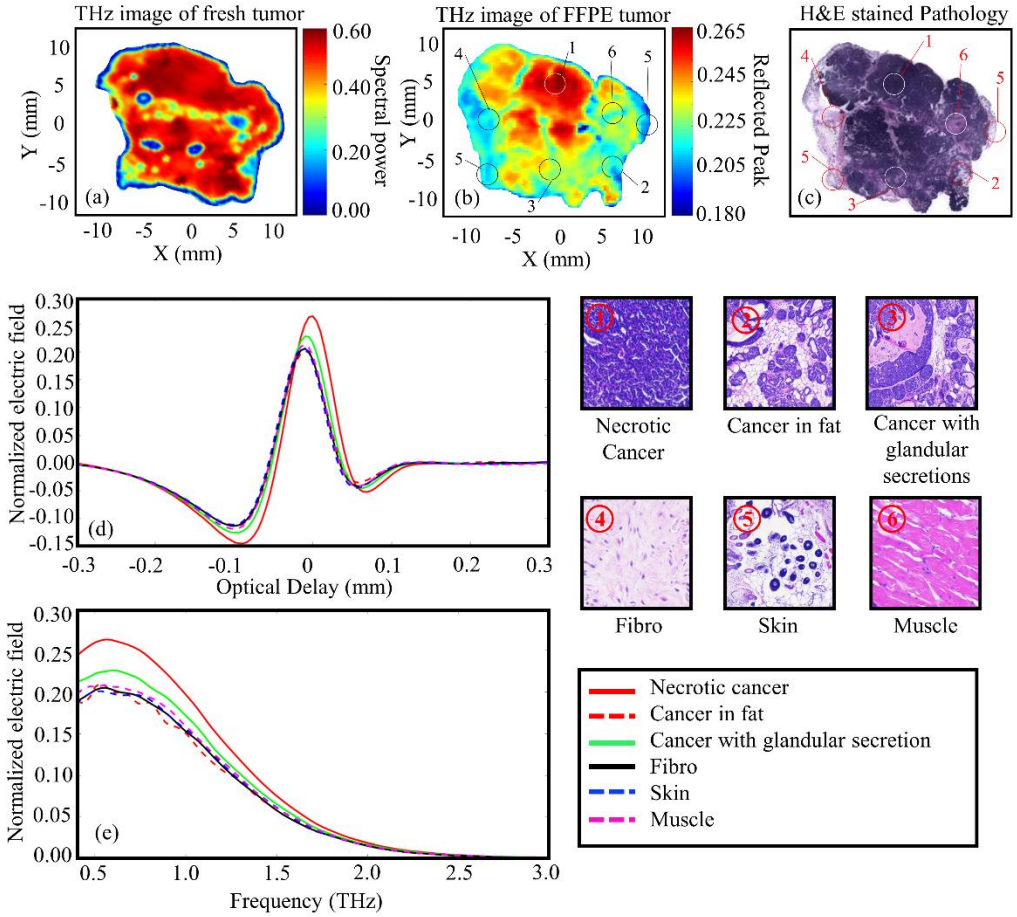

Fig. 7. THz reflection images of transgenic mice breast tumor 5 (15-B), (a) Frequency domain THz image of freshly excised tumor represented by spectral power, (b) Time domain THz image of FFPE tissue block represented by peak value, (c) Low power pathology image (d) Time domain signals of normalized reflected electric field at selected pixels ①-⑥, (e) Spectrum of normalized reflected electric field of the signals shown in (d). The high power pathology images of surrounding regions of ①-⑥ are shown. All THz signals are normalized with respect to a reference signal reflected from a gold mirror.

differentiation was often observed in tumor xenografts grown in mice [18]. The dark blue spots throughout the center of Fig. 7a are due to the air bubbles that could be observed when zooming in on the photograph in Table 1. The yellow-blush region in the lower left corner of Fig. 7a is a large area of skin ⑤. The yellow color slightly above the center of the tissue is most likely some surface roughness and separation of the tissue from the polystyrene, but may also be some loose fatty tissue that was removed in the histopathology process. The highest reflection (dark red color)

in Fig. 7b is primarily because of the higher density of cancer cells in that region ①. Almost all the regions indicated in Fig. 7c shows clear intensity differentiation in Fig. 7b, except the fibro ④ and the skin ⑤ that show similar cyan color. This similarity can also be seen in the signal amplitudes in Fig. 7d and 7e (solid black and dashed blue lines). It should be noted that the skin present in Fig. 7c and 7b cannot be seen in fresh tissue imaging in Fig. 7a as it was on the upper surface and was folded over with the imaging surface during the histopathology process. Additionally, the cystic areas represented by the light lumens (cracks) within the dark purple region seen in Fig. 7c are primarily revealed during slicing the FFPE block in the histology process. This is attributed in the pathology report to the aggressiveness of the cancer in this sample.

3.6. Tumor 6

The results in Fig. 8 represents THz imaging of Tumor 6 (14-C). The THz image of fresh tissue in Fig. 8a is dominated with the high intensity reflection of cancerous and muscle tissues which is also clear in Fig. 8c. The dark blue region at the top of Fig. 8a is the mostly fat ③ as can be seen in the THz image of FFPE in Fig. 8b and the pathology in Fig. 8c. The high reflection (red color) on the left side of the tissue in Fig. 8a is most likely excess fluid that was not fully removed by the filter paper and seeped from the muscle tissue during imaging. Additional blood or protein secretions from within the necrotic cancer region might also have emerged when the tissue was pressed between the two polystyrene plates. Furthermore, the regions of cancer infiltrated in fat ② in Fig. 8c result in the dark and light blue color areas on the right side in Fig. 8a demonstrating the significant contrast provided by THz imaging even in the mingled cancer and fat regions of freshly excised tumor. Similar to all other FFPE tissues discussed above in this section, Fig. 8b is a reasonable representation of the pathology image in Fig. 8c where cancer ① can be seen with a

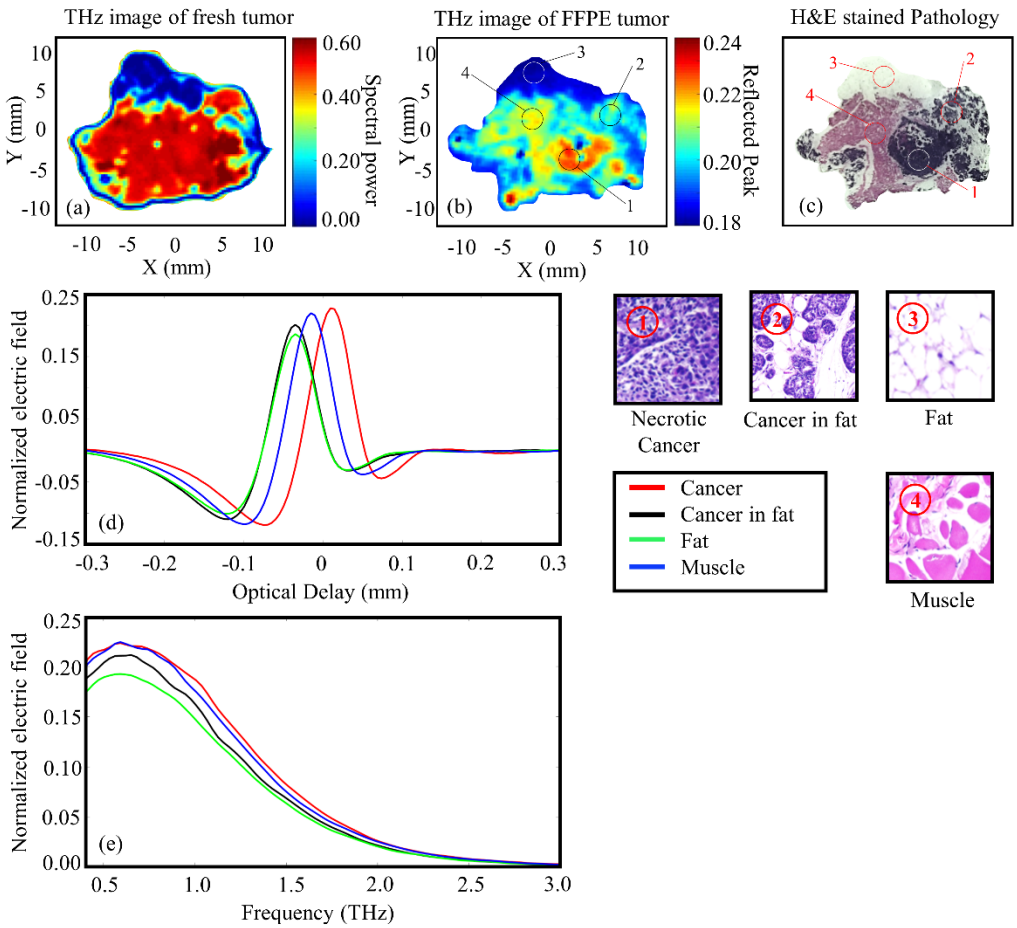

Fig. 8. THz reflection images of transgenic mice breast tumor 6 (14-C), (a) Frequency domain THz image of freshly excised tumor represented by spectral power, (b) Time domain THz image of FFPE tissue block represented by peak value, (c) Low power pathology image (d) Time domain signals of normalized reflected electric field at selected pixels ①-④, (e) Spectrum of normalized reflected electric field of the signals shown in (d). The high power pathology images of surrounding regions of ①-④ are shown. All THz signals are normalized with respect to a reference signal reflected from a gold mirror.

red color, cancer infiltrated in fat ② with a yellowish-blue color, fat ③ as a dark blue region, and muscle ④ as a yellow region.

3.7. Tumor 7

The results of Tumor 7 (12-A) are shown in Fig. 9. The THz image of the freshly excised tumor in Fig. 9a shows little contrast between different tissue types. As can be seen from Fig. 9c, the tumor is mostly cancerous with a little bit of fibrous, fat and muscle tissue within the cancerous

regions. The fat region ④ is partially shown in blue color in Fig. 9a with clear differentiation from the cancer region ① (red color). Many of the dark blue spots in Fig. 9a could be due to air bubbles (which can be seen in the zoomed photograph in Table 1). The blue outline of the image is due to the edge effect as discussed earlier. The higher reflection region in Fig. 9a is primarily due to excessive fluid or blood beneath the tissue surface because of the pressure when the tissue was positioned between two polystyrene plates. The light yellow regions mixed in red color

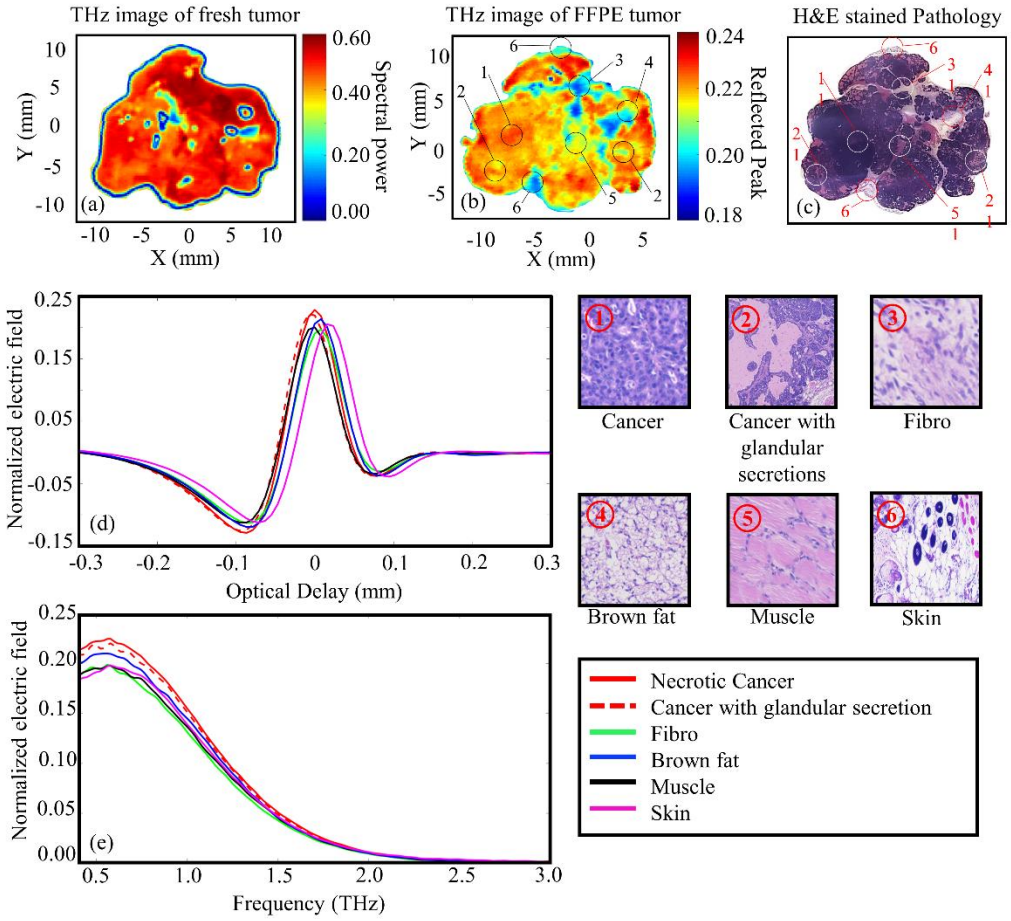

Fig. 9 THz reflection images of transgenic mice breast tumor 7(12-A), (a) Frequency domain THz image of freshly excised tumor represented by spectral power, (b) Time domain THz image of FFPE tissue block represented by peak value, (c) Low power pathology image (d) Time domain signals of normalized reflected electric field at selected pixels ①-⑥, (e) Spectrum of normalized reflected electric field of the signals shown in (d). The high power pathology images of surrounding regions of ①-⑥ are shown. All THz signals are normalized with respect to a reference signal reflected from a gold mirror.

regions in the lower left side of the image in Fig. 9a are the less dense cancer regions. Here cancer cells are forming glandular structures ② filled with some protein secretions. The THz image of the FFPE tissue in Fig. 9b shows good agreement with the pathology image in Fig.9c as demonstrated in the other tumors. The regions of cancer ① are shown in red, the cancer with glandular secretion ② is shown in yellowish-red, the muscle ⑤ is shown in yellow, the fibro ③ is shown in dark blue, the brown fat ④ is shown in yellowish-blue, and the skin ⑥ is shown in

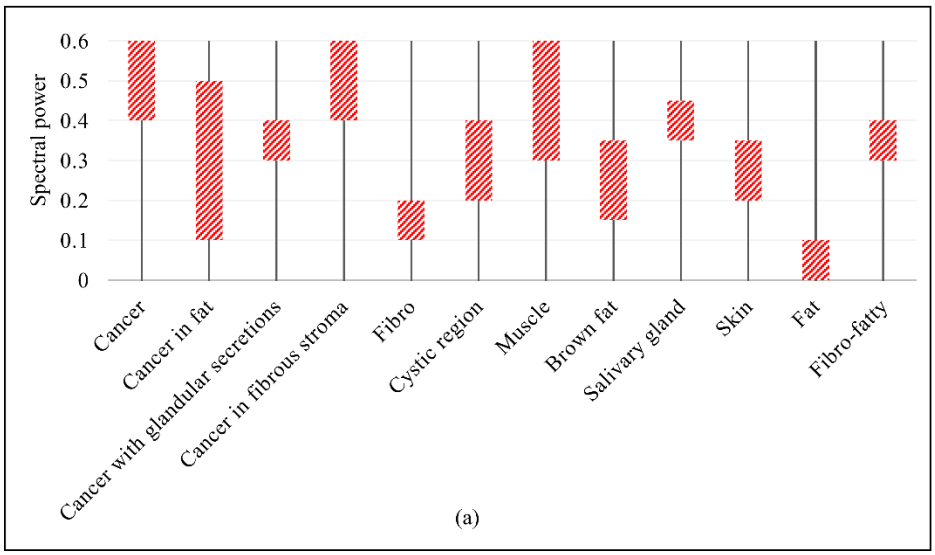

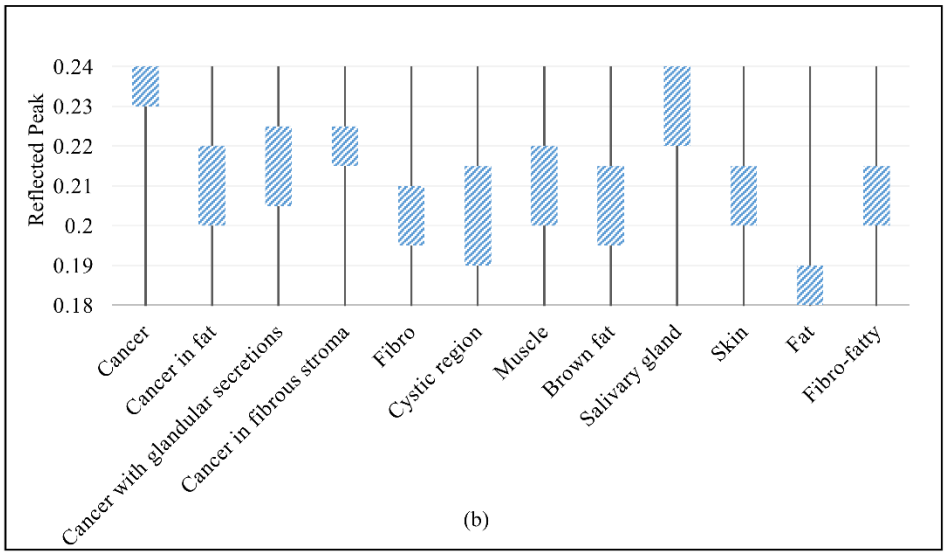

Fig. 10. Summary Charts for (a) Fresh tumors, and (b) FFPE tissue block.

cyan. It should be noted that the skin is not present in the fresh tissue image in Fig. 9a because it was on the upper surface and was folded over during the histopathology process. The time domain and frequency domain signals in Fig. 9d and 9e are in good correlation with the THz image in Fig. 9b, showing the high reflection comes from the cancer regions and the lower reflection comes from the fibro region.

The above discussion is summarized in Fig. 10, where the estimated limits of the THz spectral power and reflected peak obtained from the THz images in Figs. 3-9 is presented in Fig. 10a and 10b, respectively.

4. Conclusion

In this work we presented THz images of fresh and FFPE tissue block tumors excised from transgenic mice. The images were obtained using the reflection mode of the THz imaging system where no contrast agent or staining ink was used. The MMTV-PyMT breast cancer transgenic model was used in this work. The transgenic mice spontaneously produced multiple tumors without the need to inject carcinogens, with the tumors exhibiting complex structures with multiple tissue types like fat, cancer, fibro, muscle, cancer with glandular secretions, fat infiltrated with cancer, and others. A total of fifteen tumors were excised from four transgenic mice and were imaged using pathology and THz techniques, seven of which were presented here. Both fresh and FFPE tissue block were scanned on the THz imager and their images were compared with the low power pathology images. At the same time, high power pathology images were produced to demonstrate the complexities of the transgenic mice tumors and to designate different regions in the THz images. Almost all tumors presented in this work demonstrated advanced stages where cancer infiltrated other tissues like fat and fibrous stroma, and in some cases cancer became necrotic. In spite of the aggressiveness of the cancer in these tumors, their maximum size did not

exceed 2.5 cm. Furthermore, we observed that the transgenic mice tumors did not contain significant fibroblast tissues surrounding the cancer that we clearly saw in our research on human breast tumors [28]. Therefore, while THz imaging is shown here to be effective in distinguishing between the complex tissue regions, the transgenic tumors were not suitable for us to investigate the margins of these tumors as a direct parallel to human breast cancer.

The results of this work demonstrated a partial success in differentiation between the cancer and the diverse tissue regions within the tumor. The summary in the Figs. 10a and b demonstrated the range of the signal amplitude for each tissue type. For example, in fresh tissue the signal of aggressive cancer ranges from 0.4 to 0.6, cancer in fat ranges from 0.1 to 0.5, etc., while in FFPE tissue, it was 0.23 to 0.24, 0.2 to 0.22, etc. The pathology reports indicated each tissue type and were used to qualitatively validate the THz images. The results of Fig. 10 demonstrated that THz imaging of FFPE tissue blocks clearly differentiates between aggressive cancer (i.e. complete invasion of tissue) and other tissue types. However, when cancer partially invaded fat and fibro regions and/or when cancer has glandular secretions, the differentiation was not seen. In the meantime, only 50% of the fifteen fresh tumors investigated here showed reasonable correlation between THz images with pathology. This observation is consistent with our preliminary work on human breast tumors [28]. The results show that THz imaging demonstrates contrast between cancer and healthy tissue even without the strong interaction of water (FFPE tissue), though water's effect must be considered for surgical procedures. It has been observed that some of the tumors release more fluid than others during the fresh tissue imaging procedure despite the effort to dry it using filter paper before positioning on the scanner. The main challenges in differentiating between different tissue types in fresh tumors imaging are (i) the possible presence of fluid (water, necrotic secretions, blood, etc.) beneath the tissue surface, (ii) the degradation of fibrous and fatty

tissues once the cancer invades the surrounding regions, especially in the transgenic mice tumors in this work, and (iii) the histopathology process sometimes alters the tumor tissue shape, size, and imaging surface making the correlation with pathology more challenging compared with THz images of FFPE tissue block. Overcoming these challenges (i)-(iii) is an ongoing research objective for advancing THz imaging of fresh tumors for its use in in-vivo clinical diagnosis. Additional future work is to conduct biochemistry analysis of cancer and fibro tissues in order to understand the difference in the THz response from these tissue types.

Acknowledgments

This work was funded by the National Institutes of Health Award No. R15CA208798. It was also funded in part by the National Science Foundation (NSF) Award No. 1408007. Funding for the pulsed THz system was obtained through NSF/MRI Award No. 1228958.

References

1. R. L. Siegel, K. D. Miller, and A. Jemal, "Cancer statistics, 2018," CA. Cancer J. Clin. 68(1), 7–30 (2018).

2. American Cancer Society, "Cancer Facts & Figures 2016," Cancer Facts Fig. 2016 1–9 (2016).

3. M. R. Grootendorst, M. Cariati, S. E. Pinder, A. Kothari, M. Douek, T. Kovacs, H. Hamed, A. Pawa, F. Nimmo, J. Owen, V. Ramalingam, S. Sethi, S. Mistry, K. Vyas, D. S. Tuch, A. Britten, M. Van Hemelrijck, G. J. Cook, C. Sibley-Allen, S. Allen, and A. Purushotham, "Intraoperative Assessment of Tumor Resection Margins in Breast-Conserving Surgery Using ^{18}F-FDG Cerenkov Luminescence Imaging: A First-in-Human Feasibility Study," J. Nucl. Med. 58(6), 891–898 (2017).

4. K. J. Blair and M. Legenza, "Re-Excision Rates Following Breast Conserving Therapy : A Single Institutions Experience Over Ten Years," Marshall J. Med. 3(3), 68-74 (2017).

5. B. B. Hu and M. C. Nuss, "Imaging with terahertz waves," Opt. Lett. 20(16), 1716 (1995).

6. P. C. Ashworth, E. Pickwell-macpherson, E. Provenzano, S. E. Pinder, A. D. Purushotham, M. Pepper, and V. P. Wallace, "Terahertz pulsed spectroscopy of freshly excised human breast cancer," 17(15), 93–94 (2009).

7. T. Löffler, T. Bauer, K. Siebert, H. Roskos, A. Fitzgerald, and S. Czasch, "Terahertz dark-

field imaging of biomedical tissue," Opt. Express 9(12), 616–621 (2001).

8. A. J. Fitzgerald, V. P. Wallace, M. Jimenez-Linan, L. Bobrow, R. J. Pye, A. D. Purushotham, and D. D. Arnone, "Terahertz Pulsed Imaging of Human Breast Tumors," Radiology 239(2), 533–540 (2006).

9. P. Knobloch, K. Schmalstieg, M. Koch, E. Rehberg, F. Vauti, K. Donhuijsen, I. Hochfrequenztechnik, T. U. Braunschweig, D.- Braunschweig, H. D. U. Witten, and D. Katholischen, "THz imaging of histo-pathological samples Frequency (Hz)," Proc. SPIE - Int. Soc. Optival Eng. 4434, Hybrid Nov. Imaging New Opt. Instrum. Biomed. Appl. 239 (October 24, 2001); doi10.1117/12.446686 4434, 239–245 (2001).

10. T. Bowman, M. El-Shenawee, and L. K. Campbell, “Terahertz transmission vs reflection imaging and model-based characterization for excised breast carcinomas,” Biomed. Opt. Express 7, 3756–3783 (2016).

11. T. C. Bowman, M. El-Shenawee, and L. K. Campbell, “Terahertz imaging of excised breast tumor tissue on paraffin sections,” IEEE Trans. Antennas Propag. 63, 2088–2097 (2015).

12. T. Bowman, Y. Wu, J. Gauch, L. K. Campbell, and M. El-Shenawee., “Terahertz imaging of three-dimensional dehydrated breast cancer tumors,” J. Infrared Millimeter Terahertz Waves 38, 766– 786 (2017).

13. G. M. Png, J. W. Choi, B. W-HNg, S. P. Mickan, D. Abbott and X-C Zhang, “The impact of hydration changes in fresh bio-tissue on THz spectroscopic measurements,” Phys. Med. Biol. 53**,** 3501–3517, (2008).

14. Yu C, Fan S, Sun Y, Pickwell-MacPherson E. "The potential of terahertz imaging for cancer diagnosis: A review of investigations to date", Quant Imaging Med Surg; 2:33-45, (2012).

15. Jakubowski DB, Cerussi AE, Beilacqua F, et al. Monitoring neoadjuvant chemotherapy in breast cancer using quantitative diffuse optical spectroscopy: a case study. *J Biomed Opt*;9(1):230–238 (2004).

16. Chen JY; Knab JR, Markelz AG et al. Terahertz dielectric response sensitivity to protein oxidation state. *Lasers and Electro-Optics Society*, 2007. LEOS 2007. The *20th Annual Meeting of the IEEE*, (2007).

17. H. Chen, T.-H. Chen, T.-F. Tseng, J.-T. Lu, C.-C. Kuo, S.-C. Fu, W.-J. Lee, Y.-F. Tsai, Y.-Y. Huang, E. Y. Chuang, Y.-J. Hwang, and C.-K. Sun, "High-sensitivity in vivo THz transmission imaging of early human breast cancer in a subcutaneous xenograft mouse model," Opt. Express 19(22), 21552 (2011).

18. T. Bowman, T. Chavez, K. Khan, J. Wu, A. Chakraborty, N. Rajaram, K. Bailey, and M. El-Shenawee, “Pulsed terahertz imaging of breast cancer in freshly excised murine tumors,” *J. Biomed. Opt.*, vol. 23, no. 2, 1-13, (2018).

19. S. J. Oh, S.-H. Kim, Y. Bin Ji, K. Jeong, Y. Park, J. Yang, D. W. Park, S. K. Noh, S.-G.

Kang, Y.-M. Huh, J.-H. Son, and J.-S. Suh, "Study of freshly excised brain tissues using terahertz imaging," Biomed. Opt. Express 5(8), 2837 (2014).

20. S. Yamaguchi, Y. Fukushi, O. Kubota, T. Itsuji, T. Ouchi, and S. Yamamoto, “Brain tumor imaging of rat fresh tissue using terahertz spectroscopy,” *Sci. Rep.*, vol. 6, no. 30124, pp. 1–6, (2016).

21. A. Richmond and Y. Su, "Mouse xenograft models vs GEM models for human cancer therapeutics," Dis. Model. Mech. 1(2–3), 78–82 (2008).

22. C. T. Guy, R. D. Cardiff, and W. J. Muller, "Induction of mammary tumors by expression of polyomavirus middle T oncogene: a transgenic mouse model for metastatic disease.," Mol. Cell. Biol. 12(3), 954–961 (1992).

23. M. Plodinec, M. Loparic, C. A. Monnier, E. C. Obermann, R. Zanetti-Dallenbach, P. Oertle, J. T. Hyotyla, U. Aebi, M. Bentires-Alj, R. Y. H. Lim, and C. A. Schoenenberger, "The nanomechanical signature of breast cancer," Nat. Nanotechnol, vol. 7, 757-765, (2012).

24. E. Y. Lin, J. G. Jones, P. Li, L. Zhu, K. D. Whitney, W. J. Muller, and J. W. Pollard, "Progression to Malignancy in the Polyoma Middle T Oncoprotein Mouse Breast Cancer Model Provides a Reliable Model for Human Diseases," Am. J. Pathol. 163(5), 2113–2126 (2003).

25. K. Almholt, K. A. Green, A. Juncker-Jensen, B. S. Nielsen, L. R. Lund, and J. Rømer, "Extracellular proteolysis in transgenic mouse models of breast cancer," J. Mammary Gland Biol. Neoplasia 12(1), 83–97 (2007).

26. J. E. Maglione, D. Moghanaki, L. J. T. Young, C. K. Manner, L. G. Ellies, S. O. Joseph, B. Nicholson, R. D. Cardiff, and C. L. MacLeod, "Transgenic Polyoma middle-T mice model premalignant mammary disease," Cancer Res. 61(22), 8298–8305 (2001).

27. C. B. Reid, A. Fitzgerald, G. Reese, R. Goldin, P. Tekkis, P. S. O’Kelly, E. Pickwell-MacPherson, A. P. Gibson, and V. P. Wallace, “Terahertz pulsed imaging of freshly excised human colonic tissues,” *Phys. Med. Biol.*, vol. 56, no. 1, pp. 4333–4353, (2011).

28. M. El-Shenawee, T. Bowman, T. Esparza, K. Khan, J. Wu, A. Chakraborty, and K. Bailey, “Statistical Signal Processing For Quantitative Assessment Of Pulsed Terahertz Imaging Of Human Breast Tumors,” *Proc. of the 42nd International Conference on Infrared, Millimeter and Terahertz Waves*, Cancun, Mexico, 27 August (2017).

Appendix

We conducted spectroscopy experiments of Dulbecco’s Modified Eagle Medium (DMEM) and Phosphate-Buffered Saline (PBS) solutions. A 100 µm thick quantity of the solution is placed in the liquid sample holder of the system. The extracted refractive index and absorption coefficients

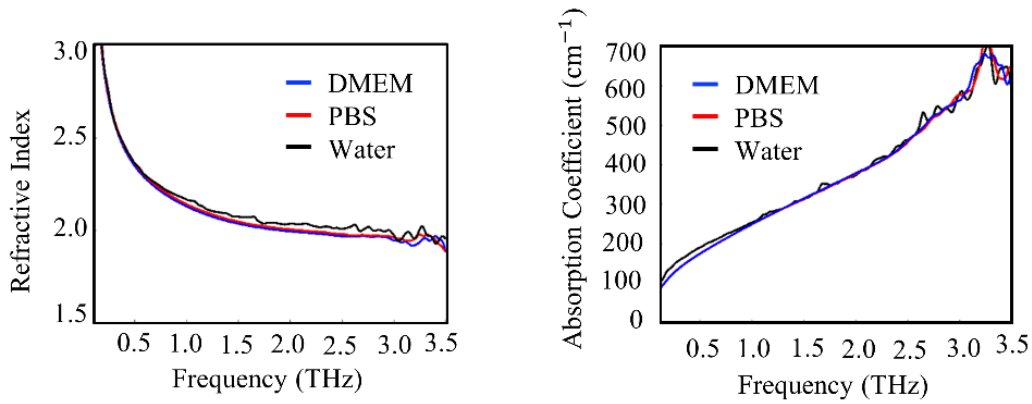

Fig. A1 Refractive index and absorption coefficient of DMEM, PBS, and water vs frequency.

compared with distilled water are shown in Fig. A1. The results show that these solutions have THz signature similar to water.

CHAPTER 4

Mammary tumors in Sprague Dawley rats induced by N-ethyl-N-nitrosourea for evaluating terahertz imaging of breast cancer

Abstract

Purpose: The objective of this study is to quantitatively evaluate terahertz (THz) imaging for differentiating cancerous from non-cancerous tissues in mammary tumors developed in response to injection of N-ethyl-N-nitrosourea (ENU) in Sprague Dawley rats.

Approach: While previous studies have investigated the biology of mammary tumors of this model, the current work is the first study to employ an imaging modality to visualize these tumors. A pulsed THz imaging system is utilized to experimentally collect the time-domain reflection signals from each pixel of the rat's excised tumor. A statistical segmentation algorithm based on the expectation-maximization (EM) classification method is implemented to quantitatively assess the obtained THz images. The model classification of cancer is reported in terms of the receiver operating characteristic (ROC) curves and the areas under the curves.

Results: The obtained low-power microscopic images of 17 ENU-rat tumor sections exhibited the presence of healthy connective tissue adjacent to cancerous tissue. The results also demonstrated that high reflection THz signals were received from cancerous compared with non-cancerous tissues. Decent tumor classification was achieved using the EM method with values ranging from 83% to 96% in fresh tissues and 89% to 96% in formalin-fixed paraffin-embedded tissues.

Conclusions: The proposed ENU breast tumor model of Sprague Dawley rats showed a potential to obtain cancerous tissues, such as human breast tumors, adjacent to healthy tissues. The implemented EM classification algorithm quantitatively demonstrated the ability of THz imaging in differentiating cancerous from non-cancerous tissues.

1. Introduction

Terahertz (THz) imaging has emerged as a potential clinical technology for noninvasive and nonionizing evaluation of breast tumor margins [1-5]. Leveraging its sensitivity to water content, THz imaging has been used to determine the differences between normal and diseased tissue in several organs [6-10]. To establish the feasibility of THz imaging for imaging breast tumor margins, we and others have shown the ability of THz imaging to distinguish between tumors and the surrounding fatty tissue in subcutaneous tumor xenograft models of breast cancer [11-14]. These tumor models are established from subcutaneous injections of immortalized cancer cells and result in the formation of distinct tumor cells and fatty tissue compartments. However, these tumors are nearly devoid of fibrous tissue and therefore do not adequately represent the complexity of human breast cancer. Recent work from our group demonstrated the first THz imaging study [15] in a transgenic mouse model of breast cancer [mouse mammary tumor virus-polyoma middle T antigen (MMTV-PyMT)], which has been used extensively as a preclinical model of breast cancer due to its similarities to the complexity and progression of human breast cancer [16, 17]. Despite the incredible tumor heterogeneity that was similar to what we have observed in our studies of human breast cancer [4, 18-21], there were appreciable differences in THz signal between different tumor compartments, such as fibrous, adipose (with and without tumor infiltration), tumor, and glandular secretions. However, the relative contributions of fatty and fibrous tissue to these tumors were still not reflective of human breast cancer [22]. Specifically,

these transgenic tumors exhibit progressive degradation of the extracellular matrix with tumor progression, resulting in nearly 70-80% of the tumor being composed of adipose tissue at the time of tumor excision in our study. In our previous work [4], we reported tomographic images of freshly excised cancerous and healthy tissues obtained from patients and breast reduction surgeries, respectively. It is a continuous challenge, in cost and frequency, to acquire an adequate number of freshly excised human tumors that include normal tissue adjacent to cancerous tissue needed to assess the tumor margins. While no model can perfectly replicate human disease, our use of THz imaging and image analysis algorithms that leverage differences in the reflection signatures from different tissue compartments necessitate the use of a model that is a closer representation of the human breast tumors.

The development of carcinogen-induced mammary tumors in rodents has been used as a preclinical model, albeit not as extensively as transgenic or tumor xenograft models. Studies have shown that injection of N-ethyl-N-nitrosourea (ENU) results in reliable growth of benign and malignant mammary tumors [23-25]. These tumors have several similarities to human breast cancer, including elevated serum calcium and local invasion into the stroma and muscle. Rats were found to develop mammary tumors between 50- and 155-days post-injection [25]. As such, the ENU model of breast cancer has the potential to present tumors that are like human breast tumors in both complexity and composition (i.e. presence of cancerous adjacent to fatty and healthy connective tissues).

The objective of this study is to determine the ability of THz imaging to differentiate cancerous and non-cancerous tissue in mammary tumors that develop in response to injection of ENU in rats. While previous studies by others conducted investigations of mammary tumor biology in these models [26-28], this is the first study to employ an imaging modality to visualize these tumors. In

addition to imaging cancer and non-cancer tissue within each tumor in both fresh and formalin-fixed paraffin-embedded forms (FFPE), we also report the results of a new classification analysis based on the expectation maximization technique [29] and a side-by-side comparison with xenograft and transgenic mice models. To ensure an objective comparison across all tumor models, our classification algorithm only considers two compartments— cancer and non-cancer.

This work is organized as follows: methodology describing the rodent injections, pulsed THz imaging system, pre-image preparation of fresh tumor tissue, and image segmentation based on the expectation maximization technique are discussed in Section 4.2, results of THz imaging of ENU-rat tumors, a comparison to other mice tumor models, and THz image analysis and classification are presented in Section 4.3, and conclusion and future work is discussed in Section 4.4. The microscopic imaging and image analysis procedure is discussed in Appendix.

2. Methodology

2.1. ENU Tumor Induction in Rats

All the rats handled in this work were injected with N-ethyl-N-nitrosourea (ENU) chemical solution at the Oklahoma State University. Two batches of ten 30-day old female Sprague Dawley rats were purchased from Charles River, Wilmington, MA, USA, and housed to acclimate for at least two days after arrival. The rats were kept two per cage in static filtered microisolator cages with corn cob bedding (Bed' OCobs, Maumee, OH, USA). Rats were fed rodent chow (Lab Diet 5001, St. Louis, MO, USA) and tap water ad libitum. The weight of the rats ranged between 150 and 186 grams. An amount of 15 mL of phosphate citrate buffer (Sigma-Aldrich, Milwaukee, WI, USA) was infused into the ipsopac containing the ENU solution (Sigma-Aldrich, Milwaukee, WI, USA). The rats were given 165 mg/kg of the ENU solution intraperitoneally in the lower right quadrant of the peritoneal cavity. All the animal procedures were performed in a chemical safety

fume hood [30]. The cages were changed every four days, with the waste being handled as chemical hazardous for the first four days. Two weeks after inoculation, the rats were shipped to the University of Arkansas, where they were housed in the animal facility. The rats were maintained at standard 12-hour light/dark cycles with regular access to food and water. Tumors were excised between 9 and 21 weeks, with sizes ranging between 8 mm and 18 mm in diameter.

The protocols for injecting rats with ENU chemical to produce mammary tumors were approved by the Institutional Animal Care and Use Committee (IACUC) of the Oklahoma State University. Additionally, protocols for all rat experiments were approved by the Institutional Animal Care & Use Committee (IACUC) of the University of Arkansas.

2.2. Pulsed Terahertz Imaging System

The diagram of the pulsed terahertz system utilized in this work is shown in Fig. 1. The terahertz emitter and receiver antennas are voltage biased bow-tie antennas on the GaAs substrate

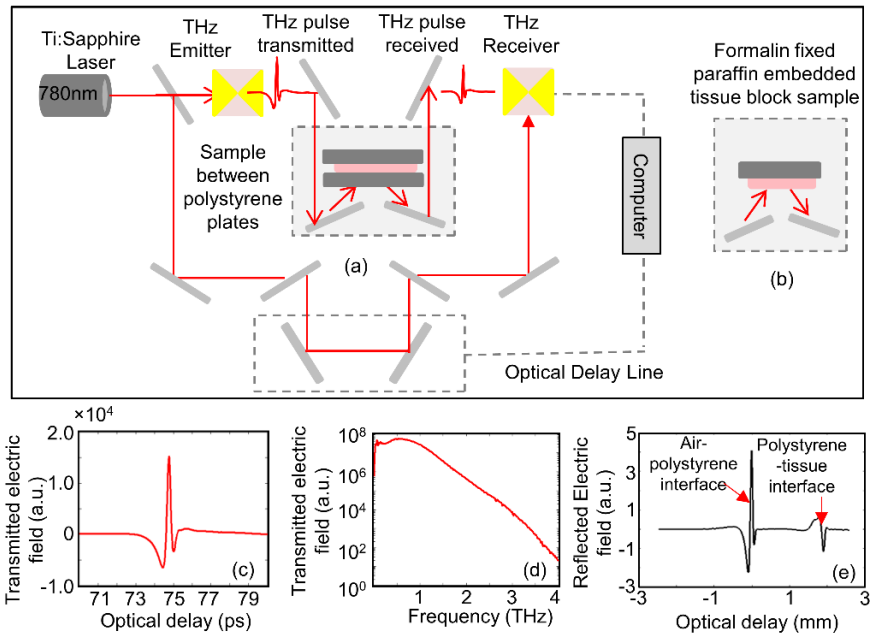

Fig. 1. Terahertz system diagram in reflection mode (a) for fresh tissue placed between two polystyrene plates, (b) for FFPE tissue block, (c) Time domain THz pulse, (d) Fourier transform of the THz pulse in (c), and (e) Reflection signals from the polystyrene-tissue arrangement in (a).

[21]. Fig. 1c shows the generated THz signal upon excitation with a 780 nm wavelength Ti: Sapphire laser beam. The Fourier transform of the time domain pulse gives the spectrum ranging from 0.1 THz to 4 THz, Fig. 1d. The generated THz pulse is directed onto the tissue sample, and the reflected signal is collected at the receiver antenna. For fresh tissue imaging, the specimen is placed between two polystyrene plates. The incident THz signal is directed on this polystyrene-tissue arrangement, and the reflected signal is recorded at the receiver antenna. In this case, two reflected pulses are received, one from the air-polystyrene interface and the second from the polystyrene-tissue interface, Fig. 1e. To record the reflected data from the tissue, the first pulse is windowed-out, and only the second pulse is recorded at each pixel on the tissue [21]. In this case, the power spectra image is constructed across a frequency range from 0.5 THz to 1.0 THz as:

$$\text{Spectral power} = \int_{0.5\ \text{THz}}^{1.0\ \text{THz}} \frac{|\mathrm{E_{samp}}(f)|^2}{|\mathrm{E_{ref}}(f)|^2}\, \mathrm{d}f \tag{1}$$

where E_{samp} is the magnitude of the Fourier transform reflected sample signal, E_{ref} is a single point reference signal obtained from the air-polystyrene interface, and f is the frequency in THz. For the FFPE block tissue imaging, the block is placed directly onto the scanner, and the reflected time domain peak signal is collected at each pixel to construct the time domain THz image [18].

2.3. Pre-image Preparation of Fresh Tumor Tissue

Upon excising the tumor from the rat with adequate healthy normal margin, it was immersed in phosphate buffered saline (PBS) for transfer from the excision site to the THz lab in the same building. As shown in Fig. 2a, the bulk tumor was bisected into two halves, such that each section has surrounding healthy normal tissue in Fig. 2b.

For performing the THz imaging, the tumor was first dried for around 3-4 minutes on a grade-1 filter paper, Fig. 2c. The tumor section was then positioned between two polystyrene plates

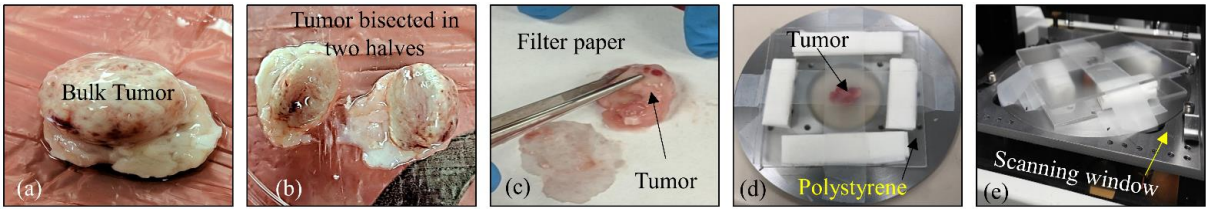

Fig. 2. Rat # 1 fresh tissue preparation for THz imaging. (a) Photograph of bulk tumor excised from rat tumor #1, (b) Bulk tumor bisected into two halves, (c) Tumor placed on filter paper to remove excess fluid, (d) Tumor positioned between two polystyrene plates, and (e) Polystyrene-tumor-polystyrene arrangement placed on the scanning window.

with gentle pressure from the top to make the tumor surface as flat as possible for imaging, as shown in Fig. 2d. We have not observed tissue dehydration due to air exposure as reported in [31]. The main reason was that during the ~ 35 minutes scanning process, the tissue was placed between two polystyrene plates as shown in Fig. 2d. This arrangement minimized tissue exposure to air and hence minimized tissue dehydration. In addition, during the scanning we often observe excess fluids at the tissue perimeter indicating that tissue maintains hydration. This tissue arrangement was then placed on the scanning window prepared for the reflection imaging, Fig. 2e. The x-y scanner motors were set to increment at every 200 µm step size to collect reflection data at each pixel on the specimen [21]. The THz imaging system scans the tissue using a raster scanner of different motor step size that ranges from 50 µm to 500 µm. While using a step size of 50 µm provides a higher resolution image [18], the time consumed in the raster scanner drastically increases depending on the tissue size. For example, the rat tumor #2- section 2 fresh tissue of size ~16.5 x 11 x 5.9 mm, shown in Fig. 4g, took ~ 25 minutes to produce the THz image using 200 µm. It is estimated that imaging the same sample could take ~ 388 minutes using 50 µm step size. Therefore, in this work, a step size of 200 µm is selected to quickly provide adequate image resolution to differentiate between tumor tissue types with a reasonable trade-off in scanning time. After completing the scanning, the tissue was immersed in a 10% buffered formalin solution and shipped to the Oklahoma Disease Diagnostic Laboratory for the histopathology process. In the

histopathology process, all the fluid and lipids were extracted from the tissue (dehydrated tissue). Finally, the tumor was embedded in a paraffin block from which a 3-4 µm thick flat tissue section was sliced, stained with standard hematoxylin and eosin (H&E) ink, and fixed on glass slides. The FFPE tissue block and the H&E stained tissue glass slides are imaged using the THz reflection imaging system and the Nikon SMZ745T and NIKON Eclipse Ci microscopes, respectively. The scanner motors in the THz system were first set up to 400 µm step size to obtain quick images for adjusting the boundaries, but a finer step size of 200 µm was used to obtain the final THz images shown in this work.

2.4. Image Segmentation Based on the Expectation Maximization Technique

The THz images were assessed with respect to the pathology images as the ground truth of tumors. However, a pathology image has an inherently higher resolution than the THz image. Additionally, due to the dehydration process that the sample goes through during the histopathology process, a shape mismatch occurs between the pathology image and the THz image of fresh tissue [32]. Due to these factors and to compare the two images at a neutral ground, two statistical processes are implemented. First, a mesh morphing algorithm is used to digitize the pathology image and generate a classification at the same resolution and orientation as the THz image as reported in [13]. Our algorithm in [13] is implemented here to correct the alignment, resolution, and shape mismatch between these images. Such an algorithm utilizes control points within the contour of the images to provide a reference pathology for the pixel-by-pixel evaluation of the segmentation results. The obtained image is referred to as the morphed pathology image. Second, a segmentation algorithm, based on the expectation maximization (EM) technique, is implemented on the THz image data to classify different tissue regions in the sample [33, 34]. The segmentation algorithm utilizes the amplitude of the frequency domain representation of the

reflected THz waveform for each pixel, $\boldsymbol{v}_n \in \mathcal{R}^F$, where F is the number of frequency samples in the spectrum, $n = \{1, \dots, N\}$ is the index of the pixel of interest, and N corresponds to the total number of pixels in the THz image. The THz information for each pixel is represented by a high-dimension vector with $F = 106$ frequency samples, which contains valuable information for the region characterization of the tumor. On the other hand, the high dimension of the THz information vector can negatively impact the model complexity of the segmentation process. Unlike alternative studies that summarize the THz information per pixel into a single physical characteristic, such as the absorption coefficient [35], the proposed algorithm employs a dimension reduction approach to identify the most relevant discriminating features while minimizing the loss of information. Here we utilize the low-dimensional ordered orthogonal projection (LOOP) algorithm [29], which empirically projects the high-dimension waveform per pixel into a lower-dimension subspace containing the most relevant features for the region segmentation of the THz image. The details of the LOOP algorithm and the EM technique were reported in [29, 36].

In addition to implementing the EM technique, we applied other classification methods such as estimating the model parameters within the Gaussian mixture model (GMM) utilizing a Markov chain Monte Carlo (MCMC) process. This procedure iteratively takes samples from the posterior distributions of the mixture model parameters by employing a Gibbs sampling technique [37]. Two versions of the MCMC were tested on the data (not presented due to space limitation); a 1-dimensional MCMC [12] and a higher dimensional MCMC with LOOP [29]. The first algorithm summarizes the THz waveform per pixel into a single feature, which corresponds to the spectral power and the peak of the normalized reflected signal for fresh and FFPE tissue, respectively [12]. While the second algorithm employs the LOOP dimension reduction technique to summarize the THz waveform per pixel into a lower dimension representation of the data with at least two

features. A previous study compared the segmentation results obtained through EM and MCMC for the detection of breast cancer in THz imaging and concluded that the EM algorithm presents the best overall segmentation performance among these approaches [29]. It is important to clarify that the samples presented in this paper were analyzed by considering different dimension sizes within the LOOP algorithm, ranging from two to six dimensions. For consistency, we present the EM results obtained through the dimension size that achieved the best overall detection performance.

3. Experimental and Image Analysis Results

A total of 9 tumors were obtained from 20 ENU induced Sprague Dawley rats, while the rest did not produce any tumors in the expected period of 9-21 weeks and were sacrificed according to the protocol. The obtained tumors were bisected into two sections, as shown in Fig. 2. The low power pathology images of 17 tumor sections obtained from the 9 rat tumors are presented in Fig. 3. The details of the low power pathology process of stitching are clarified in Appendix. The microscopic images of Figs. 3a-3q shows that the rat tumors exhibit cancer tissues adjacent to pre-existing normal fibro-fatty tissue with healthy mammary ducts and glands, mimicking the human breast tissue reported in [4, 18-21]. The microscopic images of Figs. 3a, b, f, g, j, l, m, and o, exhibit muscle tissue adjacent to both cancer and healthy fibro-fatty tissues. The muscle tissue is usually not present in human breast cancer excision but could exist in animal model tumors due to the narrow space where the tumor grows in the mammary pad.

Due to the space limitation, we present results for THz images and EM classifications for only three cases of ENU- rat tumors— rat tumor #1- section 2, rat tumor #2- section 2, and rat tumor #9- section 2.

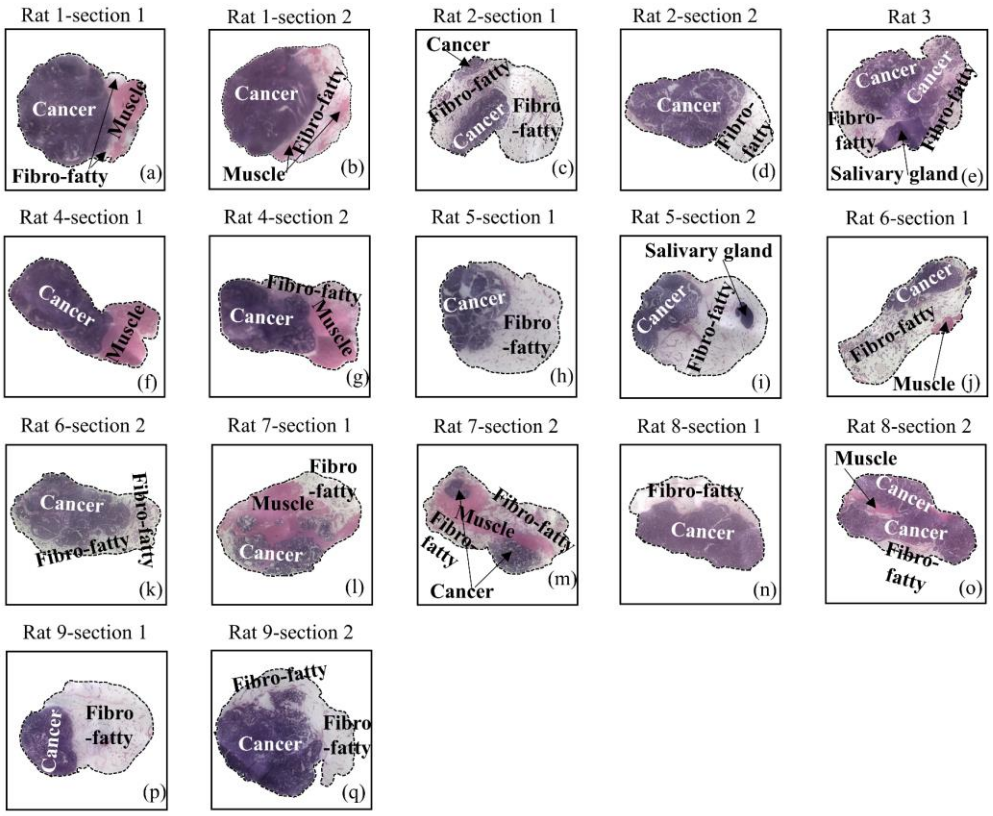

Fig. 3. Low power microscopic images of 17 tumor sections obtained from 9 rat tumors. (a) rat #1- section 1, (b) rat #1- section 2, (c) rat #2- section 1, (d) rat #2- section 2, (e) rat #3, (f) rat #4- section 1, (g) rat #4- section 2, (h) rat #5- section 1, (i) rat #5- section 2, (j) rat #6- section 1, (k) rat #6- section 2, (l) rat #7- section 1, (m) rat #7- section 2, (n) rat #8- section 1, (o) rat #8- section 2, (p) rat #9- section 1, and (q) rat #9- section 2.

3.1. THz Reflection Images

The THz reflection imaging of fresh and FFPE block tumor tissue are presented in Fig. 4. In addition, data of two tumors obtained from our previous mice models [14, 15] are included in the figure for comparison purposes. The first row of Fig. 4 shows the photographs of the fresh tissues starting with rat tumor #1-section 2 in Fig. 4(a), rat tumor #2-section 2 in Fig. 4(e), rat tumor #9-section 2 in Fig. 4(i), xenograft mouse tumor #9-section 214 in Fig. 4(m), and transgenic mouse tumor #14 C15 in Fig. 4(q). The thickness of fresh tissue specimen ranges from 5 to 8 mm in this work. Specifically, the thickness is ~8 mm for rat tumor #1-section 2, ~5.9 mm for rat

tumor #2-section 2, ~5.5 mm for rat tumor #9-section 2, ~5 mm for xenograft mouse tumor # 9-section 2, and ~5 mm for transgenic mouse tumor # 14 C. Following the same order, the results in the second, third, and fourth rows of Fig. 4 show the low-power microscopic pathology images of H&E stained slide (second row), THz power spectra images of the freshly excised tumors (third row), and THz peak time reflection images of the FFPE block tumors (fourth row).

Upon visual inspection of the photographs of xenograft and transgenic mice sections in Figs. 4m and 4q, respectively, the differentiation between cancerous and non-cancerous tissues can be clearly observed. Whereas it is not the case for the ENU-rat tumor photographs in Fig. 4a, 4e, and 4i. Here we can see the advantageous role of utilizing the THz reflection imaging technology to highlight the contrast differentiation between cancerous and non-cancerous tissue sections in the tumors, as shown in Fig. 4.

The tumor of rat #1 was excised on the 63rd day after the chemical injection with a size of ~18 mm diameter. The microscopic low power image in Fig. 4b shows that this tumor exhibits three tissue regions— cancer, fibro-fatty, and muscle. The light purple colored spots seen in the pathology image in Fig. 4b indicate a lack of cancer tissue on the slide (gaps) that is important to mention as it will also be seen in the THz image in Fig. 4d. These gaps could be either pre-existing lumens, which were filled with some secretions when the tissue was fresh, or occurred due to handling the tissue during the histopathology process. Fig. 4c shows the THz imaging of the fresh tumor obtained using the power spectra image using eq. (1) demonstrating the excellent distinction between cancer and the fibro-fatty regions of the tumor. Here, the cancer shows higher reflections (red color) than the fibro-fatty (cyan and blue color). However, no distinction could be observed between the cancer and the muscle regions. This is because the electrical properties of fresh muscle tissue and fresh cancer tissues are similar, in agreement with our previously reported work [12].

In contrast to the fresh tissue THz image, the THz peak reflection image in Fig. 4d shows a clear differentiation between all three regions, with cancer representing higher reflections (red color)

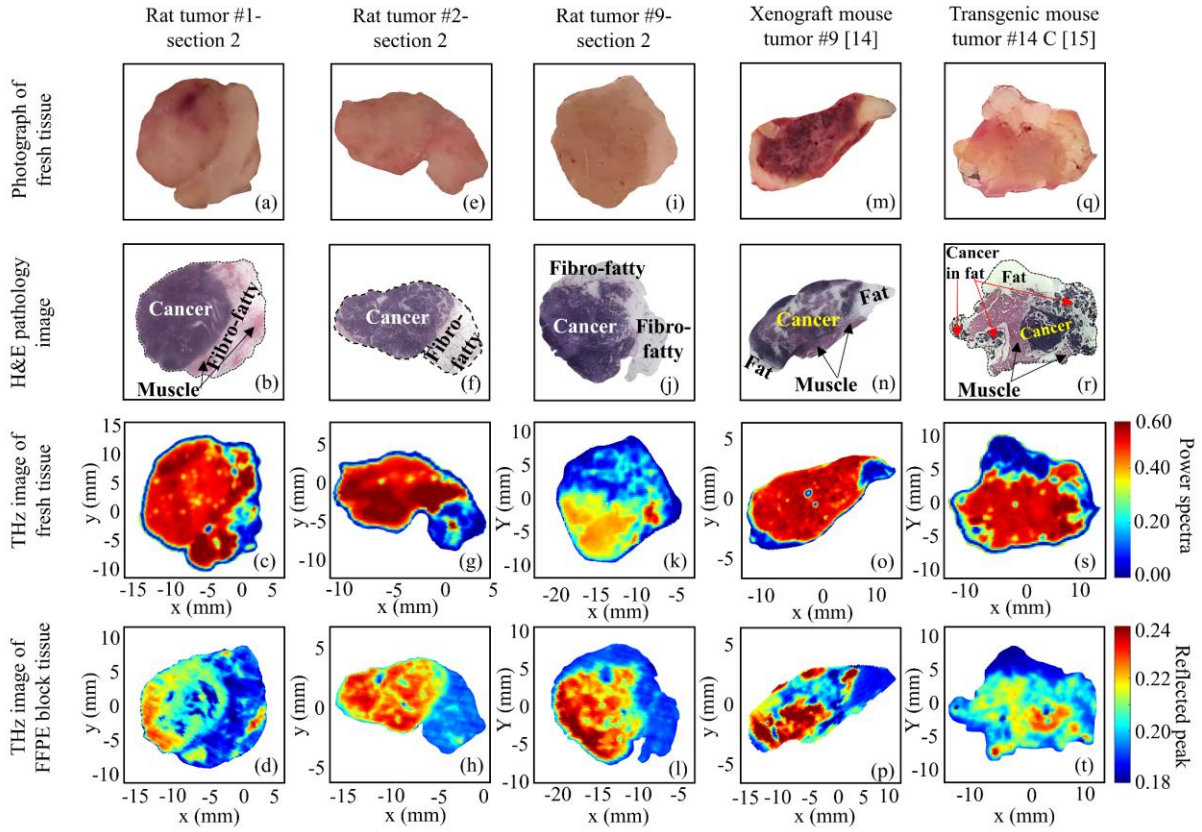

Fig. 4. THz reflection imaging results. For rat tumor #1- section 2 (a) the photograph of the fresh tissue, (b) the low power pathology image, (c) the THz power spectra image of the fresh tissue, (d) the THz time domain peak reflection image of the FFPE block. For rat tumor #2- section 2 (e) the photograph of the fresh tissue, (f) the low power pathology image, (g) the THz power spectra image of the fresh tissue, (h) the THz time domain peak reflection image of the FFPE block. For rat tumor #9- section 2 (i) the photograph of the fresh tissue, (j) the low power pathology image, (k) the THz power spectra image of the fresh tissue, (l) the THz time domain peak reflection image of the FFPE block. For xenograft mouse tumor #9- section 2 (m) the photograph of the fresh tissue [14], (n) the low power pathology image [14], (o) the THz power spectra image of the fresh tissue [14], (p) the THz time domain peak reflection image of the FFPE block [14]. For transgenic mouse tumor #14 C (q) the photograph of the fresh tissue [15], (r) the low power pathology image [15], (s) the THz power spectra image of the fresh tissue [15], and (t) the THz time domain peak reflection image of the FFPE block [15]. Figs. 4m-4p, are reproduced with permission from the IEEE. Figs. 4q-4t, are reproduced with permission from the IOP Publishing, Ltd.

followed by the muscle (light yellow) and fat (blue color). Consistent with the pathology image in Fig. 4b, the THz image in Fig. 4d shows blue color spots inside the cancer region associated with the gaps/lumens filled with the paraffin.

The rat tumor #2 was excised on the 68th day from the chemical injection with a ~11.87 mm tumor diameter. Based on the microscopic image in Fig. 4f, this tumor includes two tissue regions— cancer and fibro-fatty. Here, we also observe in Fig. 4g that the THz power spectra image shows higher power spectra values for the cancer region (red color) compared with the fibro-fatty region (blue and cyan color). In other words, a clear margin between cancer and fibro-fatty tissue regions is seen in this image. This differentiation is also observed in the THz peak reflection image of the FFPE block tumor in Fig. 4h, with cancer demonstrating higher reflection magnitude (red color) than the fibro-fatty region (blue and cyan color). Furthermore, we observe darker red color regions (higher reflection) in the cancer region in Figs. 4c and 4g that could be due to higher density of cancer cells, insufficient drying of the tumor before placing it on the polystyrene plate, or excess fluid secreted out of the tumor due to the pressure from the polystyrene plate during the scanning process.

The third case presented here is for the rat tumor #9 shown in Figs. 4i-4l. This tumor was excised on the 120th day after the chemical injection with a tumor diameter equals to ~10.63 mm. Like the second rat tumor, this tumor also exhibits cancer and fibro-fatty regions, as shown in the microscopic image of Fig. 4j. Consistent with the above cases, the THz power spectra image in Fig. 4k and the peak reflection image in Fig. 4l demonstrate higher reflection values for the cancer region (yellow-red color) in the tumor compared with the fibro-fatty region (blue and cyan color). Upon comparing the THz image of the FFPE block tissue in Fig. 4l and the pathology image in Fig. 4j, we see an excellent qualitative correlation between both images. However, this is not the

case with the fresh tissue image. As discussed in our previous work [32], the histopathology process introduced deformation in tissue shape leading to a change in the imaging surface. Therefore, the correlation between the fresh tissue THz image and pathology image is degraded.

For comparison purposes between three animal breast tumor models, two tumors of different animal models based on mice are included in Fig. 4. The first is the xenograft mice model reported in [12-14], and the transgenic mice model reported in [15]. These three breast cancer animal models represent major differences in the tumor growth process, types of healthy tissues enclosed in the tumor along with cancer, the heterogeneity of the tumor, and the amount of healthy tissue at the tumor margin. As described in Section 2.1, the tumors in the Sprague Dawley rats were induced by injecting ENU chemical in the rat's mammary pad. Whereas the tumors in C57BL/6 black laboratory xenograft mice were induced by injecting E0771 murine breast adenocarcinoma cells in their mammary pad [14]. In contrast to both these methods, the transgenic model did not require any carcinogen injection to induce tumors in the mice's body as it is a genetically modified mice model that grows multifocal tumors spontaneously in the mammary pad [15].

The data of the xenograft and transgenic tumors are shown in Figs. 4m-4t. As observed from the THz imaging point of view, we see a visual consistency in differentiation between different tumor regions. For example, in the THz power spectra image of xenograft mouse tumor #9 in Fig. 4o and the transgenic mouse tumor #14 in Fig. 4s, the cancer shows higher reflections (red color) compared with fat (blue color). Also, like rat tumor #1, the cancer and muscle show similar reflection magnitudes in the fresh tissue images in Figs. 4o and 4s. We also observed consistent THz reflections from different regions in the FFPE block tissue images in Figs. 4p and 4t, for xenograft mouse and transgenic mouse tumors, respectively.

Furthermore, upon comparing the microscopic images of xenograft [14] and transgenic [15] mice tumors in Figs. 4n and 4r, respectively, with the microscopic images of rat tumors in Fig. 3, it can be seen that both mice tumor models lack the presence of pre-existing healthy fibrous tissue in the excised tumors. Both mice tumor models exhibit only fat adjacent to cancer in the tumor. Also, it can be seen that the amount of surrounding healthy tissue available in ENU-rat tumors is more than that in the presented mice models. A numerical comparison between the percentage cancerous pixels in each tumor in three animal models is shown in Table 1 and Fig. 5.

Table 1. Summary of % cancerous pixels in each tumor in Fig. 4

Tumor Type	% of cancer pixels in fresh tumor	% of cancer pixels in FFPE block tumor
Rat #1- section 2	56.61	50.7
Rat #2- section 2	73.22	65.99
Rat #9- section 2	46.12	54.33
Xenograft #9- section 2 [14]	62.70	68.71
Transgenic #14 C [15]	43.09	45.81

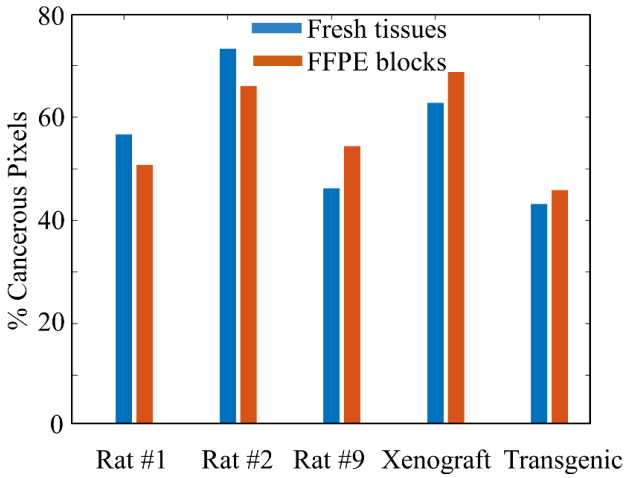

Fig. 5. Percentage of cancerous pixels in each tumor THz image in Fig. 4.

The percentage is achieved through generating binary masks of the tissue under test. The outer mask of the FFPE block is obtained upon mapping the THz image with the pathology image, while the fresh tissue mask was obtained through applying the gradient to the fresh tissue THz image.

The binary masks have values of one for the pixels on the tissue and zeros for the outside pixels. Similarly, a second binary mask is generated for the cancerous region using the guidance of the pathology image for the FFPE tumor and the gradient for the THz fresh tissue. The estimated percentage of cancerous pixels is comparable among the tumors indicating to a general preservation of the surface between the fresh and fixed tissue specimens. Furthermore, despite the very different procedures used to grow the tumors in these three animal models, the percentage of cancerous pixels is consistent with the size of the excised tumors following the IACUC protocol.

3.2. THz Image Classification

The tumor classification results in Fig. 6 are achieved using the EM technique for all tumors presented in Fig. 4. While the THz images of xenograft and transgenic mice tumors are published in [14, 15], the EM classification technique is implemented on these mice tumors here for the first time for comparison purposes. The results are obtained from a binary classification perspective as cancer versus non-cancerous regions, in which any non-cancerous regions in the tumor are merged into a single region. Upon applying the EM segmentation algorithm to the data in Fig. 4, we can obtain the probability that a pixel in the THz image belongs to cancer or non-cancer region. For example, based on the calculation of the EM segmentation algorithm, a given pixel within the THz image can present a 20% chance of belonging to cancer and 80% of belonging to a non-cancerous region. The segmentation results presented in Fig. 6 were obtained by considering the maximum probability among these 2 regions, i.e. a threshold of 50% was utilized for the label assignment of this process. For the binary representation of tumors in Fig. 6, cancer pixels in each tumor are displayed as red color and the non-cancer pixels (fat, fibro, or muscle tissues) as blue color.

The statistical classification results of rat #1 are presented in Figs. 6a-6d. The morphed pathology images, constructed based on the pathology assessment, are obtained separately for both

fresh and FFPE tumors [13], as shown in Figs. 6a and 6c, respectively. The EM model results are shown in Figs. 6b and 6d for the fresh and FFPE tissue, respectively. Although there is no tissue distortion among the pathology results and the THz image of the FFPE tissue, the morphing

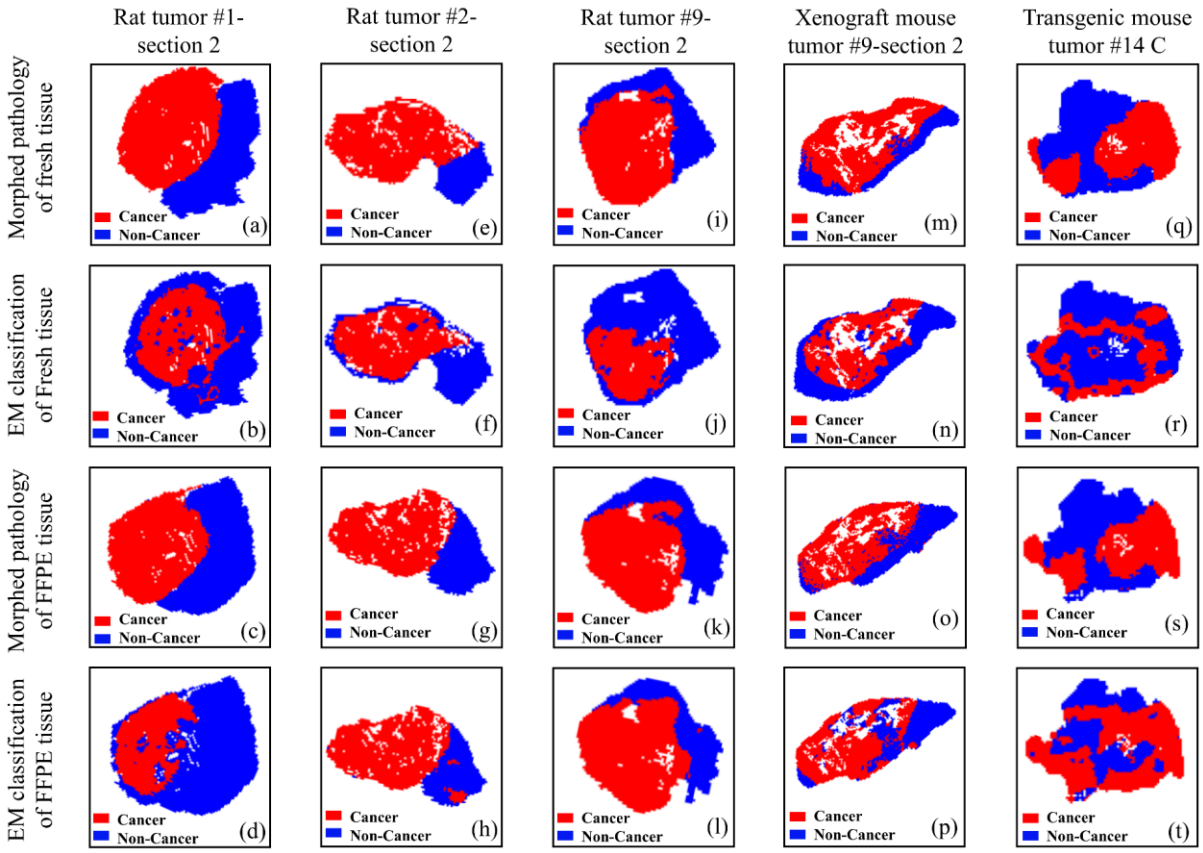

Fig. 6. Statistical classification. Sub-figures (a-d) for rat #1; (a) The morphed pathology for the fresh tissue, (b) The 3D EM detection model results for the fresh tissue, (c) The morphed pathology image for the FFPE tissue block, and (d) The 4D EM detection model results for the FFPE block tissue. Sub-figures (e-h) for Rat # 2; (e) The morphed pathology for the fresh tissue, (f) The 2D EM detection model results for the fresh tissue, (g) The morphed pathology image for the FFPE tissue block, and (h) The 4D EM detection model results for the FFPE block tissue. Sub-figures (i-l) for rat #9. (i) The morphed pathology for the fresh tissue, (j) The 2D EM detection model results for the fresh tissue, (k) The morphed pathology image for the FFPE tissue block, and (l) The 4D EM detection model results for the FFPE block tissue. Sub-figures (m-p) for xenograft mouse #9. (m) The morphed pathology for the fresh tissue, (n) The 2D EM detection model results for the fresh tissue, (o) The morphed pathology image for the FFPE tissue block, and (p) The 3D EM detection model results for the FFPE block tissue. Sub-figures (q-t) for transgenic mouse #14 C. (q) The morphed pathology for the fresh tissue, (r) The 2D EM detection model results for the fresh tissue, (s) The morphed pathology image for the FFPE tissue block, and (t) The 2D EM detection model results for the FFPE block tissue.

algorithm is still applied to the FFPE tissue to correct the resolution and alignment mismatch between these images. For this tumor, the fibro-fatty and muscle tissues are grouped together and classified as non-cancer for the binary representation of the tissue classification results. The results in Fig. 6b represent the classification of tissues in the fresh tumor obtained by the 3D EM model. It can be observed here that the 3D EM segmentation model presents a good visual correlation with respect to the morphed pathology results, where it identifies the cancerous area correctly with minimum non-cancer misclassification. The classification image shown in Fig. 6d represents the FFPE block tumor segmentation results obtained using the 4D EM model. In this figure, we can observe that the 4D EM segmentation results show some misclassification of the non-cancer region but overall shows a good correlation with the microscopic image in Fig. 4a.

The statistical classification results of rat tumor #2 are discussed in Fig. 6e-6h. The morphed pathology image of a fresh and FFPE tumor in Fig. 6e and 6g display cancer and fibro-fatty tissue regions in the tumor as cancer and non-cancer, respectively. The 2D EM classification model results for fresh tumor THz data are presented in Fig. 6f. By visually inspecting Fig. 6f, we can observe that the overall region classification for the EM model shows a good correlation with the morphed pathology results with a very minimum non-cancer misclassification around the edge of the cancer region. Furthermore, the classification results obtained for the FFPE block tumor using the 4D EM model are presented in Fig. 6h. This figure shows that the model represents the correct classification of both cancer and non-cancer regions with a small region of pixels in the non-cancer region classified as cancer. These results are to be compared with the pathology and THz images of rat # 2 in Fig. 4.

The statistical classification results of the third tumor, rat tumor #9, are shown in Fig. 6i-6l. The morphed pathology images of fresh and FFPE tumors showing a binary representation of

tumor as cancer and non-cancer regions are shown in Figs. 6i and 6k, respectively. By visually inspecting the 2D EM classification results in Fig. 6j, we can observe that most of the cancer area located in the lower-left section of the tissue was correctly identified. In contrast, the upper-middle cancerous region within the tissue was mostly misclassified. For the FFPE block tumor, the segmentation image obtained using the 4D EM model presented in Fig. 6l represents the correct classification of both cancer and non-cancer regions. These results are to be compared with the microscopic pathology and THz images of rat # 9 in Fig. 4.

The statistical classification results of the xenograft mouse tumor #9 are shown in Fig. 6m-6p. In the morphed pathology images of fresh and FFPE block tumor in Fig. 6m and 6o, respectively, the fat and muscle tissues are combined and displayed as non-cancer. From the classification imaging results in Fig. 6n, we can observe that the overall region classification for the 2D EM model presents a good correlation with the morphed pathology results and correct classification of muscle as a non-cancer region around the lower-middle edge of the cancer region. The 3D EM model deployed for the FFPE block tumor provides the correct classification of both cancer and non-cancer regions with some misclassification of cancer in the upper right section of the tumor, as presented in Fig. 6p.

Similarly, the classification results of the fifth tumor obtained from transgenic mouse #14 are presented in Figs. 6q-6t. In the morphed pathology images in Figs. 6q and 6s for fresh and FFPE block tumors, respectively, the cancer and cancer in fat are grouped to be classified as cancer, and fat and muscle tissues are grouped to be classified as non-cancer. The segmentation results for the fresh transgenic tumor obtained using the 2D EM model in Fig. 6r represent the misclassification of the cancer area located in the center of the tumor. Similarly, in the 2D EM

classification results of FFPE tumor shown in Fig. 6t, the non-cancer region in the upper-left and lower-left region of the tumor is misclassified as cancer.

The segmentation process shown above is performed by considering the total number of regions within the tissue, but the performance analysis presented here is evaluated in terms of the detection of cancer alone using the operating characteristic (ROC) curves. Ideally, the ROC curves achieve the optimum 100% true detection rate with 0% false detection rate. Therefore, we compare the proposed classifiers' performance by analyzing their proximity to the optimal detection point within the curve. Additionally, we summarize the classifiers' performance by obtaining their areas under the ROC curve, which are then evaluated by considering their proximity to the ideal case, i.e., 100%. A comparison of the ROC curves of cancer for the rats, xenograft mouse, and transgenic mouse is summarized in Fig. 7 and Table 2. In Fig. 7, we present the cancer ROC curves obtained using the statistical EM classification technique of the five tumors presented in Fig. 4. The cancer ROC curves for fresh tissue samples are presented in Fig. 7a and for the FFPE block tissue samples in Fig. 7b.

As mentioned in the Methodology Section, the tumor sections were also classified using the MCMC method, and the areas under the cancer ROC curves are listed in Table 2. Upon comparing the MCMC and EM results, it is clear that the EM technique provided the highest

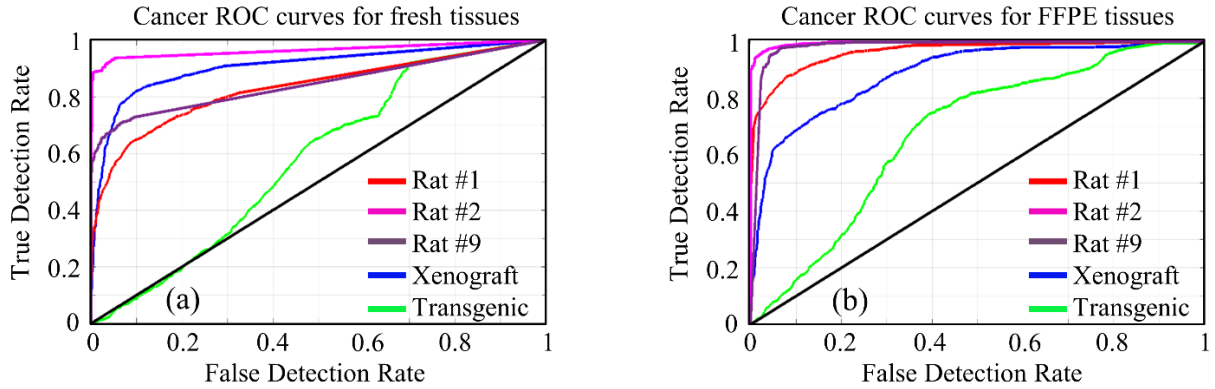

Fig. 7. ROC curves of cancer using the EM technique. (a) fresh tissues, and (b) FFPE tissues.

success rate in most of the cases. For example, the EM provided 96.45 % for rat tumor # 2, followed by the xenograft mouse tumor # 9 with 90.68 %. The classifications of rat tumors # 1and # 9 show

Table 2. Summary of areas under the cancer ROC curves for all samples

Fresh Tissue			**FFPE Block Tissue**		
Rat Tumor #1 Section 2					
1D MCMC	6D MCMC	3D EM	1D MCMC	2D MCMC	4D EM
0.7787	0.8392	0.831	0.7551	0.9347	0.9636
Rat Tumor #2 Section 2					
1D MCMC	2D MCMC	2D EM	1D MCMC	6D MCMC	4D EM
0.9591	0.9284	0.9645	0.9752	0.9949	0.9957
Rat Tumor #9 Section 2					
1D MCMC	5D MCMC	2D EM	1D MCMC	5D MCMC	4D EM
0.7319	0.8356	0.8457	0.9312	0.9711	0.9812
Xenograft Tumor #9 Section 2					
1D MCMC	2D MCMC	2D EM	1D MCMC	2D MCMC	3D EM
0.8647	0.8968	0.9068	0.8633	0.8827	0.8869
Transgenic Tumor #14 C					
1D MCMC	5D MCMC	2D EM	1D MCMC	3D MCMC	2D EM
0.624	0.6551	0.5782	0.5917	0.6878	0.6776

similar performance with ~84 % area under the ROC curve. The performance of the classifier in the rat tumor # 9 could be degraded due to the distortion in the shape of the tumor after the histopathology process, as discussed earlier. Furthermore, we observe that the transgenic mouse tumor #14 C does not show good tissue classification due to the high heterogeneity and complexity observed in the transgenic tumors, as reported in [15]. As cancer invades the other tissue, it became difficult for the classifier to distinguish between the different regions of the transgenic model. Similarly, the EM classification of FFPE block tumors in Fig. 7b presents the best performance among the rat tumors. The results of Table 2 show a success rate with more than 95% area under the ROC curves for rat tumors, followed by xenograft mouse tumor #9 with 88.69%, and then the transgenic mouse tumor with 67.76%. The results of Table 2 are consistent with the classification results of human breast cancer tumors reported in [29].

4. Conclusions

The results obtained in this work highlighted the THz imaging reflection technique and the expectation maximization classification (EM) algorithm of breast cancer in rats. Malignant mammary tumors were grown in Sprague Dawley rats upon injection with the N-ethyl-N-nitrosourea (ENU).

Seventeen tumor sections were obtained from nine tumors once they reached the size of ~18mm in diameter. The freshly excised tissue sections and their associated dehydrated FFPE block tissues were scanned on the imaging system to produce the THz images. The fresh tissue images were based on the reflected signal in the frequency domain using the power spectra formulation, while the FFPE block tissue images were based on the peak of the time domain reflected signal at each pixel. The low power microscopic images of the 17 rat tumor sections were obtained using the high-power microscope, followed by applying the stitching procedure. The obtained images demonstrate that the ENU-tumors induced in rats exhibit the presence of cancer tissue adjacent to healthy fibro-fatty tissues like human breast cancer tumors. This was the motivation of this work as the previously investigated xenograft, and transgenic mice tumor models did not exhibit such resemblance with human breast tumors.

Based on the results obtained in this work, we can conclude that the xenograft tumor model represents the simplest tumor with only cancer and fat regions. The transgenic model represents much more complex heterogeneous tumors with cancer invading the surrounding tissue and expressing advanced-stage tumors. At the same time, the ENU-tumor rat model fits in between the two mice models and closely mimics human breast tumors where healthy fibro-fatty tissues are present adjacent to cancer tissues.

The obtained THz images showed significant differentiation between cancer and healthy tissues in most tumors' sections presented here. A few sections showed the presence of muscle tissue in the tumor, which exhibits reflection signals like the cancer in the THz images shown in Fig. 4. As a result, the presence of muscle tissue introduced some challenges in the EM classification; however, muscle tissue is not a concern in human breast tumors. While THz images of the FFPE block tissue show a good correlation with the pathology image, the challenge remains in the correlation between the THz image of fresh tissue and the pathology image. As reported in previous work [32], there is usually a surface mismatch between the pathology and the fresh tissue THz image, as can be clearly seen in rat tumor #9- section 2. The primary reason for this mismatch is due to tissue deformation that occurs during the histopathology process. Almost ~ 100 µm thick tissue section is usually removed during the histopathology process to obtain a flat surface cut for the H&E stained slide. The mismatch and deformation in the imaging surface lead to a mismatch in the image between THz and pathology. Additionally, during the histopathology process, the tissue sometimes gets unfold and laid down at the bottom surface of the tumor. This also introduces ambiguity when correlating fresh tissue THz images with the pathology image. This observation is consistent with our previous mice tumor models [14, 15].

THz imaging and classification results were obtained for the ENU-tumors in rats and the mice models previously published, such as the xenograft [12-14] and the MMTV PyMT transgenic [15]. The difference observed in the results between these animal models was based on various factors, like the tumor induction process, the presence of healthy breast tissue at the tumor's margin, the tissue types in the tumor, and the tissue response to the THz pulse. A small amount of fibrous tissue was exhibited in transgenic mouse tumors, but that fibrous tissue was cancer induced tissue and not pre-existing. The results also showed that the best classification was achieved using

the EM technique, except for the transgenic mouse tumor, consistent with the classification of human breast cancer tumors reported in [29]. Furthermore, the obtained results showed that the EM classification of cancer in freshly excised tumors seems to be underpredicted by showing more false negatives than false positives.

The future work focuses on implementing machine learning and deep learning algorithms on THz imaging to perform better cancer classification and better assessment of tumor margins. Machine learning, as known, requires establishing a large database of tumor tissues. The use of ENU-tumor in rats has shown a potential to provide an adequate amount of data instead of relying on human breast tumors. Furthermore, a spectroscopy procedure in the reflection mode will be conducted to extract the refractive index and absorption coefficient of the xenograft, transgenic, and rat tumor models and compare with human breast tumors.

Disclosures

The authors declare that they have no conflict of interest.

Acknowledgments

This work was funded by the National Institutes of Health Award No. R15CA208798. It was also funded in part by the National Science Foundation (NSF) Award No. 1408007. Funding for the pulsed THz system was obtained through NSF/MRI Award No. 1228958. We also acknowledge the collaboration with Oklahoma Animal Disease Diagnostic Laboratory at the Oklahoma State University for conducting the histopathology procedure on all the tissues handled in this work. The Authors also acknowledge the use of the Histopathology Lab in the Biomedical Engineering Department at the University of Arkansas.

References

1. K. Okada, K. Serita, Q. Cassar, H. Murakami, G. MacGrogan, J-P. Guillet, P. Mounaix, and M. Tonouchi, "Terahertz near-field microscopy of ductal carcinoma *in situ* (DCIS) of the breast," *Journal of Physics: Photonics*, vol. 2, no. 4, pp. 044008, 2020.

2. Q. Sun, Y. He, K. Liu, S. Fan, E. P. J. Parrott, and E. Pickwell-MacPherson, "Recent advances in terahertz technology for biomedical applications," *Quantitative Imaging in Medicine and Surgery*, vol. 7, no. 3, pp. 345-355, 2017.

3. A. J. Fitzgerald, S. Pinder, A. D. Purushotham, P. O'Kelly, et al., "Classification of terahertz-pulsed imaging data from excised breast tissue," *Journal of Biomedical Optics*, vol. 17, no. 1, pp. 016005, 2012.

4. T. Bowman, N. Vohra, K. Bailey, and M. El-Shenawee, "Terahertz tomographic imaging of freshly excised human breast tissues," *Journal of Medical Imaging*, vol. 6, no. 2, pp. 023501, 2019.

5. B. S. Peter, S. Yngvesson, P. Siqueira, P. Kelly, A. Khan, S. Glick, and A. Karellas, "Development and testing of a single frequency terahertz imaging system for breast cancer detection," *IEEE Journal of Biomedical and Health Informatics*, vol. 17, no. 4, pp. 785-97, 2013.

6. S. Yamaguchi, Y. Fukushi, O. Kubota, T. Itsuji, T. Ouchi, and S. Yamamoto, "Brain tumor imaging of rat fresh tissue using terahertz spectroscopy," *Scientific Reports*, vol. 6, no. 1, pp. 30124, 2016.

7. H. Zuhayri, A. I. Knyazkova, V. V. Nikolaev, A. V. Borisov, Yu. V. Kistenev, O. A. Zakharova, P. A. Dyachenko, and V. V. Tuchin, "Study of wound healing by terahertz spectroscopy," *Proc. SPIE 11582, Fourth International Conference on Terahertz and Microwave Radiation: Generation, Detection, and Application*, Tomsk, Russian Federation, 115821E, 2020.

8. S. Sy, S. Huang, Y-X. Wang, J. Yu, A. T. Ahuja, Y-T. Zhang, and E. Pickwell-MacPherson, "Terahertz spectroscopy of liver cirrhosis: investigating the origin of contrast," *Physics in Medicine and Biology*, vol. 55, no. 24, pp. 7587-96, 2010.

9. Y. C. Sim, J. Y. Park, K-M. Ahn, C. Park, and J-H. Son, "Terahertz imaging of excised oral cancer at frozen temperature," *Biomedical optics express*, vol. 4, no. 8, pp. 1413-21, 2013.

10. F. Wahaia, G. Valusis, L. M. Bernardo, A. Almeida, J. A. Moreira, P. C. Lopes, J. Macutkevic, I. Kasalynas, D. Seliuta, R. Adomavicius, R. Henrique, and M. Lopes, "Detection of colon cancer by terahertz techniques," *Journal of Molecular Structure*, vol. 1006, no. 1, pp. 77-82, 2011.

11. H. Chen, T-H. Chen, T-F. Tseng, J-T. Lu, C-C. Kuo, S-C. Fu, W-J. Lee, Y-F. Tsai, Y-Y. Huang, E. Y. Chuang, Y-J. Hwang, and C-K. Sun, "High-sensitivity in vivo THz transmission

imaging of early human breast cancer in a subcutaneous xenograft mouse model," *Opt. Express*, vol. 19, no. 22, pp.21552-62, 2011.

12. T. Bowman, T. Chavez, K. Khan, J. Wu, A. Chakraborty, N. Rajaram, K. Bailey, and M. El-Shenawee, "Pulsed terahertz imaging of breast cancer in freshly excised murine tumors," *J. Biomed. Opt.*, vol. 23, no. 2, pp. 026004, 2018.

13. T. Chavez, T. Bowman, J. Wu, K. Bailey, and M. El-Shenawee, "Assessment of terahertz imaging for excised breast cancer tumors with image morphing," *J. Infrared Milli. Terahz Waves*, vol. 39, no. 12, 1283–1302, 2018.

14. T. Chavez, T. Bowman, J. Wu, K. Bailey, and M. El-Shenawee, "Cancer classification of freshly excised murine tumors with ordered orthogonal projection," *Proc. 2019 IEEE International Symposium on Antennas and Propagation and USNC-URSI Radio Science Meeting*, Atlanta, GA, USA, pp. 525-526, *2019*.

15. N. Vohra, T. Bowman, P. M. Diaz, N. Rajaram, K. Bailey, and M. El-Shenawee, "Pulsed terahertz reflection imaging of tumors in a spontaneous model of breast cancer," *Biomed. Phys. & Engg. Express*, vol. 4, no. 6, pp. 065025, 2018.

16. C. T. Guy, R. D. Cardiff, and W. J. Muller, "Induction of mammary tumors by expression of polyomavirus middle T oncogene: a transgenic mouse model for metastatic disease," *Molecular and Cellular Biology*, vol. 12, no. 3, pp. 954-61, 1992.

17. E. Y. Lin, J. G. Jones, P. Li, L. Zhu, K. D. Whitney, W. J. Muller, and J. W. Pollard, "Progression to malignancy in the polyoma middle T oncoprotein mouse breast cancer model provides a reliable model for human diseases," *The American Journal of Pathology*, vol. 163, no. 5, pp. 2113-26, 2003.

18. T. C. Bowman, M. El-Shenawee, and L.K. Campbell. "Terahertz imaging of excised breast tumor tissue on paraffin sections." *IEEE Trans. on Ant. and Propag*., vol. 63, no. 5, pp. 2088-2097, 2015.

19. T. Bowman, M. El-Shenawee, and L. K. Campbell, "Terahertz transmission vs reflection imaging and model-based characterization for excised breast carcinomas," *Biomed. Opt. Express*, vol. 7, no. 9, pp. 3756-83, 2016.

20. T. Bowman, Y. Wu, J. Gauch, L. K. Campbell, and M. El-Shenawee, "Terahertz imaging of three-dimensional dehydrated breast cancer tumors," *J. Infrared Milli. Terahz Waves*, vol. 38, no. 6, pp. 766-786, 2017.

21. N. Vohra, T. Bowman, K. Bailey, and M. El-Shenawee, "Terahertz imaging and characterization protocol for freshly excised breast cancer tumors," *J. Vis. Exp. issue*. 158, pp. e61007, 2020.

22. K. Almholt, K. A. Green, A. Juncker-Jensen, B. S. Nielsen, L. R. Lund, and J. Rømer, "Extracellular proteolysis in transgenic mouse models of breast cancer," *Journal of Mammary Gland Biology and Neoplasia*, vol. 12, no. 1, pp. 83-97, 2007.

23. G. Stoica, A. Koestner, and C. Capen, "Neoplasms induced with high single doses of N-ethyl-N-nitrosourea in 30-day-old Sprague-Dawley rats, with special emphasis on mammary neoplasia," *Anticancer research*, vol. 4, no. 1-2, pp. 5-12, 1984.

24. P. Swann and P. Magee, "Nitrosamine-induced carcinogenesis. The alkylation of N-7 of guanine of nucleic acids of the rat by diethylnitrosamine, N-ethyl-N-nitrosourea and ethyl methanesulphonate," *Biochemical Journal*, vol. 125, no. 3, pp. 841-7, 1971.

25. G. Stoica, A. Koestner, and C. Capen, "Characterization of N-ethyl-N-nitrosourea--induced mammary tumors in the rat," *The American journal of pathology*, vol. 110, no. 2, pp. 161, 1983.

26. K. Turetschek, T. P. Roberts, E. Floyd, A. Preda, V. Novikov, D. M. Shames, W. O. Carter, and R. C. Brasch, "Tumor microvascular characterization using ultrasmall superparamagnetic iron oxide particles (USPIO) in an experimental breast cancer model," *J. Magn. Reson. Imaging*, vol. 13 no. 6, pp. 882-8, 2001.

27. W. Li, R. B. Calder, J. C. Mar, and J. Vijg, "Single-cell transcriptogenomics reveals transcriptional exclusion of ENU-mutated alleles," *Mutation Research/Fundamental and Molecular Mechanisms of Mutagenesis*, vol. 772, pp. 55-62, 2015.

28. A. Nazmeen and S. Maiti, "Oxidant stress induction and signalling in xenografted (human breast cancer-tissues) plus estradiol treated or N-ethyl-N-nitrosourea treated female rats via altered estrogen sulfotransferase (rSULT1E1) expressions and SOD1/catalase regulations," *Molecular biology reports*, vol. 45, no. 6, pp. 2571-84, 2018.

29. T. Chavez, N. Vohra, J. Wu, K. Bailey and M. El-Shenawee, "Breast cancer detection with low-dimensional ordered orthogonal projection in terahertz imaging," *IEEE Transactions on Terahertz Science and Technology*, vol. 10, no. 2, pp. 176-189, 2020.

30. A. P. Salinger, and M. J. Justice MJ, "Mouse mutagenesis using N-ethyl-N-nitrosourea (ENU)," *CSH Protoc.* vol. 3, no. 4, Apr 2008.

31. S. Fan, B. Ung, E.P.J. Parrott, and E. Pickwell-MacPherson, "Gelatin embedding: a novel way to preserve biological samples for terahertz imaging and spectroscopy," *Physics in Medicine and Biology*, vol. 60, no. 7, pp. 2703-2713, 2015.

32. M. El-Shenawee, N. Vohra, T. Bowman, K. Bailey, "Cancer detection in excised breast tumors using terahertz imaging and spectroscopy," *Biomedical Spectroscopy and Imaging*, vol. 8, no. 1-2, pp. 1-9, 2019.

33. S. Ragothaman, S. Narasimhan, M. Basavaraj, and R. Dewar, "Unsupervised segmentation of cervical cell images using gaussian mixture model," in *Proceedings of the IEEE Conference on Computer Vision and Pattern Recognition (CVPR) Workshops*, pp. 70-75, 2016.

34. J. Friedman, T. Hastie, and R. Tibshirani, *The Elements of Statistical Learning* (Springer Series in Statistics), vol. 1. New York, NY, USA: Springer, 2001.

35. F. Wahaia, I. Kašalynas, L. Minkevičius, C. C. Silva, A. Urbanowicz, and G. Valušis, "Terahertz spectroscopy and imaging for gastric cancer diagnosis," *Journal of Spectral Imaging*, vol. 9, no. 1, pp. a2, 2020.

36. S. Guha and A. R. Lamichhane, "Document classification after dimension reduction through a modified Gram-Schmidt process," *Wireless Networks and Computational Intelligence*, K. R. Venugopal and L. M. Patnaik, Eds. Berlin, Germany: Springer, pp. 236–243, 2012.

37. X. Zhang, J. Bolton, and P. Gader, "A new learning method for continuous hidden Markov models for subsurface landmine detection in ground penetrating radar," *IEEE J. Sel. Topics Appl. Earth Observ. Remote Sens*., vol. 7, no. 3, pp. 813–819, 2014.

38. Pablo d'Angelo, "Hugin – Panorama photo stitcher." http://hugin.sourceforge.net/. Accessed: 7-1-2017.

Appendix : Microscopic Imaging and Image Analysis

The analysis of each rat mammary tumor is performed via microscopic imaging of the H&E-stained tissue slide (Fig. 8a). The first step in this process is to construct the low power microscopic image of the tissue slide. This is achieved by taking ~ 10-15 subsection images of the H&E slide at 6.7x magnification, as shown in Fig. 8b. The size of each sub-image obtained at 6.7x magnification is 3.28 × 3.28 mm. The images are taken such that every two adjacent subsection images have a common region between them. These images are then uploaded in open-source software (Hugin-Panorama Stitcher [38]). To map the common regions among all images, one image is taken as a reference image and is compared one on one with other images. For example, in Fig. 8c, image #1 is taken as a reference image, and it is further compared with all other images. The common regions between the reference image and the other images are marked as different colored boxes in Fig. 8c. Every image is made a reference image, and this mapping process is repeated for all images. Upon completion of the common region mapping process, the software then compiles the stitching of the images to provide the complete pathology image of the tissue at 6.7x magnification, as shown in Fig. 8d. To assess the tissue, few regions on the low power image are selected, for which 100x magnification images are obtained to have the cellular level

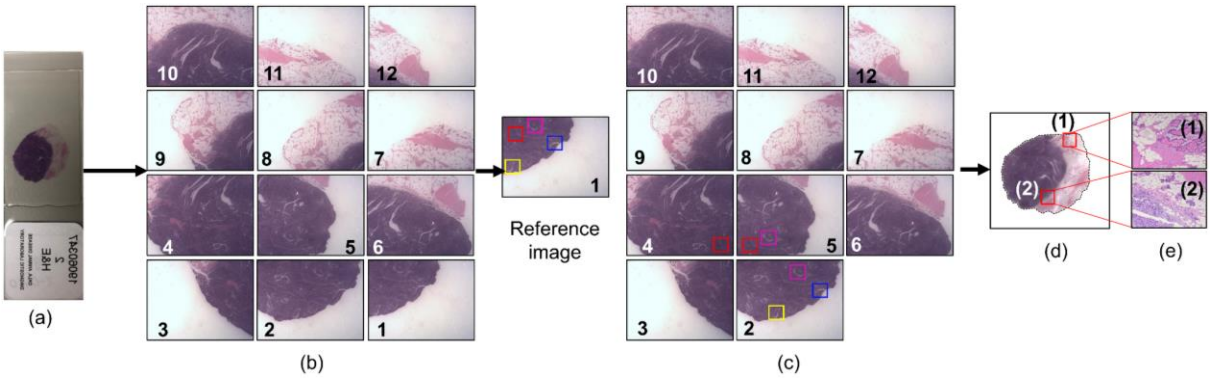

Fig. 8. Stitching microscopic images of mammary tumor from rat # 1. (a) H&E-stained tissue slide of rat tumor #1- section 2, (b) Low power microscopic images of the slide in (a) at 6.7x magnification, (c) compiled image in the software after mapping of common points between all images in (b), (d) Stitched pathology image, and (e) High power images obtained at 100x magnification for the tissue regions marked (1) and (2) in (d).

information of the selected region. For example, at the regions marked (1) and (2) in Fig. 8d, the high-power images are presented in Fig. 8e. The size of each high-power image obtained at 100x magnification is 0.22 × 0.22 mm. Several such images are taken that covers most of the tissue regions to be assessed.

CHAPTER 5

K- and W-Band Free-Space Characterizations of Highly Conductive Radar Absorbing Materials

Abstract

This work presents a characterization technique of highly conductive material in the K- and W-bands. The transmission line theory model is modified to adapt to the phase challenges observed in the measured S-parameters at high frequency. The S-parameters measurements are obtained using the nondestructive focused beam free-space system connected with the network analyzer and the millimeter-wave frequency extenders. The system provides measurements in a frequency range from 5.8 to 110 GHz, and it includes focused beam horn lens antennas to minimize sample edge reflection. The thru-reflect-line (TRL) calibration and the time-gated feature of the network analyzer are used. Good agreement between the measured and calculated S-parameters in the transmission mode is achieved using the extraction algorithm. The measured S-parameters are further used to obtain the electromagnetic shield effectiveness parameters and the percentage of power absorbed in the material. In addition, the return loss of the metal-backed material is calculated using the extracted permittivity to obtain the maximum absorption at the desired frequencies.

1. Introduction

With the inclusion of radar systems in the automotive industry, the interest to manufacture radar absorbing materials (RAMs) has increased in recent years. Newly introduced car models are equipped with radar-based advanced driver assistance systems (ADAS), such as collision warning

and collision avoidance (CW/CA), adaptive cruise control (ACC), assisted lane change, collision mitigation braking (CMS), and automated parking assist (APS), which provides high volume production with low-cost potential [1]. The radar sensors for these advanced systems are primarily deployed to function in the 24–26-GHz (short-range) and 76–77-GHz (long-range) allocated frequency bands [2]. The sensor at 77 GHz is typically much smaller, reducing the volume- and weight-related costs [3]. In addition, the long-range radar (LRR) systems at 77 GHz have shown improvement in many aspects from the short-range radars (SRRs) and mid-range radars (MRRs) [4], [5]. However, the deployment of ADAS systems has led to an increase in the number of automotive radar sensors operating simultaneously in a compact space. This results in signal interference that can lead to a reduced signal to noise ratio or ghost targets [6]. Furthermore, the coupling between transmit and receive antennas and the reflections from the adjacent metal structures of the vehicle can cause electromagnetic interference (EMI) in the automotive radar system. Engineering and characterization of high-frequency RAMs have been investigated in the literature for years [7], [8]. In addition, the shielding from the EM waves depends on the critical properties of the engineered composite materials [9]–[11]. Therefore, the electromagnetic characterization of the RAM material versus frequency is of significant importance, i.e., obtaining the complex electric permittivity (ε) and complex magnetic permeability (μ). The literature is rich with reports on the aspect of material characterization [12]–[43]. These materials were characterized as lossy or low-loss materials, where a variety of extraction methods based on the measured S-parameters were reported [12]–[43]. In this work, we use the free-space characterization technique to measure the S-parameters with thru-reflect-line (TRL) as the calibration methods. While the electromagnetic characterization of lossless and low-to-moderate lossy materials is well-established in the literature, we focus here on characterizing highly

conductive, inhomogeneous carbon-based materials in the K- and W-bands for the SRR and LRR radar systems, respectively. For example, among the samples handled in this work, sample P1 validates the success of the presented iterative extraction method where the obtained $\varepsilon = \sim 6$ in the K-band and ~ 4 in the W-band. Sample P2 demonstrates its potential use in the automotive industry as a radar-absorbing material where the absorption dip in the metal-backed measurements occurred in the K-band at 24 GHz after changing the thickness from 3.33 to 2.704 mm. Finally, sample P3 is different from the other two samples, demonstrating a very high-conductive material with ε values of ~ 100 and ~ 50 in the K- and W-bands, respectively. The proposed optimization technique, to find the initial guess values of the unknown relative permittivity, to be used in the extraction method highlights the novelty of this work. Our developed extraction algorithm is based on the transmission line theory [45], the iterative optimization algorithm [46], the modification due to configuration inhomogeneity in the W-band [15], and the inhomogeneity observation in 3-D metamaterial characterization, as reported in [48]. The proposed method provides the correct extraction of the relative permittivity of highly conductive samples measured in both the K- and W-bands. In addition, the extracted complex permittivity is further used to calculate the metalbacked return loss at several estimated sample thicknesses to obtain the maximum absorption at 24 and 77 GHz for use in the SRR and LRR systems, respectively. We present the percentage of power absorbed and the shielding effectiveness (SE) of materials, calculated based on the measured S-parameters. To the best of our knowledge, this is the first time that this extraction method has been investigated for microwave and millimeter-wave characterizations of highly conductive RAM samples measured using the free-space method. A total of 51 RAM samples were characterized under a nondisclosure agreement. Preliminary results to validate the method with commercial RAM materials were reported in our conference papers [28], [49], where materials of

1- and 2-mm thicknesses were purchased from the ARC Technology Inc. The free-space system is described in Section 2, the TRL calibration in Section 3, the model formulations in Section 4, the experimental results in Section 5, and the conclusion in Section 6. The Appendix describes the time gating feature used in the measurements, in addition to presenting the 3-dB beamwidth of the system in the *K*- and *W*-bands.

2. Free-Space System Setup

The microwave and millimeter-wave free-space measurement system is sketched in Fig. 1. It is composed of transmitting and receiving conical lens horn antennas with bandwidth from 5.8 to 110 GHz, a sample holder, an Agilent PNA E8361C network analyzer, an N5260A millimeter-wave controller, and two millimeter-wave frequency extenders. The antennas and the sample holder are mounted on a positioning scanner fixed on a large aluminum table in the XZ plane. This positioning system provides four degrees of freedom for the antenna movement in the X, Z, elevation angle (theta), and azimuth angle (phi) directions with a precision of ±2 μm [39], [40]. The sample holder stage provides motion in the Y -direction only. In order to focus the antenna beam on the sample center, two equal planoconvex dielectric lenses are mounted back-to-back in the conical horn antenna. The distance between the two antennas is ∼61 cm, and the focal distance to the diameter ratio of the lens is unity, with the lens's diameter equal to ∼30.5 cm. Thus, the dielectric lens focuses the beam incident on a sample at a specific frequency to a footprint of diameter approximately one wavelength [39]. The 3-dB beamwidths in the K- and W-bands are ∼1.2 cm and 4 mm, respectively (see Fig. 11). A custom-made sample holder is placed at the common focal plane of both antennas. It holds the sample under test between the two antennas such that the focal point of port 1 antenna is at the front face of the sample and that of port 2 antenna is at the back face of the sample. The sample holder is made of acrylic material and can

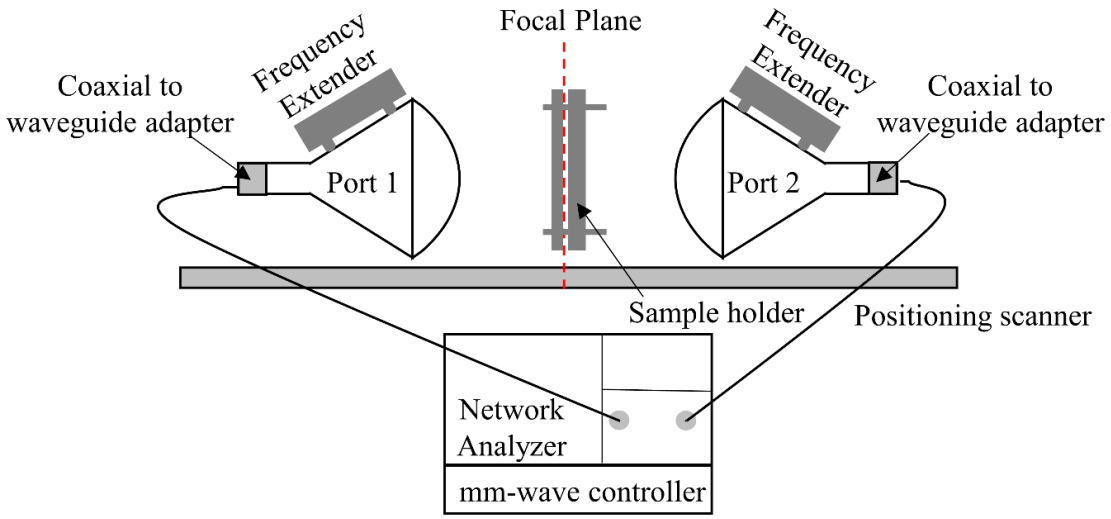

Fig. 1. Microwave and millimeter wave free-space measurement system.

hold the samples of size 6 × 6 and 12 × 12. The PNA E8361C network analyzer provides frequencies from 10 MHz to 67 GHz using 1.85-mm female coaxial cables from the network analyzer to the rest of the system. A coaxial to waveguide adapter is used to feed the antennas. These adapters are designed for the specific frequency ranges at which only the TE10 dominant mode is excited [33]. A total of eight pairs of the coaxial to waveguide adapters cover the frequency range from 5.8 to 110 GHz. In this work, the coaxial to waveguide adapters of the K-band (1.85-mm female connector) and the W-band (1-mm female connector), purchased from Keysight Technologies (W281C for the W-band and K281C for the K-band), are used. For the frequency bands up to 67 GHz, the horn antennas are directly connected to the network analyzer, whereas, for the frequency bands higher than 67 GHz, the horn antennas are connected to the millimeter-wave frequency extenders, which provides frequencies ranging from 67 to 110 GHz. The same conical horn lens antennas can be used for the entire range from 5.8 to 110 GHz. However, the appropriate coaxial to waveguide adapter that connects the network analyzer to the horn antenna is replaced for each desired bandwidth.

3. Free-Space Calibration and Measurement Procedures

3.1. System Calibration

The electromagnetic characterization of materials depends on the correct measurement of its complex S-parameters. To account for measurement errors in cables and network analyzer, a calibration procedure is needed. Among many well-known two-port calibration techniques [35],

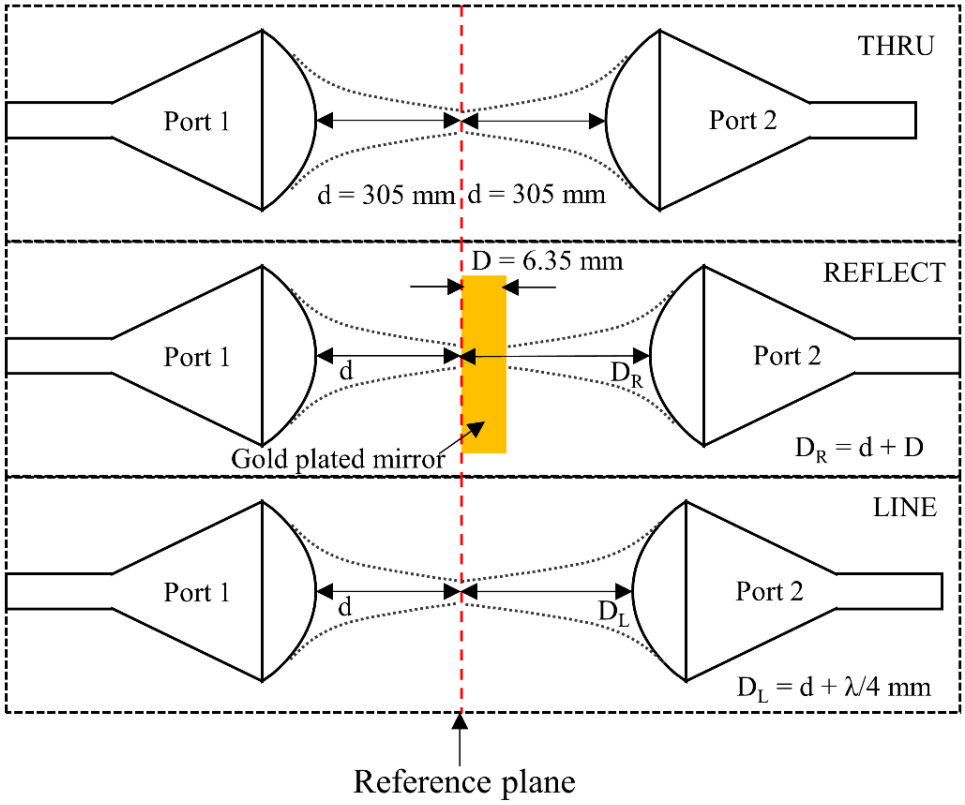

Fig. 2. TRL calibration procedure for free-space measurement system.

[38], [44], the TRL is considered the most appropriate technique for the free-space measurements [15], [28], [39]. The calibration steps are summarized in the following (see Fig. 2).

1) THRU standard in the TRL calibration is implemented by keeping both port 1 and port 2 antennas at their home positions and taking the measurements through the air. Here, the incident beams from both antennas are focused on the reference plane marked as the red dotted line in Fig.

2. This selected reference plane is the common focal plane of both antennas with a focal distance of ~305 mm, as shown in the figure.

2) REFLECT standard is implemented by placing a gold plated plate (also known as the gold-plated mirror) of thickness D = 6.35 mm in the sample holder. The mirror in the sample holder is placed at the common focal plane of the two antennas. Thus, the golden mirror side facing port 1 antenna is aligned with the reference plane, i.e., the incident beam from the port 1 antenna is focused on the air–gold mirror interface. However, due to the thickness of the gold mirror, port 2 antenna is moved back by a distance DR = d + D from the reference plane, and the measurement of the reflect standard is recorded.

3) LINE standard is implemented by removing the gold mirror from the sample holder and positioning port 2 antenna at a distance of DL = d + λ/4 from the reference plane. Here, λ/4 distance is calculated at the mid-frequency band, and the measurement through the air is recorded.

In order to verify the correctness of the calibration, S_{11} and S_{22} of a gold-plated plate are measured. The measurement is obtained by moving the port 2 antenna back by the distance DR = d + D from the reference plane, as described in step 2 of the TRL calibration. The threshold of the S_{11} and S_{22} magnitudes should be within ±0.1 dB, and the phase should be within 2° from ±180°. If these conditions are not achieved, the calibration is repeated.

3.2. Free-Space Measurements

In this work, two types of measurements are conducted: transmission mode and metal-backed reflection mode. As known, the measurements are sensitive to the thickness accuracy of the samples. Here, the sample thickness is measured at ten different points on the sample, and their average ($D = D_{ave}$) is considered the sample thickness. The measurements of ten points are acquired using the Mitutoyo Digimatic micrometer mounted on a flat granite stand. The sample is placed in

the holder, while the incident beam from port 2 antenna is focused on the air–sample interface by positioning it back by the distance (d+D) from the reference plane. The four complex S-parameters—S_{11}, S_{21}, S_{12}, and S_{22}—are measured and recorded using the network analyzer. For the metal-backed reflection mode, the sample is placed in the holder and backed with a gold-plated plate of 6.35-mm thickness. The front face of the sample is facing port 1 antenna, aligning with the reference plane, and only the S_{11} parameter is measured. All results of this work are obtained using the time-gated feature of the network analyzer (see the Appendix for details).

4. Extraction Method

4.1. Transmission Line Model

The concept of the extraction method to obtain the complex relative permittivity is based on the transmission line theory [45], [46]. However, our material samples have an unusual level of inhomogeneity and conductivity that necessitated additional work to accurately extract the complex relative permittivity $\widehat{\varepsilon_r} = \varepsilon' - j\varepsilon''$ with $\varepsilon'' = \sigma/\omega\varepsilon_o$, where σ is the conductivity of the material, ω is the angular frequency of the incident beam, and ε_o is the free-space permittivity. The reflection coefficient and transmission coefficients are [45]:

$$\Gamma = \frac{Z_S - Z_o}{Z_S + Z_o} = \frac{\sqrt{\frac{\widehat{\mu_r}}{\widehat{\varepsilon_r}}} - 1}{\sqrt{\frac{\widehat{\mu_r}}{\widehat{\varepsilon_r}}} + 1}, \qquad T = e^{-j\omega\sqrt{\varepsilon^*\mu^*}\,D} \tag{1}$$

where Z_o is the characteristic impedance of air, Z_S is the characteristic impedance of the material, $\varepsilon^* = \varepsilon_o\widehat{\varepsilon_r}$, and D is the thickness of the sample under test. For nonmagnetic materials, the magnetic permeability $\widehat{\mu_r} = 1$ and $\mu^* = \mu_o$.

The extraction method reported in [46] is based on iteratively minimizing error functions between the S-parameters measurements and calculations in each iteration. However, the

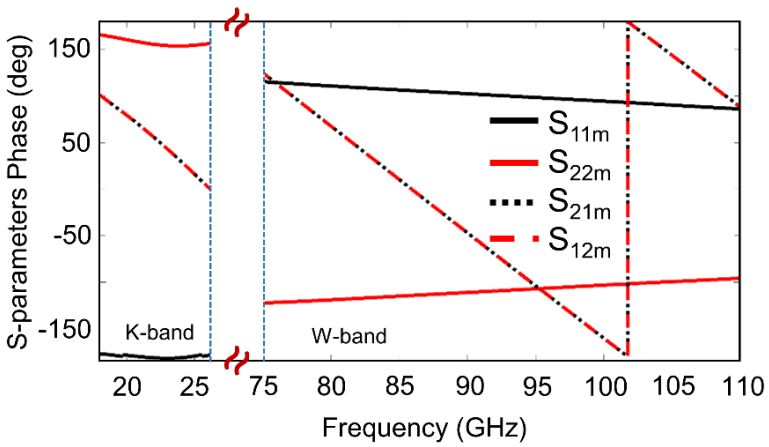

Fig. 3. The measured S-parameters phase of sample P1 in *K*- and *W*-band.

literature reported that this method has some challenges in inhomogeneous configurations [15], [48]. In [15], the work in the *W*-band reported inhomogeneity in the configuration due to the antennas' movement, while the tested samples were lossless or of low loss homogeneous materials. In [48], the work reported inhomogeneity due to the inclusion of the metamaterial cells. In both works, the iterative method was slightly modified. In this study, we observed that the samples are inhomogeneous in the *W*-band due to both factors, i.e. antennas' movements and mixing several ingredients at specific percentages (e.g. carbon, fiber, nylon, etc.). To be noted that the RAM industry aims at engineering highly absorbing radar materials by adding carbon based ingredients. The discussed challenge is demonstrated in Fig. 3 in the *W*-band and not the *K*-band. The phase of S_{11} is not equal to the phase of S_{22}, while the phase of S_{21} and S_{12} are equal. This phase difference prohibits the minimization of the error functions between measured and calculated S-parameters to provide accurate values of the extracted permittivity. The magnitude of the measured S-parameters is almost the same with some small differences due to measurements accuracy. As a result, we modified the model to combine the methods reported in [45], [46], and [15] in the *W*-band while keeping the same model of [46] in the *K*-band.

Thus, the novelty of this work lies in the proposed optimization technique that demonstrates the significance of the initial values of the unknown permittivity for such highly conductive materials in both the *K*- and *W*-band. To find these initial guess values, the error functions to be minimized in the *K*-band are:

$$\mathrm{Fun}_1 = 10 * \log_{10}|S_{11m} - S_{11c}| \tag{2a}$$

$$\mathrm{Fun}_2 = 10 * \log_{10}|S_{21m} - S_{21c}| \tag{2b}$$

$$\mathrm{Fun}_3 = 10 * \log_{10}|S_{12m} - S_{12c}| \tag{2c}$$

$$\mathrm{Fun}_4 = 10 * \log_{10}|S_{22m} - S_{22c}| \tag{2d}$$

Where in the *W*-band, we minimize the following functions:

$$\mathrm{Fun}_1 = 10 * \log_{10}|S_{21m} - S_{21c}| \tag{3a}$$

$$\mathrm{Fun}_2 = 10 * \log_{10}|S_{12m} - S_{12c}| \tag{3b}$$

$$\mathrm{Fun}_3 = 10 * \log_{10}\big||S_{11m}| - |S_{11c}|\big| \tag{3c}$$

$$\mathrm{Fun}_4 = 10 * \log_{10}\,||S_{22m}| - |S_{22c}|| \tag{3d}$$

Where S_{11m}, S_{22m}, S_{21m}, and S_{12m} are the measured complex transmission parameter, $S_{11c} = \frac{\Gamma(1-T^2)}{1-\Gamma^2T^2}$, and $S_{21c} = \frac{T(1-\Gamma^2)}{1-\Gamma^2T^2}$ are the calculated complex parameters at each iteration in the minimization search using the equation in [46]. Theoretically, $S_{22c} = S_{11c}$ and $S_{12c} = S_{21c}$. Note that the error functions in equations (2a-d) and (3a-b) minimize both the amplitude and phase of the parameter, while the functions in equations (3c-d) minimize only the magnitude of the parameter.

4.2. Absorption in Transmission and Metal-Backed modes

The main interest of the RAM industry is to examine the absorption of the material in transmission and when the material covers a metallic target. In the transmission mode, the amount of power absorbed, reflected, and transmitted through the sample is obtained using the measured S-parameters as follows:

$$\frac{\text{Power reflected}}{\text{Power incident}} = |S_{11m}|^2, \tag{4a}$$

$$\frac{\text{Power transmitted}}{\text{Power incident}} = |S_{21m}|^2, \tag{4b}$$

$$\frac{\text{Power absorbed}}{\text{Power incident}} = 1 - |S_{11m}|^2 - |S_{21m}|^2 \tag{4c}$$

For the metal-backed reflection, the S_{11refc} is given by [13]:

$$S_{11refc} = \frac{\sqrt{\frac{\widehat{\mu_r}}{\widehat{\varepsilon_r}}}\tanh\left(j\omega\sqrt{\varepsilon^*\mu^*}D\right) - 1}{\sqrt{\frac{\widehat{\mu_r}}{\widehat{\varepsilon_r}}}\tanh\left(j\omega\sqrt{\varepsilon^*\mu^*}D\right) + 1} \tag{5}$$

Where D is the sample thickness and $\varepsilon^* = \varepsilon_o\widehat{\varepsilon_r}$, $\mu^* = \mu_o\widehat{\mu_r}$, and $\widehat{\mu_r} = 1$ for nonmagnetic material. The S_{11refc} is measured upon backing the sample with the gold mirror and is also calculated using the extracted complex permittivity $\widehat{\varepsilon_r}$.

4.3. Electromagnetic Shield Effectiveness

The electromagnetic shield effectiveness is defined by the ability of a material to attenuate the intensity of electromagnetic radiation to an adequate level desired based on the application. The total shield effectiveness SE is the summation of the reflection, absorption, and multiple internal reflection losses at the air-sample interface. When SE_A is ≥ 10dB, the multiple internal reflection is negligible, which is usually the case. Therefore, the total shield effectiveness SE is expressed by [47]:

$$SE = SE_A + SE_R \tag{6a}$$

where SE_A and SE_R are the absorption and reflection shielding, given as functions of the S-parameters by:

$$SE_A = -10\log_{10}\left(\frac{|S_{21m}|^2}{1-|S_{11m}|^2}\right) \tag{6b}$$

$$SE_R = -10\log_{10}(1-|S_{11m}|^2) \tag{6c}$$

The SE depends on the frequency of the excitation, the thickness of the sample, the material composite, and the fabrication and processing conditions [9].

5. Experimental Results

In this section, we present the results of three samples in both the K- and W-bands. While the developed method is applicable to magnetic and nonmagnetic materials, all samples presented here are assumed nonmagnetic, based on information from the manufacturer. The samples are referred to by P1, P2, and P3 and are made of highly conductive materials with an average thickness of around 3 mm. For each sample, the extracted complex relative permittivity, the magnitude validation of S-parameters (dB), and the return loss (dB) are presented versus frequency. The SE and the percentage of power absorbed for each sample are also presented in both the K- and W-bands.

5.1. Initial Guess

While, in the K-band, the initial guess in the iterative solver for the complex relative permittivity can start with (1 – j0), which is more involved in the W-band, the simplest method to select the initial guess of the material in the W-band is to use the values extracted at 26.5 GHz in

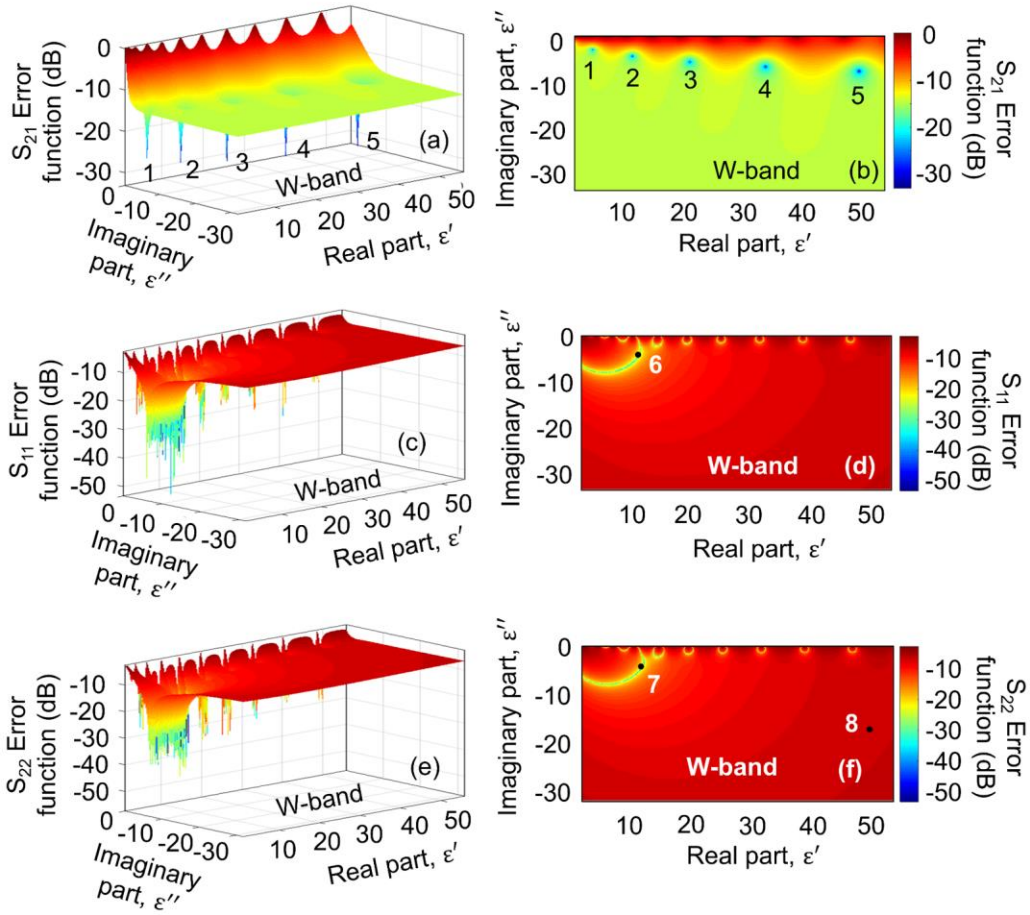

Fig. 4. The initial guess in the *W*-band for sample P1. (a) 3-D Error function showing the minimum error between $S_{21measured}$ and $S_{21calculated}$. (b) Top view of (a). (c) 3-D Error function graph showing minimum error between $|S_{11}|_{measured}$ and $|S_{11}|_{calculated}$. (d) Top view of (c). (e) 3-D Error function graph showing minimum error between $|S_{22}|_{measured}$ and $|S_{22}|_{calculated}$. (f) Top view of (e).

the K-band. Another method to select the initial guess in the W-band is to map the roots of error functions in (3) individually and select those that are close to each other. The initial guess is used in a line search using the MATLAB code, and the algorithm stops when a preassigned threshold error is achieved. In order to validate the extracted permittivity, the error between the calculated and measured S-parameters is obtained, and the results are selected based on the minimum error. In some cases, all initial guess values provide the same solutions. Fig. 4 demonstrates the map of the roots of (3a), (3c), and (3d) for sample P1. Table 1 lists various initial guess values used in the

line search of the W-band solution. The listed values of the initial guess converged to the same solution of the extracted permittivity that is shown in Fig. 5(a), except for a couple of initial guess points. For example, the first point marked as 1 with (ε' = 4.1, ε" = 2.8) gave a wrong validation when comparing the measured and calculated S-parameters with a difference of ∼25–30 dB in the

Table 1. Sample P1—Initial Guess Points Based On S_{21}, S_{11}, and S_{22} Error Functions

W-band			
Number	Initial Guess		Extracted Permittivity Solution
	ε′	**ε″**	
K-band	12.98	4.65	Same as Fig. 5a
1	4.1	2.8	Wrong S-parameter
2	11.1	4.1	Same as Fig. 5a
3	21.3	5.2	Same as Fig. 5a
4	34.7	6.2	Same as Fig. 5a
5	51.4	7.2	Same as Fig. 5a
6	11.1	4.1	Same as Fig. 5a
7	11.6	4.1	Same as Fig. 5a
8	52.8	18.9	Ambiguous

S_{21} parameter. The second point marked by 8 (ε' = 52.8, ε" =18.9) was a random point in the considered space, giving an ambiguous solution of the permittivity. This means that the values of the real and imaginary parts demonstrate jumps in a stepwise manner at certain frequencies similar to what was reported in [50] and [51]. Therefore, the solutions based on these two initial guesses were rejected, and the converged solution with the good S-parameter validations was selected.

5.2. Electrical Properties

The extracted permittivity of P1 sample is shown in Fig. 5(a); the validation of the S-parameters is shown in Fig. 5(b) for the K- and W-bands. The solid black line represents the real part, and the red solid line represents the imaginary part of the extracted permittivity in Fig. 5(a). The large values of ε across the K- and W-bands demonstrate the high conductivity of the material. The relative permittivity of P1 shows a decreasing trend in the K-band as the frequency increases,

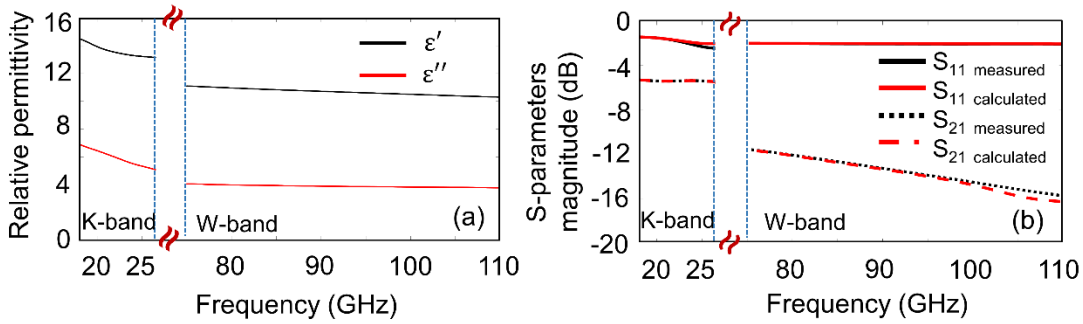

Fig. 5. (a) and (b) Results of sample P1 in K- and W-bands. (a) Relative permittivity plot showing real and imaginary parts ε' and ε", respectively. (b) Comparison between the measured and calculated S-parameters magnitudes.

where, in the W-band, it is almost constant versus frequency with an average value of 10.67 for ε' and that of 3.89 for the ε". The extracted relative permittivity of P1 in both K- and W-bands is further used to calculate the S-parameters, as shown in Fig. 5(b). A maximum difference observed between the magnitudes of calculated and measured S_{11} (red solid and black lines, respectively) is 0.51 dB and that between calculated and measured S_{21} (dashed red and black dotted line, respectively) is 0.001 dB in the K-band. On the other hand, in the W-band, the error is 0.026 and 0.8 dB between the calculated and measured S_{11} and S_{21}, respectively. This demonstrates a good validation of the extraction model for sample P1.

5.3. Return Loss for Metal-Backed Material

The return loss for sample P1 is obtained versus frequency in the K- and W-bands, as presented in Fig. 5(c) and (d), respectively. The red solid and black lines in Fig. 5(c) and (d) represent the measured and calculated return loss values obtained at the average thickness of the sample (3.153 mm). An approximate maximum error of the 1.0-dB difference between the calculated (red solid line) and measured return loss (solid black line) is observed at a 26.5-GHz frequency in Fig. 5(c), whereas, it is ~0.001 dB at 110.0 GHz in Fig. 5(d). More importantly, with the sample thickness of 3.153 mm, there was no observed resonance in the measured return loss at

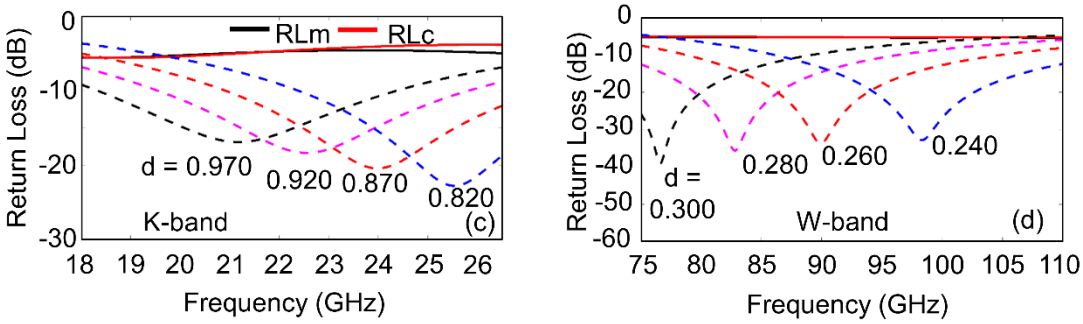

Fig. 5c-d. Return loss of metal-backed material of Sample P1. (c) Measured and calculated return loss for the metal backed reflection measurement at different thicknesses in *K*-band, (d) Measured and calculated return loss for the metal backed reflection measurement at different thicknesses in *W*-band.

any frequency in the K- or W-band. Upon using the extracted complex permittivity in (5) with different thicknesses, the sample can demonstrate resonance if made of different thicknesses. The calculated return loss at four other thicknesses is shown in Fig. 5(c) for the K-band and Fig. 5(d) for the W-band (see dotted colored lines). In the K-band figure, the black dotted, magenta, red, and blue lines in Fig. 5(c) represent return loss calculated at a thickness of 0.970, 0.920, 0.870, and 0.820 mm, respectively. Similarly, for the W-band, the black dotted, magenta, red, and blue lines in Fig. 5(d) represent the return loss calculated for 0.300, 0.280, 0.260, and 0.240 mm, respectively. In addition, the data in Table 2 show the frequency at which the maximum absorption occurs for each thickness and the bandwidth at −10 dB. The table indicates that the obtained bandwidth in the K-band is ~6 GHz at each thickness, whereas it is more than 20 GHz in the W-band. Furthermore, it can be observed from Fig. 5(c) and (d) and Table II that, for a small change in the sample thickness of ~50 μm, in the K-band and ~20 μm in the W-band, the resonance shifts by ~1.5 and ~5.0 GHz, respectively. Thus, to use the sample material as an absorber for radar systems, it is imperative to manufacture the sample at the correct thickness of the needed frequency. For example, in the automotive industry, the use of 24 GHz in short range and 77 GHz

in LRR detection units is commonplace with the advent of environment object detection technologies being deployed in all high-tech automobiles. To utilize sample P1 as an absorber in these SRR and LRR systems, it has to be manufactured precisely at a thickness equal to 0.870 and 0.3 mm, respectively.

Table 2. Calculated absorption values using new thickness shown in Figs. 5(c) and (d)

Number	K-band			W-band		
	Thickness (mm)	Max. Absorption frequency (GHz)	Bandwidth (GHz)	Thickness (mm)	Max. Absorption frequency (GHz)	Bandwidth (GHz)
1	0.970	21.15	6.05	0.300	77	22.39
2	0.920	22.56	6.27	0.280	82.83	23.78
3	0.870	24.0	6.42	0.260	89.94	25.99
4	0.820	25.55	6.53	0.240	98.32	28.46

The results of the second sample P2 are shown in Fig. 6. This sample has an average thickness of 3.33 mm. Similar to sample P1, the initial guess of the complex permittivity is selected using the solution of the K-band validated by selecting the initial guess based on the error functions of (3). The results are not shown here due to space limitations. The extracted results of the complex permittivity are shown in Fig. 6(a). The solid black line in Fig. 6(a) represents the real part of the permittivity, and the red solid line represents the imaginary part. The real part demonstrates an increasing trend until around 22 GHz and then shows an almost constant value of ~34 in the K-band. For the W-band, it shows an almost constant value with an average of 32.46 for ε' and that of 2.11 for ε".

In order to validate the permittivity solution, the S-parameters are calculated using the extracted permittivity values in the K- and W-bands and compared with measurement magnitudes. A maximum difference in S_{11} was observed to be 0.16 dB and in S_{21} to be 0.76 dB in the K-band, while it is 0.2 and 0.36 dB in the W-band, as shown in Fig. 6(b). The results demonstrate a good

validation of the extraction model in both K- and W-bands for this sample, consistent with sample P1. The metal-backed return loss (dB) is shown in Fig. 6(c) and (d), for the K- and W-bands, respectively. The red solid and black lines in Fig. 6(c) and (d) represent the measured and calculated return loss values obtained at the actual average sample thickness of 3.33 mm. Unlike other samples discussed earlier, the measured return loss of this sample (solid black line) indicates the maximum absorption of the signal at 19.42 GHz, as shown in Fig. 6(c). This sample demonstrates a narrow band absorber providing a bandwidth of ~600 MHz at 19.42 GHz. A shift of approximately 400 MHz from the measured maximum absorption is observed in the calculated return loss (red solid line) obtained at the same sample thickness (3.33 mm). This shift could be due to a slight change in the sample thickness when the measurements are performed. As described earlier, our method of taking the sample thickness is based on measuring the thickness at ten

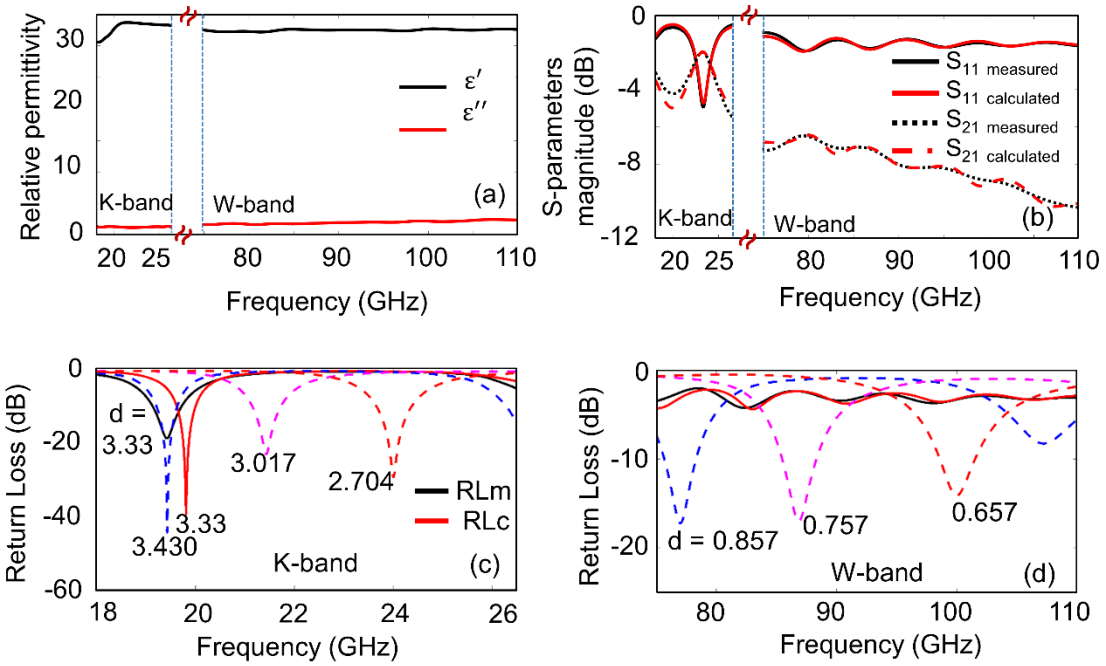

Fig. 6. Results for sample P2 in the *K*- and *W*-band. (a) The real and imaginary parts of permittivity, ε' and ε", respectively (b) Comparison between measured and calculated S-parameters magnitude. In Figs. 6c-d, the measured and calculated metal-backed return loss at different thicknesses (c) in *K*-band, and (d) *W*-band.

different points on the sample and averaging them. It is likely that, when the measurements are performed, the spot on the sample at which the beam hits has a slightly different thickness than the average thickness used in the algorithm. In addition, as observed earlier in this section, a slight change of ~50 μm in the thickness caused the resonance to shift significantly. To prove this, the

Table 3. Measured and calculated absorption at actual and new sample thickness shown in Figs. 6(c) and (d).

Number	K-band			W-band		
	Thickness (mm)	Max. Absorption frequency (GHz)	Bandwidth (GHz)	Thickness (mm)	Max. Absorption frequency (GHz)	Bandwidth (GHz)
Measured and calculated absorption at the actual sample thickness						
RLm	3.330	19.42	0.6	3.330	-	-
RLc	3.330	19.82	0.380	3.330	-	-
Calculated absorption using new thickness						
1	3.430	19.42	0.420	0.857	77	2.62
2	3.017	21.43	0.580	0.757	86.86	2.84
3	2.704	24.0	0.730	0.657	99.88	2.91

return loss for this sample is calculated at the sample thickness of 3.43 mm (a change of 0.1 mm), which shifted the maximum absorption back at the same 19.42-GHz frequency (blue dotted line) of the measured return loss, as shown in Fig. 6(c). The return loss is also calculated at the other two thicknesses− 3.017 and 2.704 mm, which displays the maximum absorption at 21.43 and 24 GHz, as shown in magenta dotted and red lines in Fig. 6(c), respectively. The return loss for sample P2 in the W-band is presented in Fig. 6(d). At high frequencies, multiple reflections are observed, as shown in the figure. However, the calculated metal-backed return loss (red solid) follows the same behavior as the measured one (solid black line), demonstrating a maximum difference of ~0.76 dB at 75 GHz. This validates the extraction method for this sample. In addition, in Fig. 6(d), the blue dotted, magenta, and red lines represent the metal-backed return loss calculated, using the extracted permittivity and sample thicknesses of 0.857, 0.757, and 0.657 mm, respectively. Table

3 lists the frequency of the maximum absorption at each of these thicknesses and the bandwidth obtained using the -10 dB threshold. To utilize sample P2 as an absorber in the SRR and LRR systems, it has to be manufactured precisely at a thickness equal to 2.704 and 0.857 mm, respectively.

The results of the third sample, P3, are shown in Fig. 7, where the average thickness of the sample is 3.373 mm. This sample represents the highest conductive material among all the 51 samples characterized in this project. Here, the error functions of (3a) and (3b) were modified to be similar to (3c) and (3d) where the phase minimization was removed and only the error in magnitudes was used. Here, even in the K-band, the initial guess is marked as 1 where (ε' = 1 and ε'' = 0), provided a negative value of the real part of $\hat{\varepsilon}_r$, as listed in Table 4. The same for the random initial guess is marked by 7 (ε' = 6 and ε'' = 10.3). All other initial guess values obtained from the error functions converged to the same solution that also provided good comparisons between the calculated and measured S-parameter magnitudes, as shown in Fig. 7. Here, the initial guess of the permittivity in the W-band is obtained from the solution in the K-band at 26.5 GHz.

The results of the extracted permittivity are shown in Fig. 7(a) for the K- and W-bands. The black solid line represents the real part, and the red solid line represents the imaginary part.

Table 4. Sample P3 – Initial guess points based on S_{21}, S_{11}, and S_{22} error functions.

K-band			
Number	Initial Guess		Extracted Permittivity Solution
1	$\boldsymbol{\varepsilon'}$	$\boldsymbol{\varepsilon''}$	
2	1	0	Negative $\boldsymbol{\varepsilon'}$: rejected
3	44.6	50.2	Same as Fig. 7a
4	288	93.4	Same as Fig. 7a
5	329	97	Same as Fig. 7a
6	483	113.6	Same as Fig. 7a
7	585	147	Same as Fig. 7a
8	6	10.3	Negative $\boldsymbol{\varepsilon'}$: rejected

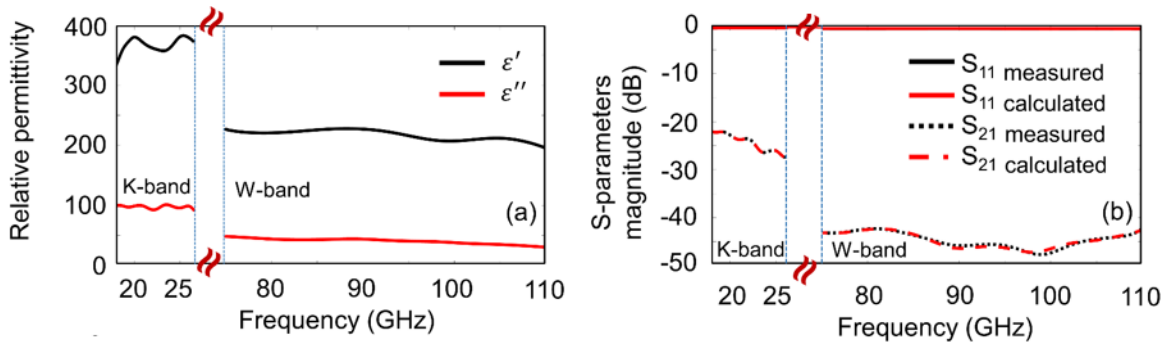

Fig. 7. Results of sample P3 in the *K*- and *W*-band, (a) The real and imaginary parts of the relative permittivity, ε' and ε", respectively, (b) Comparison between the measured and calculated S-parameters magnitudes.

The comparison between the measured and calculated S-parameters magnitudes is shown in Fig. 7(b) with the solid lines representing S_{11} and the dashed or dotted lines representing S_{21}. It is observed that the real and imaginary parts of the extracted permittivity in Fig. 7(a) are noticeably higher in the K-band compared with those in the W-band. This observation is consistent with samples P1 and P2 results but with less difference between the two bands. We also note wavy plots in the permittivity versus frequency consistent with the P2 sample results. This behavior could also be due to the multiple reflections in the sample. In Fig. 7(b), the sample P3 is highly reflective due to its high conductivity, demonstrated in the permittivity imaginary parts in Fig. 7(a). The magnitude of S_{11} is in the range between −1 and ~0 dB in the K- and W-bands, while that of S_{21} is between ~−20 and ~−30 dB in the K-band and between ~−40 and ~−50 dB in the W-band.

The maximum difference observed between the magnitudes of calculated and measured S_{11} and S_{21} is 0.01 dB in the K-band, as shown in Fig. 7(b), whereas it is 0.012 and 0.86 dB between the calculated and measured S_{11} and S_{21}, respectively, in the W-band. Even with almost no transmission through this sample, the difference between the measured and calculated S-parameters is less than 1 dB, proving the validity of this extraction model for highly conductive materials. For the metal-backed configuration, this sample proved to be unsuitable as a RAM. The

return loss results (not included) did not show absorption in the mm-range of sample thickness. However, it is possible to use this material as absorbing thin film covering metallic targets, where thicknesses of less than 50 μm were observed to provide absorption of fewer values ∼−12 dB at 110 GHz.

5.4. Absorption and Shield Effectiveness

The percentage of power absorbed in the transmission mode is obtained using (4c). A comparison between the three samples is shown in Fig. 8. Sample P1 demonstrates higher absorption values compared with that in samples P2 and P3. This behavior is consistent with the

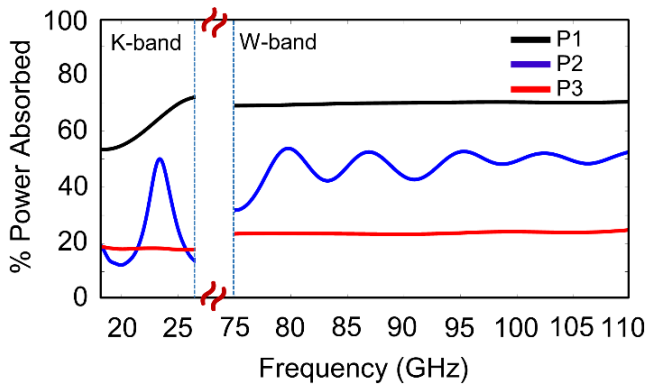

Fig. 8. The percentage power absorbed based on measured S-parameters in samples P1, P2, and P3 obtained in *K*- and *W*-band.

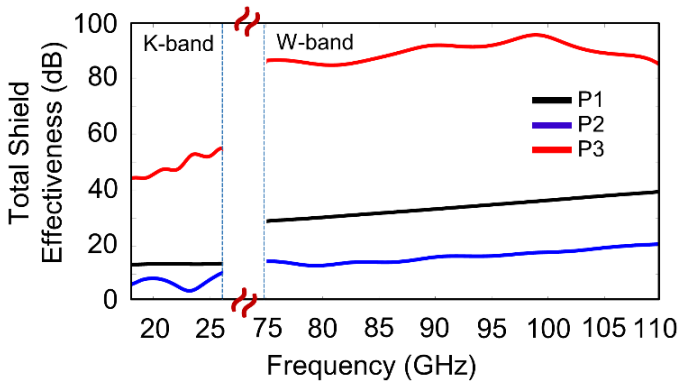

Fig. 9. The electromagnetic total shield effectiveness based on the measured S-parameters of samples P1, P2, and P3.

extracted permittivity of these materials. A comparison of the total SE of the three samples, obtained using (6a), is shown in Fig. 9. The value of SE (total SE) is the sum of SE_A (absorption SE) and SE_R (reflection SE). Due to space limitations, we omitted the results of SE_A and SE_R and presented only the SE values in Fig. 9. As observed in the results, the SE is higher in the W-band than in the K-band in all three samples. In addition, as the frequency increases, the SE increases, except for P3 in the W-band, where it shows wavy behavior versus frequency. P3 shows higher SE values than that of P1, followed by P2. Furthermore, a wavy behavior in the SE plots observed in samples P2 and P3 is consistent with their extracted permittivity and also with the literature [9] for carbon-based nanostructured polymeric materials. The work in [9] described such behavior as the irregular nature of the included conductive materials.

6. Conclusion

We presented the results of the free-space characterization method for three highly conductive nonhomogeneous carbon-based RAM samples. The TRL calibration was utilized here, and the measurements were conducted in the K- and W-bands. The developed method is based on an iterative optimization model to extract the complex permittivity of the engineered materials. The initial guess technique and the extraction algorithm that we presented in this article have successfully provided the correct relative permittivity of highly conductive samples (e.g., sample P3). The validation of the extracted permittivity was based on minimizing the error between the measured and calculated S-parameters. The S-parameters calculations were based on using the extracted complex permittivity in the S-parameters expressions of the transmission line model [45]. In all samples, the maximum error was less than 1 dB. Furthermore, a validation was demonstrated for the metal-backed samples based on a minimum error between the measured and calculated return loss. The phase difference between the S_{11} and S_{22} parameters in the

measurements using the TRL calibration was reported in the literature in the W-band [15] and the Ku-band [48]. We observed the same issue, particularly for the high-conductivity materials considered here. These phase discrepancies represented a challenge when using the original extraction methods in [45] and [46] as it has led to ambiguous solutions similar to those reported in [50] and [51] or to incorrect validation of the measured and calculated S-parameters, as discussed in Section 5. Here, we modified the extraction method by simultaneously minimizing the functions of the S-parameters based on their magnitude and also generating a pool of initial guesses based on the individual error functions. Otherwise, it would have been almost impossible for the W-band measurements to start the optimization algorithm with an initial guess as $\varepsilon' = 1$ and $\varepsilon'' = 0$ (similar to the K-band). Therefore, we adopted a similar technique to that reported in [15] to obtain the initial guess in the W-band, as presented in Fig. 4. The results also show that using metal-backed samples does not necessarily demonstrate resonances at the desired frequency. However, the extracted complex permittivity can be utilized to design the appropriate thickness of the sample in order to obtain the maximum resonance in the return loss at the desired frequency. In addition, the total SE and the percentage of power absorbed in the transmission mode were obtained to guide the selection of the appropriate material, in particular at 24 and 77 GHz, for the automotive radar application.

Acknowledgments

This work was funded in part through the GAP Chancellor's Innovation Fund under Award 003184-00001A and in part by the Department of Electrical Engineering at the University of Arkansas. The RAM samples were provided by a company under a nondisclosure agreement.

References

[1] Kyongsu Yi, Seung-Wuk Moon, In-Sik Lee, Jae-Yong Um, and Ilki Moon, “Design of full-range ACC with collision avoidance/mitigation braking,” *IFAC Proceedings Volumes*, vol. 40, no. 10, pp. 127-134, 2007.

[2] Z. Sun, G. Bebis, and R. Miller, “On-road vehicle detection: A review,” *IEEE Trans. Pattern Anal. Mach. Intell.*, vol. 28, no. 5, pp. 694–711, May 2006.

[3] J. Hasch, E. Topak, R. Schnabel, T. Zwick, R. Weigel, and C. Waldschmidt, "Millimeter-Wave technology for automotive radar sensors in the 77 GHz frequency band," in *IEEE Transactions on Microwave Theory and Techniques*, vol. 60, no. 3, pp. 845-860, 2012.

[4] M. Kim and S. Kim, "Design and fabrication of 77-GHz radar absorbing materials using frequency-selective surfaces for autonomous vehicles application," *IEEE Microwave and Wireless Components Letters*, vol. 29, no. 12, pp. 779-782, 2019.

[5] L. Maurer, G. Haider, and H. Knapp, "77 GHz SiGe based bipolar transceivers for automotive radar applications — An industrial perspective," 2011 *IEEE 9th International New Circuits and systems conference*, Bordeaux, 2011, pp. 257-260, 2011.

[6] M. Goppelt, H.-L. Blöcher, and W. Menzel, “Automotive radar Investigation of mutual interference mechanisms,” *Adv. Radio Sci.*, vol. 8, pp. 55–60, Sep. 2010.

[7] D. C. Schleher, *Electronic Warfare in the Information Age*, London: Artech House, 1999.

[8] S. A. Silva, J. J. Pereira, E. L. Nohara, and M. C. Rezende, “Electromagnetic behavior of microwave absorbing materials based on Ca hexaferrite modified with CoTi ions and doped with La,” *Journal of Aerospace Technology and Management*, vol. 1, no. 2, pp. 255-263, 2009.

[9] D. D. L. Chung, “Electromagnetic interference shielding effectiveness of carbon materials,” *Carbon*, vol. 39, no. 2, pp. 279-285, 2001.

[10] M. H. Al-Saleh, W. H. Saadeh, and U. Sundararaj, “EMI shielding effectiveness of carbon based nanostructured polymeric materials: A comparative study,” *Carbon*, vol. 60, no. 8, pp. 146-156, 2013.

[11] D. Balageas and P. Levesque “EMIR: A photothermal tool for electromagnetic phenomena characterization,” *Revue Generale de Thermique*, vol. 37, no. 9, pp. 725-739, 1998.

[12] V. V. Varadan, "Radar absorbing applications of metamaterials," *2007 IEEE Region 5 Technical Conference, Fayetteville, AR*, pp. 105-108, 2007.

[13] D. M. Pozar, “Microwave engineering,” Hoboken, NJ: Wiley, 2012.

[14] L. d. C. Folgueras, M. A. Alves, and M. C. Rezende, "Development, characterization and optimization of dielectric radar absorbent materials as flexible sheets for use at X-band,"

2007 SBMO/IEEE MTT-S International Microwave and Optoelectronics Conference, Brazil, pp. 488-491, 2007.

[15] D. Bourreau, A. Peden, and S. Le Maguer, "A Quasi-optical free-space measurement setup without time-domain gating for material characterization in the W-band," *IEEE Transactions on Instrumentation and Measurement*, vol. 55, no. 6, pp. 2022-2028, 2006.

[16] Y. Zhai, Y. Zhang, and W. Ren, "Electromagnetic characteristic and microwave absorbing performance of different carbon-based hydrogenated acrylonitrile–butadiene rubber composites," *Materials Chemistry and Physics*, vol. 133, no. 1, pp. 176-181, 2012.

[17] B. G. M. Helme, "Measurement of the microwave properties of materials," *IEE Colloquium on Industrial Uses of Microwaves*, London, UK, pp. 3/1-3/7, 1990.

[18] L. F. Chen, C. K. Ong, C. P. Neo, V. V. Varadan, and V. K. Varadan, Microwave electronics: Measurement and materials characterization, John Wiley & Sons, 2004.

[19] Von Hippel, A.R. Dielectric materials and applications; Artech House: Dedham, MA, USA, Vol. 2, 1954.

[20] J. Barker-Jarvis et al., "Dielectric characterization of low-loss materials—A comparison of techniques," *IEEE Trans. Dielectr. Electr. Insul*., vol. 5, no. 4, pp. 571–577, 1998.

[21] J. Obrzut, C. Emiroglu, O. Kirillov, Y. Yang, and R. E. Elmquist, "Surface conductance of graphene from non-contact resonant cavity," *Measurement*, vol. 87, pp. 146–151, Jun. 2016.

[22] C. L. Pournaropoulos and D. K. Misra, "The co-axial aperture electromagnetic sensor and its application in material characterization," *Measurement Science and Technology*, Vol. 8, no. 11, pp. 1191-1202, 1997.

[23] S. Mueller, A. Penirschke, C. Damm, P. Scheele, M. Wittek, C. Weil, and R. Jakoby, "Broad-band microwave characterization of liquid crystals using a temperature-controlled co-axial transmission line," in *IEEE Transactions on Microwave Theory and Techniques*, vol. 53, no. 6, pp. 1937-1945, 2005.

[24] N. Williams, V. K. Varadan, D. Ghodgaonkar, and V. V. Varadan, "Measurement of transmission and reflection of conductive lossy polymers at millimeter-waves frequencies*," IEEE Trans. Electromagn. Compat*., vol. 32, no. 3, pp. 236–240, 1990.

[25] S. Sahin, N. K. Nahar, and K. Sertel, "A simplified Nicolson–Ross–Weir method for material characterization using single-port measurements," in *IEEE Transactions on Terahertz Science and Technology*, vol. 10, no. 4, pp. 404-410, 2020.

[26] F. Costa, M. Borgese, M. Degiorgi, and A. Monorchio, "Electromagnetic characterization of materials by using transmission/reflection (T/R) devices," *Electronics*, vol. 6, no. 95, pp. 1-27, 2017.

[27] Z. Qamar, N. Aboserwal, and J. L. Salazar-Cerreno, "An accurate method for designing, characterizing, and testing a multi-layer radome for mm-wave applications," in *IEEE Access*, vol. 8, pp. 23041-23053, 2020.

[28] N. Vohra, L. R. Rodriguez-Aguilar, J. S. Batista, and M. El-Shenawee, "Free-space characterization of radar absorbing non-magnetic materials in the W-band," in *Proc. of ARFTG 2020*, San Antonio, TX, 26-29 Jan 2020.

[29] M. S. Hilario et al., "W-band complex permittivity measurements at high temperature using free-space methods," in *IEEE Transactions on Components, Packaging and Manufacturing Technology*, vol. 9, no. 6, pp. 1011-1019, 2019.

[30] H. Ahmed, J. Hyun, and J-Ryul. Lee, "Development of scanning single port free space measurement setup for imaging reflection loss of microwave absorbing materials," *Measurement*, vol. 125, pp. 114-122, 2018.

[31] T. Ozturk, A. Elhawil, I. Uluer, and M. T. Guneser, "Development of extraction techniques for dielectric constant from free-space measured S-parameters between 50 and 170 GHz," *J Mater Sci: Mater Electron* vol. 28, pp. 11543–11549, 2017.

[32] T. Ozturk, O. Morikawa, I. Ünal, and I. Uluer, "Comparison of free space measurement using a vector network analyzer and low-cost-type THz-TDS measurement methods between 75 and 325 GHz," *J Infrared Milli Terahz Waves*, vol. 38, pp. 1241–1251, 2017.

[33] C. E. Kintner, "Free-space measurements of dielectrics and three-dimensional periodic metamaterials," M.S. thesis, Dept. of Elect. Eng., Univ. of Arkansas, Fayetteville, AR, USA, 2017. Accessed on: Dec 19, 2017. [Online]. Available: https://scholarworks.uark.edu/etd/2557.

[34] Z. Akhter and M. J. Akhtar, "Free-space time domain position insensitive technique for simultaneous measurement of complex permittivity and thickness of lossy dielectric samples," *IEEE Transactions on Instrumentation and Measurement*, vol. 65, no. 10, pp. 2394-2405, 2016.

[35] A. M. Hassan, J. Obrzut, and E. J. Garboczi, "A Q-band free space characterization of carbon nanotube composites," *IEEE Trans. Microwave Theory & Tech*, vol. 64, no. 11, pp. 3807-3819, 2016.

[36] V. V. Varadan, K. A. Jose, and V. K. Varadan, "In situ microwave characterization of nonplanar dielectric objects," *IEEE Transactions on Microwave Theory and Techniques*, vol. 48, no. 3, pp. 388-394, 2000.

[37] F. C. Smith, B. Chambers, and J. C. Bennett, "Methodology for accurate free-space characterization of radar absorbing materials," *Proc. Inst. Elect. Eng.—Sci., Meas., Technol.*, vol. 141, no. 6, pp. 538–546, 1994.

[38] D. V. Blackham, "Free space characterization of materials," in *Proc. Antenna Meas. Techn. Assoc. Symp., vol. 15, pp. 58–60, 1993.*

[39] D. K. Ghodgaonkar, V. V. Varadan, and V. K. Varadan, “Free-space measurement of complex permittivity and complex permeability of magnetic materials at microwave frequencies,” *IEEE Trans. Instrum. Meas.*, vol. 39, no. 2, pp. 387–394, Apr. 1990.

[40] M. H. Umari, D. K. Ghodgaonkar, V. V. Varadan, and V. K. Varadan, “A free-space bistatic calibration technique for the measurement of parallel and perpendicular reflection coefficients of planar samples,” *IEEE Trans. Instrum. Meas.*, vol. 40, no. 1, pp. 19–24, Feb. 1991.

[41] V. V. Varadan, R. D. Hollinger, D. K. Ghodgaonkar, and V. K. Varadan, “Free-space, broadband measurements of high-temperature, complex dielectric properties at microwave frequencies,” *IEEE Trans. Instrum. Meas.*, vol. 40, no. 5, pp. 842–846, Oct. 1991.

[42] S. Chen, K. A. Korolev, J. Kupershmidt, K. Nguyen, and M. N. Afsar, “High-resolution high-power quasi-optical free-space spectrometer for dielectric and magnetic measurements in millimeter waves,” *IEEE Trans. Instrum. Meas.*, vol. 58, no. 8, pp. 2671–2678, 2009.

[43] G. L. Friedsam and E. M. Biebl, “A broadband free-space dielectric properties measurement system at millimeter wavelengths,” *IEEE Trans. Instrum. Meas.*, vol. 46, no. 2, pp. 515–518, Apr. 1997.

[44] Agilent Technologies, “Advanced calibration techniques for vector network analyzers,” *Modern Measurement Techniques for Testing Advanced Military Communications and Radars*, 2nd edn. Agilent Technologies, Inc. 2006.

[45] A. M. Nicolson and G. F. Ross, “Measurement of the intrinsic properties of materials by time-domain techniques,” *IEEE Trans. Instrum. Meas.*, vol. 19, pp. 377–382, 1970.

[46] J. Baker-Javis, M. D. Janezic, J. H. Grosvenor Jr., and R. G. Geyer, “Transmission/reflection and short-circuit line methods for measuring permittivity and permeability,” *NASA STIRecon Tech. Rep*. N 1992, 93, 12084.

[47] B.P. Singh, P. Bharadwaj, V. Choudhary, and R. B. Mathur, “Enhanced microwave shielding and mechanical properties of multiwall carbon nanotubes anchored carbon fiber felt reinforced epoxy multiscale composites,” *Appl Nanosci* vol. 4, pp. 421–428, 2014.

[48] D. R. Smith, D. C. Vier, Th. Koschny, and C. M. Soukoulis, “Electromagnetic parameter retrieval from inhomogeneous metamaterials,” *Phys. Rev. E*, vol. 71, no. 3, pp. 036617, 2005.

[49] N. Vohra, J. S. Batista, and M. El-Shenawee, “Characterization of radar absorbing materials at 75 GHz – 90 GHz using free-space system,” in *Proc. of IEEE-APS/URSI* 2020, Montreal, Quebec, Canada, 5-10 July 2020.

[50] V. V. Varadan and R. Ro, "Unique retrieval of complex permittivity and permeability of dispersive materials from reflection and transmitted fields by enforcing causality," *IEEE Trans. Microwave Theory & Tech*, vol. 55, no. 10, pp. 2224-2230, 2007.

[51] O. Luukkonen, S. I. Maslovski, and S. A. Tretyakov, "A stepwise Nicolson–Ross–Weir-based material parameter extraction method," in *IEEE Antennas and Wireless Propagation Letters*, vol. 10, pp. 1295-1298, 2011.

Appendix

Upon measuring the S-parameters, the time gating is implemented on the raw data. This feature in the network analyzer helps remove the post-calibration errors caused by the reflection of the sample's edge and load impedance mismatch due to any imperfection in the calibration standards. Here, we show the raw and gated data of S_{11} of the metal-backed reflection mode of sample P1, as an example, in Fig. 10. First, the inverse Fourier Transform of the frequency-domain S_{11} raw data is obtained, as sh own in Fig. 10. Then, the gating window is applied to the time-domain transformed data that include the main lobe and two side lobes. The gated time-domain data are transformed back to the frequency domain using the Fourier transform, as shown in the figure (red curve). An additional advantage of the gating is removing the noise. This procedure is applied to all S-parameters measured in this work.

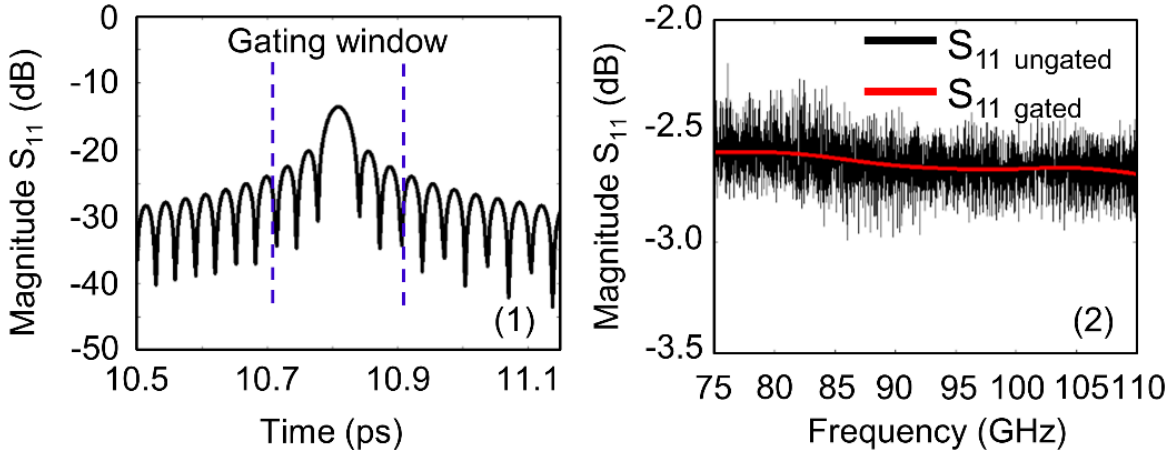

Fig. 10. Time-domain gating on S_{11} data of sample P1 obtained in W-band. (a) Inverse Fourier transformed time-domain S_{11} magnitude showing the applied gating window using the network analyzer gating feature. (b) Ungated (black solid line) and gated (red solid line) S_{11} magnitude (dB).

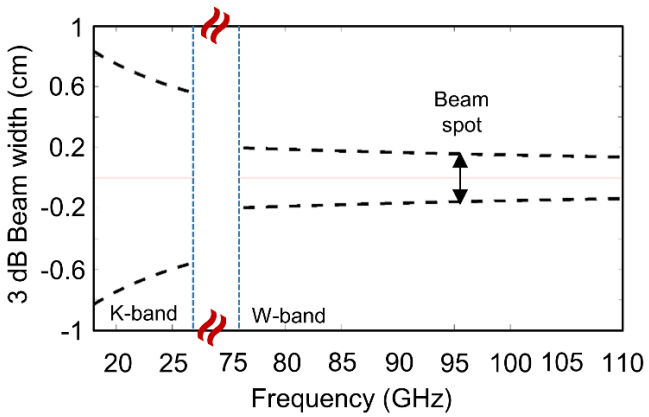

Fig. 11. A plot for 3-dB beamwidth of the incident beam on the sample under test across the whole *K*- and *W*-band.

The 3-dB beamwidth across the *K*- and *W*-bands is presented in Fig. 11, where the distance between the two dashed lines represents the beam spot diameter versus frequency, following the method at the *X*-band reported in [39].

CHAPTER 6

Conclusions

Over the course of this work, THz has proven effective in distinguishing between breast cancer tissue and healthy tissues in both FFPE and fresh tissue applications. Tumors obtained from humans and two different animal models—the transgenic mouse model and the Sprague Dawley rat model—are investigated in this work. The tumor inoculation process used in each animal model was different where transgenic mice produced tumors due to their genetic modifications; the rat model produced tumors upon ENU chemical injection in their mammary pad. The human breast cancer tumors involved freshly excised IDC cancer tumors obtained from NDRI biobank.

The experimental THz reflection imaging and transmission spectroscopy of freshly excised breast cancer tissue was obtained following the protocol detailed in Chapter 2 [1]. This protocol is designed according to the intraoperative time to image the excised tumor. To perform an effective THz reflection imaging on the freshly excised tumor, it is essential to dry the sample using grade 1 filter paper prior to the imaging to avoid false detection of cancer due to the presence of excess fluid. Additionally, it is crucial to ensure that the tumor is adequately placed on the polystyrene window, as poor tissue contact with the imaging window creates air bubbles underneath the tissue. These air bubbles cause spots of low reflection in the THz reflection image which ruins the imaging results.

Furthermore, for correct extraction of electrical properties of the tissues, additional considerations for the stage setup must be carefully implemented. An unbalanced scanning stage, even by a small fraction, can cause significant phase shifts in the measured data and thus affect the calculation of refractive index and absorption coefficient data of the tissue.

The work in Chapter 3 [2] expanded the THz reflection imaging applications to the freshly excised tumors obtained from transgenic mice. A total of fifteen tumors were excised from four

transgenic mice and were imaged following the THz reflection imaging protocol detailed in [1]. The freshly excised mouse model tumors and the corresponding FFPE block tissues were scanned using the THz scanner. The resulting images were compared against the low-power microscopic images of the pathology slides. In this work, almost all mice tumors represented advanced-stage cancer that infiltrated the surrounding normal tissues like fat and fibrous stroma. In some tumors, cancer became necrotic. Despite the aggressiveness of these tumors, they failed to represent significant fibroblast tissues surrounding the cancer, which we saw in our research on human breast tumors [1, 3]. Even though THz imaging of the transgenic mouse model tumors shows differentiation between the complex tissue regions, this model was not suitable for the overall goal of this study.

Therefore, another animal model study was conducted to continue the margin assessment investigation of breast cancer tumors [4]. In this work, the Sprague Dawley rat model was used to produce mammary tumors upon inoculation with an ENU chemical injection in their mammary pad. A total of 17 tumor sections were handled in this study obtained from nine tumors. The freshly excised tissue sections and their associated dehydrated FFPE block tissues were scanned on the imaging system to produce the THz images. The results obtained in this work highlighted the THz imaging reflection technique and the classified images obtained using the statistical expectation maximization (EM) classification algorithm. The obtained pathology images demonstrate that the ENU-tumors induced in rats exhibit the presence of healthy fibro-fatty tissues adjacent to cancer tissue similar to human breast cancer tumors. This similarity provided the motivation for this work, as the previously investigated xenograft [5, 6] and transgenic mouse [2] tumor models did not exhibit such resemblance with human breast tumors. The THz images of these tumors showed clear differentiation between cancerous and non-cancerous regions. This conclusion is also

supported by the EM model classification, where rat tumors represent a greater area under the ROC curve than the xenograft and transgenic mouse tumors.

Based on the obtained results in the investigation of margin assessment of tumors obtained from three different animal models, it can be concluded that the best animal model for breast cancer tumors is the ENU injected rat tumor model. While the xenograft and transgenic mouse models were utterly devoid of the fibroglandular tissue, the rat model closely mimicked human breast tumors by presenting healthy fibro-fatty tissues adjacent to cancer tissues [4].

In all cases, the THz imaging presented in the published works of this dissertation has shown to provide inherent contrast between cancer and healthy tissues in both fresh and FFPE block tumors. The THz imaging of FFPE block tissues shows strong agreement with the pathology images. However, it remains a challenge to correlate the fresh tissue image with the pathology image. The fresh tissue during the histopathology process undergoes shape and surface change, making the fresh tissue image not comparable to the pathology image. Additionally, due to the sectioning of tissue slices to get a flat surface for H&E stained pathology slides, the original surface of the fresh tissue is lost. This observation gravitate towards the animal model tumors. The animal model tumors tend to be soft and flexible as compared to the human breast cancer tumors. Because of which it is more likely for these tumors to undergo shape change during the histopathology process. Thus, another comparable method needs to be investigated, which can be used to compare the THz image at the same level.

Furthermore, from the THz imaging results of fresh tissues, a clear differentiation is seen between cancer and fat tissues, cancer and fibro-fatty tissues, and fibro-fatty and fat tissues. However, the primary challenge is determining and enhancing the contrast between pre-existing dense collagen and cancerous tissue. While these regions are seen to be clearly distinct in the

transmission spectroscopy results [7], the differentiation needs further enhancement in the tumor imaging.

One technique by which the contrast between cancer and collagen can be enhanced is by using optical clearing agents [8]. Optical clearing agents have been used in many imaging techniques at frequencies across the electromagnetic spectrum to improve the signal penetration inside the fresh biological tissues [9, 10]. One example of an optical clearing agent is glycerol. It is a biocompatible viscous solution, which is miscible with water and is hygroscopic in nature [11]. It is synthesized from glucose, and when it is introduced on fresh tissue, it binds to the structural protein in the tissue, which further affects the free-to-bound water ratio around the region of application. This affects the hydration of the tissue [9] and thus increases the signal penetration in the fresh tissue. Additionally, as observed in this work, the differentiation between cancer and collagen tissues is significantly observed in the FFPE block tissues due to its dehydration state. Therefore, in our pilot study to investigate the contrast enhancement between cancer and collagen tissues in human breast cancer tumors, we used glycerol as an optical clearing agent. The preliminary results of the glycerol-treated breast cancer tissues, presented in Appendix, show an enhancement in contrast between cancer and dense collagen tissue regions in the tumor [12]. Further investigation on this will help solve the biggest challenge when assessing surgical margins of the excised human breast cancer tumors.

To understand the interaction of the THz signal with breast cancer tumors the spectroscopy results obtained in [7] for cancerous and healthy breast tumors can be used to model the breast cancer tumors for computational simulations. The preliminary work done on this project is demonstrated in Appendix C in this dissertation. Together, the tissue handling experimental

methodology and FDTD model-based THz imaging can serve as a solid basis for developing THz as an intraoperative breast cancer application.

In the characterization of non-biological radar absorbing material samples in chapter 5 [14], we presented the results of the free-space measurements and novel characterization method for three highly conductive nonhomogeneous carbon-based RAM samples. To account for the system noise and error, a TRL system calibration was performed prior to the measurements of the samples in the K- and W-bands. The novel characterization method developed in this work is based on an iterative optimization model to extract the complex permittivity of unknown materials. The initial guess technique and the extraction algorithm presented in this work have successfully provided the correct relative permittivity of highly conductive samples (specifically, sample P3). The correctness of the extracted permittivity was validated by back calculating the S-parameters using the transmission line model [15] and comparing them with the measured S-parameters. When compared, the maximum error in the measured and computed S-parameters of all three samples was less than 1-dB. The future work on this project may involve the characterizing the magnetic radar absorbing materials in the W-band.

References

[1] N. Vohra, T. Bowman, K. Bailey, M. El-Shenawee, "Terahertz Imaging and Characterization Protocol for Freshly Excised Breast Cancer Tumors," *J. Vis. Exp.* issue. 158, e61007, 2020.

[2] N. Vohra, T. Bowman, P. M. Diaz, N. Rajaram, K. Bailey, M. El-Shenawee, "Pulsed terahertz reflection imaging of tumors in a spontaneous model of breast cancer," Biomedical Physics and Engineering Express, vol 4, no. 6, pp. 065025, 2018.

[3] M. El-Shenawee, T. Bowman, T. Esparza, K. Khan, J. Wu, A. Chakraborty, and K. Bailey, "Statistical Signal Processing For Quantitative Assessment Of Pulsed Terahertz Imaging Of Human Breast Tumors," 42nd International Conference on Infrared, Millimeter and Terahertz Waves, Cancun, Mexico, 27 August – 1 September 2017.

[4] N. Vohra, T. Chavez, J. Troncoso, N. Rajaram, J. Wu, P. Coan, T. A. Jackson, K.Bailey, M. El-Shenawee, "Mammary tumors in Sprague Dawley rats induced by N-ethyl-N-nitrosourea for evaluating terahertz imaging of breast cancer," *J. Med. Imag.* 8(2), 023504 2021.

[5] T. Bowman, T. Chavez, K. Khan, J. Wu, A. Chakraborty, N. Rajaram, K. Bailey, and M. El-Shenawee, “Pulsed terahertz imaging of breast cancer in freshly excised murine tumors,” J. Biomed. Opt., vol. 23, no. 2, pp. 026004, 2018.

[6] T. Chavez, T. Bowman, J. Wu, K. Bailey, and M. El-Shenawee, “Assessment of Terahertz Imaging for Excised Breast Cancer Tumors with Image Morphing,” J. Infrared Milli. Terahz Waves, vol. 39, no. 12, 1283–1302, 2018.

[7] T. Bowman, N. Vohra, K. Bailey, M. El-Shenawee, “Terahertz tomographic imaging of freshly excised human breast tissues,” *J. Med. Imag.* 6(2), 023501 (2019).

[8] G. R. Musina, A. A. Gavdush, D. K. Tuchina, I. N. Dolganova, G. A. Komandin, S. V. Chuchupal, O. A. Smolyanskaya, O. P. Cherkasova, K. I. Zaytsev, and V. V. Tuchin, "A comparison of terahertz optical constants and diffusion coefficients of tissue immersion optical clearing agents ," *Proc. SPIE 11065, Saratov Fall Meeting 2018: Optical and Nano-Technologies for Biology and Medicine*, 110651Z, 2019.

[9] O. A. Smolyanskaya, I. J. Schelkanova, M. S. Kulya, E. L. Odlyanitskiy, I. S. Goryachev, A. N. Tcypkin, Ya. V. Grachev, Ya. G. Toropova, and V. V. Tuchin, "Glycerol dehydration of native and diabetic animal tissues studied by THz-TDS and NMR methods," *Biomed. Opt. Express*, vol. 9, pp. 1198-1215, 2018.

[10] H. Q. Zhong, Z. Y. Guo, H. J. Wei, J. L. Si, L. Guo, Q. L. Zhao, C. C. Zeng, H. L. Xiong, Y. H. He and S. H. Liu, “Enhancement of permeability of glycerol with ultrasound in human normal and cancer breast tissues *in vitro* using optical coherence tomography,” *Laser Physics Letters*, vol. 7, no. 5, pp. 388-395, 2010.

[11] R. Christoph, B. Schmidt, U. Steinberner, W. Dilla, and R. Karinen, “Glycerol,” *Ullmann's Encyclopedia of Industrial Chemistry*, 2006.

[12] N. Vohra, K. Bailey, and M. El-Shenawee, “Dehydration Approach for Enhancing Terahertz Detection of Cancer in Freshly Excised Breast Tumors,” *Proc. of IEEE-APS/URSI* 2020, Montreal, Quebec, Canada, 5-10 July 2020.

[13] I. E. Pralea, R. C. Moldovan, A. B. Țigu, C. Ionescu, and C. A. Iuga, "Mass Spectrometry-Based Omics for the Characterization of Triple-Negative Breast Cancer Bio-Signature," *J. Pers. Med.*, vol. 10, no. 4, pp. 277, 2020.

[14] N. Vohra and M. El-Shenawee, “K- and W-Band Free-Space Characterizations of Highly Conductive Radar Absorbing Materials,” in IEEE Transactions on Instrumentation and Measurement, vol. 70, pp. 1-10, 2021, Art no. 8001910.

[15] A. M. Nicolson and G. F. Ross, “Measurement of the intrinsic properties of materials by time-domain techniques,” IEEE Trans. Instrum. Meas., vol. IM-19, no. 4, pp. 377–382, Nov. 1970.

APPENDICES

Appendix A: Dehydration Approach for Enhancing Terahertz Detection of Cancer in Freshly Excised Breast Tumors

Abstract

In this work we demonstrate the use of 60% concentration of glycerol solution as an optical clearance agent in freshly excised breast tissues. The research aims at enhancing the differentiation between cancer and collagen tissues using terahertz imaging technique. The terahertz reflection mode imaging is utilized in this work. The preliminary results demonstrated a potential contrast enhancement in the terahertz image between cancer and collagen tissues.

A.1. Introduction

Terahertz (THz) imaging has become an emerging technology for biomedical applications [1]. The technology has shown a significant promise in differentiating cancerous from non-cancerous tissues [2]. However, due to the high sensitivity of THz signal to water (or similar fluids), around 50% of the investigated fresh tissue samples showed success when compared with pathology. The challenge remains in differentiating cancer from collagen (connective healthy) tissues due to the presence of blood and other fluids in the samples [3].

A study using optical coherence tomography (OCT) imaging of breast cancer tissues has reported the use of glycerol as an optical clearing agent to enhance the image. The glycerol is a biocompatible viscous solution with absorption coefficient much smaller than that of water in the THz frequency range. It has been used as an optical clearing agent to enhance the penetration of

the optical light into biological tissues. The idea is treating the tissue with a clearing solution to increase the penetration depth of the optical signal [4]. The results reported in the literature showed OCT image enhancement upon treating the tissue with 60% concentration of glycerol solution [4]. Another study reported that monitoring THz signal in-vitro muscle tissue, upon dehydration using glycerol, showed the ability to form a free water flow out of the tissue, and hence increased the signal penetration [5].

A.2. Methodology

In this work we report the use of 60 % concentration of glycerol solution to investigate image enhancement of cancer in freshly excised human breast tumors in the THz reflection imaging method. The human breast cancer tissues handled in this work are obtained from the National Disease Research Interchange (NDRI) biobank, immersed in Dulbecco's Modified Eagle Medium (DMEM). The tissue was received within 24 hours of excision. Upon receiving the tissue, we dissected the sample into two halves as shown in Fig. 1a. It is to be noted, that when one half of the tissue is being scanned on the THz system, the other half is kept immersed in the DMEM solution to prevent drying the tissue in air.

The first half of the tissue was not treated with glycerol and is scanned using the configuration shown in Fig. 1b. The TPS Spectra 3000 pulsed THz imaging system (from TeraView Ltd, UK) is used to image the specimen following the procedure reported in [3]. The second half of the tissue is treated with the glycerol solution for 5 minutes as shown in Fig. 1. After immersing the tissue in glycerol, it was kept aside in a clean petri dish for ~ 50-55 minutes to allow the glycerol to be absorbed. The tissue is then placed on a filter paper for few minutes, in an upward position, to allow the appropriate absorption of the glycerol into the tissue. The tissue is then scanned using the same configuration of the untreated tissue. The THz reflection mode is used in

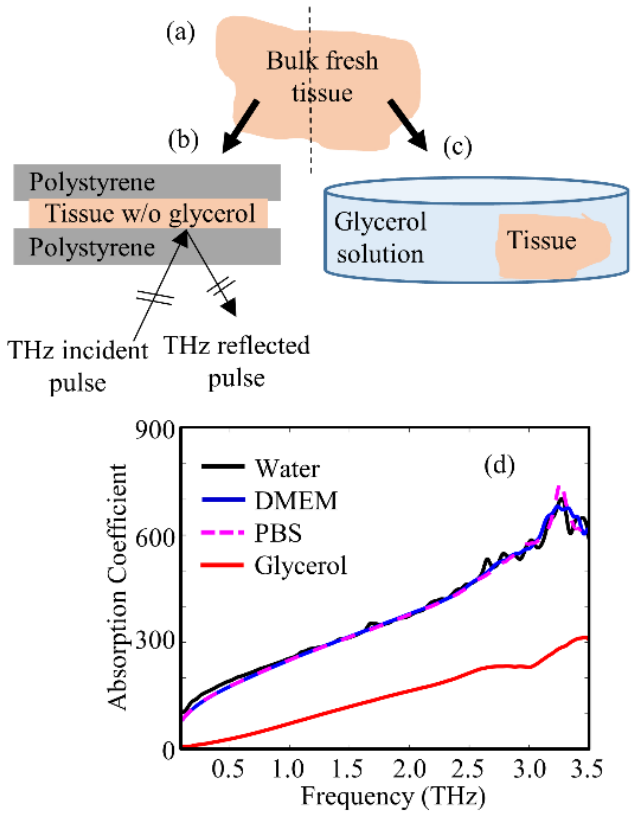

Fig. 1 Schematic diagram of the sample preparation for THz imaging. (a) Bulk tissue dissected into two halves, (b) THz reflection mode configuration using untreated tissue sandwiched between two polystyrene plates, (c) the second half of the tissue is immersed in glycerol solution placed in a petri dish, (d) the absorption coefficient plots of glycerol, DMEM, water, PhosphateBuffered Saline (PBS) solutions versus frequency

the imaging procedure where the tissue was placed between two polystyrene plates as shown in Fig. 1b. The absorption coefficient of glycerol is shown to be much smaller than other solution such as water, DMEM, and Phosphate-Buffered Saline (PBS) as shown in Fig. 1d.

Upon completing the imaging procedure, the tissues are immersed in formalin solution and sent to the Oklahoma Animal Disease Diagnostic Laboratory (OADDL) for pathology process. The formalin fixed paraffin embedded (FFPE) block tissue are then imaged using THz reflection mode. The images are validated with the pathology (microscopic) images.

A.3. Experimental Results

The results in Fig. 2 represent THz and pathology images of the dissected halves of the ND18228 sample. This tumor was obtained from a 70 years old female via mastectomy. The pathology and THz images shown in Fig. 2a and 2b, respectively, corresponds to the ND18228-1 which is not treated with glycerol. Whereas, the results in Fig. 2c and 2d corresponds to ND18228-2 which is treated with 60% concentration of glycerol solution applied for a total of ~ 60 minutes. The 60% concentration of the solution is obtained using a well-known dilution formula, $C_1V_1 = C_2V_2$, where C_1 is the original concentration (100 %) of the glycerol solution, V_1 is the volume of the original solution required to obtain the required volume V_2 of concentration C_2.

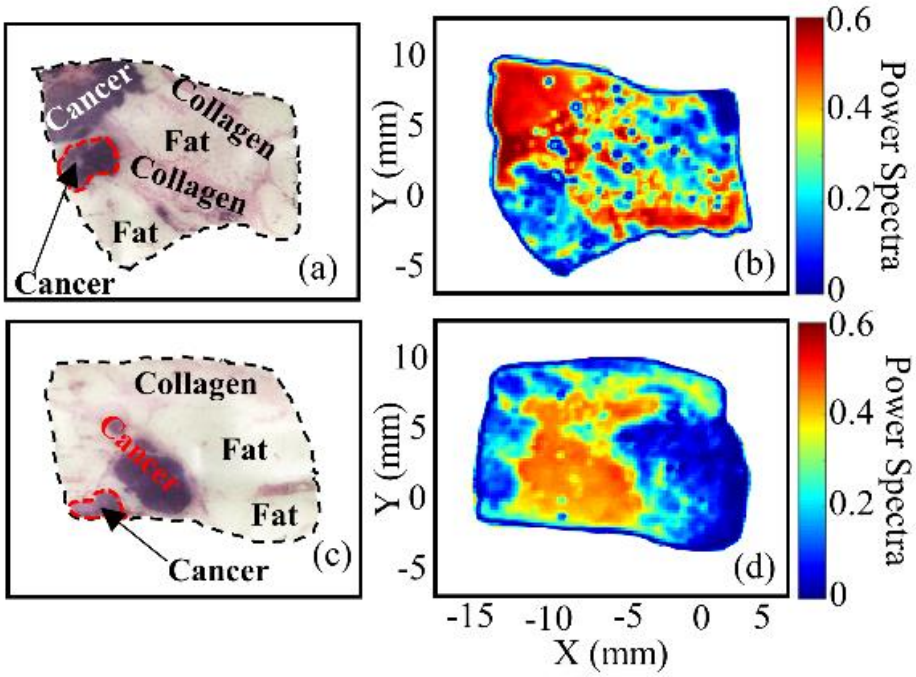

Fig. 2 THz reflection imaging of a freshly excised human breast cancer tissue # ND18228. (a) The low power pathology image of one half of the bulk tumor (ND18228-1) which is not treated with glycerol solution, (b) The frequency domain THz image of the tumor in (a) represented in spectral power, (c) The low power pathology image of the second half of the bulk tumor (ND18228-2) which is treated using 60% concentration of glycerol solution for 60 minutes prior to the imaging, (d) The frequency domain THz image of the tumor in (c) represented in spectral power. All spectral power values are obtained upon integrating the frequency domain THz signals over the range from 0.5 THz to 1.0 THz.

The THz results in Fig. 2 are obtained using the power spectra over the frequency range from 0.5 THz to 1 THz as reported in [3]. Upon comparing the THz image in Fig. 2b with the pathology image in Fig. 2a, a noticeable differentiation can be seen between cancer (red color) and fat (blue) regions. Furthermore, a significant differentiation is observed between cancer (red color) and fibro-fatty (cyan color) regions. However, the differentiation between cancer and collagen is not clearly observed. Both of the regions show high reflections (red color) in the THz image color bar. It is to be noted that the blue circular dots around the caner region in the THz image in Fig. 1b are due to air bubbles between the tissue and the polystyrene plate.

The result of Fig. 2d represents the THz spectra image of the ND18228-2 tissue, also obtained over the frequency range from 0.5 THz to 1 THz. Upon comparing the THz image with the pathology image in Figs. 2d and Fig. 2c, respectively, a good differentiation can be observed between cancer (red color) and collagen region (yellow-blue color). It is also observed that the reflection values from cancer in Fig. 2d are lower than those in Fig. 2b (see the color bar). This is because the untreated tissue in Fig. 2b has more fluid content compared with that of the treated tissue in Fig. 2d. This means that the percentage of fluid content in both cancer and collagen was comparable in Fig. 2b, while treating the tissue with the glycerol solution has led to push away the fluids from the tissue. These results demonstrate the potential of using glycerol solution for enhancing THz imaging. Ongoing research aims at investigating the use of optical clearing solutions of various concentrations and time durations.

Acknowledgement

We acknowledge the NDRI for providing breast tissues, with support from the NIH grant U42OD11158. We appreciate the collaboration with the OADDL for conducting the histopathology procedure of tissues.

References

[1] Q. Sun, Y. He, K. Liu, S. Fan, E. P. Parrott, and E. Pickwell-MacPherson, "Recent advances in terahertz technology for biomedical applications," *Quantitative imaging in medicine and surgery, vol. 7, no. 3*, pp. 345-355, 2017.

[2] M. El-Shenawee, N. Vohra, T. Bowman, K. Bailey,"Cancer detection in excised breast tumors using terahertz imaging and spectroscopy," *Biomedical Spectroscopy and Imaging*, vol. 8, no. 1-2, pp. 1-9, 2019.

[3] T. C. Bowman, N. Vohra, K.Bailey, M. El-Shenawee, "Terahertz tomographic imaging of freshly excised human breast tissues," *J. Med. Imag.*, vol. **6, no.** 2, pp. 023501, 2019.

[4] H. Q. Zhong, Z. Y. Guo, H. J. Wei, J. L. Si, L. Guo, Q. L. Zhao, C. C. Zeng, H. L. Xiong, Y. H. He and S. H. Liu, "Enhancement of permeability of glycerol with ultrasound in human normal and cancer breast tissues *in vitro* using optical coherence tomography," *Laser Physics Letters*, vol. 7, no. 5, pp. 388-395, 2010.

[5] A. S. Kolesnikov, E. A. Kolesnikova, A. P. Popov, M. M. Nazarov, A. P. Shkurinov, and V. V. Tuchin, "In vitro terahertz monitoring of muscle tissue dehydration under the action of hyperosmotic agents," *Quantum Electronics*, vol. 44, no. 7, pp. 633-640, 2014.

Appendix B: Imaging Breast Ductal Carcinoma In Situ (DCIS) using Pulsed Terahertz Spectroscopy System

Abstract

This work proposes the use of terahertz (THz) reflection imaging method for investigating breast ductal carcinoma in situ (DCIS). The tumor handled in this work is formalin fixed and paraffin embedded tissue block (FFPE). The goal of this research is to differentiate between DCIS and invasive ductal carcinoma (IDC). In the previous research, THz spectroscopy has shown successful differentiation between cancerous (IDC) and normal breast tissue in freshly excised tumors. The study conducted on IDC has demonstrated interesting signatures in the absorption coefficient of cancer tissues. Similar studies will be conducted in this work for FFPE tissue blocks to investigate the potential invasiveness level of DCIS tumors.

B.1. Introduction

Ductal carcinoma in situ (DCIS) is considered the earliest form of breast cancer, where abnormal cells replace the normal epithelial cells that line the breast ducts. Currently about 20% of breast cancers diagnosed in the United States are DCIS with an overall 10-24% risk of progression to invasive breast cancer within 10 years [1]. Advances in screening techniques have increased the detection rate of DCIS incidence, but for comedo DCIS, a subtype that is considered particularly aggressive and requires treatment, the detection rate has not increased as rapidly as for the less aggressive forms which can remain untreated [2]. Many of the key risk factors, methods of detection and prevention techniques for DCIS are similar to those of invasive breast cancer such as age, race, family history, breast density, chemoprevention (e.g. tamoxifen), and mammography,

but the challenge exists in determining which DCIS cases should be treated and which ones to be left alone [2, 3].

Terahertz (THz) has been a growing area of research, especially in the biomedical field, since the advent of reliable THz sources [4]. Several investigations have been made using THz imaging and spectroscopy of freshly excised breast cancer tissue that has shown inherent distinction between cancer and normal tissue [5]. An interesting observation has been made in the ongoing research of our group where the transmission spectroscopy absorption coefficient results of freshly excised cancer tissue show a peak in the frequency band of 3-3.5 THz. The peak was observed around the same frequency band in all freshly excised IDC cancerous tissue samples that were examined in the study. On the other hand, a less significant trend for peaks is observed in collagenous (connective) tissues and no peaks were observed in the fatty tissues [5]. This technique could be a potential method for identifying signatures in DCIS tumors to help investigate its grade.

In this work we present the THz reflection imaging of FFPE tissue block of DCIS tumor. The results provide successful differentiation between DCIS and other adjacent non-cancerous tissues in the same tumor.

B.2. Methodology

The formalin fixed paraffin embedded DCIS tissue blocks used in this work are obtained from the National Disease Research Interchange (NDRI) biobank. Upon receiving the tissue block in the Terahertz Lab at the University of Arkansas, the reflection imaging is performed using the same procedure detailed in [6]. The TPS Spectra 3000 pulsed THz imaging system (from TeraView Ltd, UK) is used to perform the reflection mode scanning of the block tissue [6]. The imaging stage is set to be moved in increments of 200 μm using stepper motors to obtain the time domain reflection data at each pixel on the tissue. The maximum peak of the acquired reflected

data at each pixel is used to construct the time domain THz image. Upon completing the imaging procedure, the tissue block is sent to the Oklahoma Animal Disease Diagnostic Laboratory (OADDL) for pathology process. During the pathology process, a 3-4 μm thick tissue section is sliced from the surface of the block, the slice is stained with hematoxylin and eosin (H&E), and a pathology slide is obtained. The microscopic image of the pathology slide is then used to correlate THz image with pathology image.

B.3. Experimental Results

The results in Fig. 1 represent the THz image of the FFPE DCIS block tissue obtained from a 46 years old female via right breast mastectomy. According to the pathology report, the tissue shown in Fig. 1 is diagnosed as high-grade DCIS. The low power pathology image of the corresponding FFPE block tissue is shown in Fig. 1a.

THz image constructed based on the maximum peak of the reflected time domain data at each pixel is shown in Fig. 1b. The colorbar in the image represents the amplitude of the electric field in the time domain normalized with respect to that reflected from a gold mirror. The time domain plots in Fig. 1c show the reflected THz electric field pulse at selected pixels ①-⑤ shown in Fig. 1a. The high-power pathology images of Fig. 1d show the neighborhood of points ①-⑤. Upon comparing the THz image in Fig. 1b with the low power pathology image in Fig. 1a, we can see that the good correlation with the pathology image. Furthermore, the THz image in Fig. 1b demonstrates that DCIS show higher reflections (red color regions) than the dense collagen with mammary ducts (yellow- light red color regions) and the fibrofatty (cyan color regions). This differentiation can also be observed in the THz time domain reflected signals plotted in Fig. 1c. The higher reflection is observed from the DCIS pixels ② and ③ compared with the dense collagen regions with mammary ducts and glands ① and ④, followed by the lowest reflection

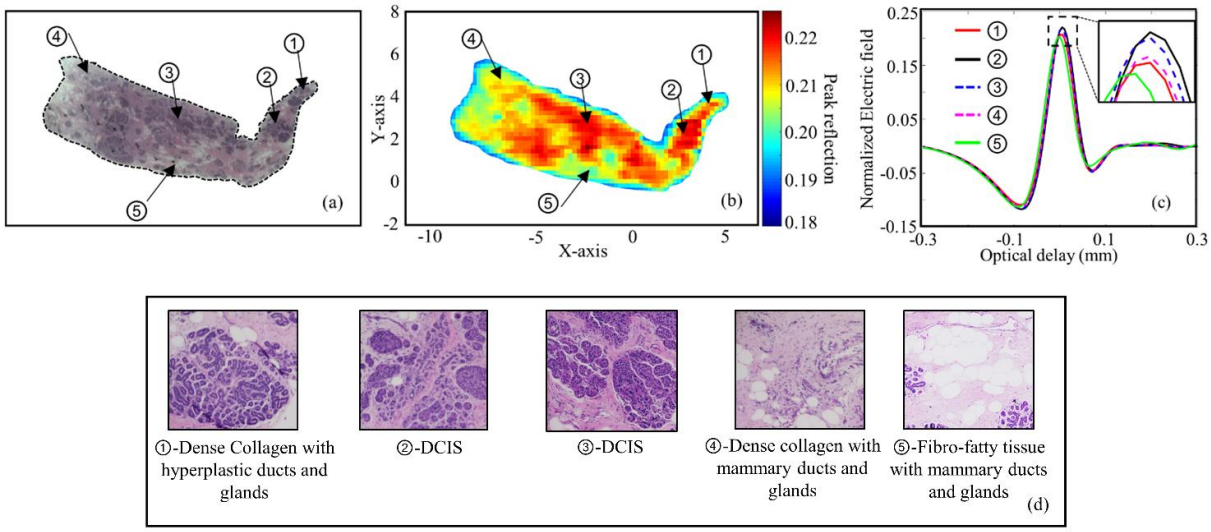

Fig. 1 THz reflection imaging of a formalin fixed paraffin embedded DCIS tissue block. (a) The low power pathology image, (b) The time domain THz image of FFPE tissue block represented by maximum peak value, (c) The time domain reflected electric field signals at selected pixels ①-⑤ shown in (b), (d) The high power pathology images of the surrounding regions corresponding to each selected point in (a).

from fibro-fatty regions ⑤. However, it is to be noted that in Fig. 1c insignificant differentiation can be observed between ② and ③ pixel plots, which is consistent with both being DCIS. This insignificant difference could be due a difference in the density of cancer cells enclosed in the scanned pixels. The observation applies to pixel plots of① and ④, where both represent dense collagen with mammary glands and ducts. The results demonstrate potential differentiation between DCIS and adjacent non-cancerous tissues in the FFPE block tissue using THz imaging. Depending on the outcome results of THz investigation of FFPE DCIS tissue blocks, the research will be expanded to use freshly excised DCIS tumors in animal and/or human models.

Acknowledgement

We acknowledge the use of tissues procured by the National Disease Research Interchange (NDRI) with support from the NIH grant U42OD11158. We also acknowledge the collaboration

with Oklahoma Animal Disease Diagnostic Laboratory at the Oklahoma State University for conducting the histopathology procedure on all the tissues handled in this work.

References

[1] Cancer Facts and Figures 2015, "Special Section: Breast Carcinoma In Situ," pp. 26-36, 2015.

[2] B. A. Virnig, T. M. Tuttle, T. Shamliyan, R. L. Kane, "Ductal carcinoma in situ of the breast: a systematic review of incidence, treatment, and outcomes," J. National Cancer Institute, vol. 102, no. 3, pp. 170-178, 2010.

[3] I. Schmale, S. Liu, J. Rayhanabad, C. A. Russell, S. F. Sener, "Ductal carcinoma in situ (DCIS) of the breast: perspectives on biology and controversies in current management," J. Surg Oncol, vol. 105, no. 2, pp. 212-20, 2012.

[4] N. M. Burford, M. J. Evans, and M. El-Shenawee, "Plasmonic Nanodisk Thin-Film Terahertz Photoconductive Antenna," IEEE Trans. on Terahz. Sci. and Tech. vol. 8, no. 2, p. 237-247, 2018.

[5] T. C. Bowman, N. Vohra, K.Bailey, M. El-Shenawee, "Terahertz tomographic imaging of freshly excised human breast tissues," J. Med. Imag., vol. 6, no. 2, pp. 023501, 2019.

[6] T. C. Bowman, M. El-Shenawee, and L.K. Campbell. "Terahertz Imaging of Excised Breast Tumor Tissue on Paraffin Sections." IEEE Trans. on Ant. and Propag. vol. 63, no. 5, pp. 2088-2097, 2015.

Appendix C: Finite-Difference Time-Domain Method for Modeling the Interaction of Terahertz Waves with Human Breast Cancer Tumors

C1. Motivation

The motivation for this work arises from a study conducted, in the THz lab at the University of Arkansas, for the in-depth imaging of FFPE block tissues. The FFPE block tissues handled in that study were human breast cancer metastasized lymph node tissues. The goal of that study was to investigate THz in-depth imaging of metastasized tumors and compare it with the THz imaging of the IDC tumors. The in-depth imaging on the block tissues is performed by following the procedure defined in [1]. However, the results obtained from the in-depth imaging were not encouraging. Except for the THz image obtained at the surface of the block, no image obtained at various depths inside the block tissue present differentiation between different regions in the tissue. This could be primarily due to the interference caused by the multiple reflections from the surrounding tissues. Thus, the constructed image did not present the correct results when compared against the pathology at the same depth of the imaging. The results of one of the FFPE tumors

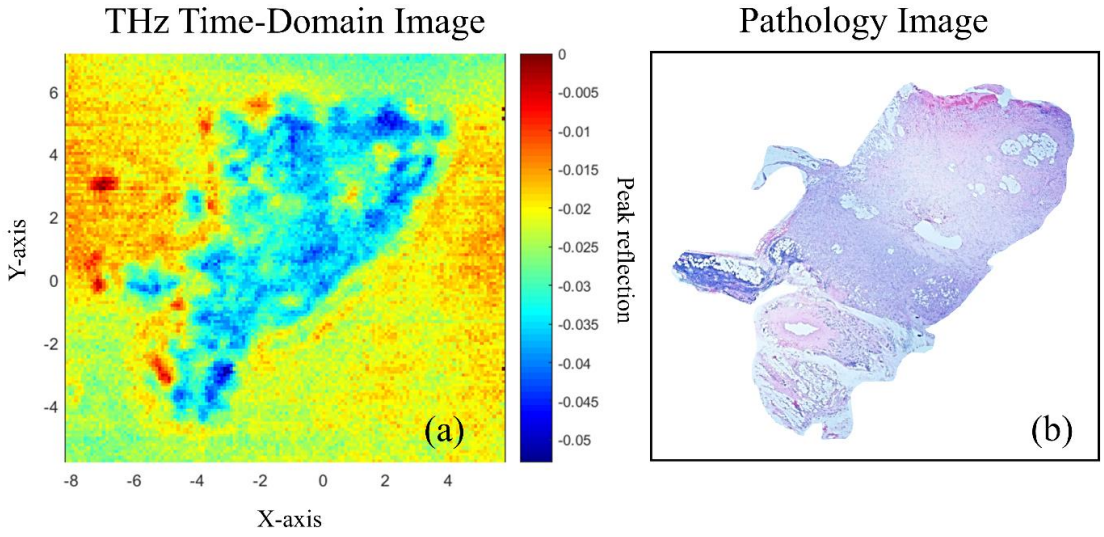

Fig. 1. (a) THz in-depth image of a lymph node metastasized sample S10-17840, obtained at 180 µm from the sample surface, constructed using the peak reflection magnitude at each pixel, (b) Low power pathology image of lymph node metastasized sample S10-17840.

imaged in this work are presented in Fig. 1. The image in Fig. 1a represents the in-depth image of block sample S10-17840 obtained at 180 µm below the sample surface. The image in Fig.1b represents the pathology image of the tissue slice taken at 180 µm below the block surface after the in-depth scanning was already performed. Upon comparing the two images, we can see that the tissue shape is very easily predictable from the THz image; however, the details in the tissue regions are not captured in the image. Additionally, the reflections on the tissue edges, in the paraffin regions, are very dominant; primarily due to the multiple reflections in the sample and edge effects. Therefore, to better understand the physics behind the signal interaction with the block sample in Z-scan imaging, we shifted the focus of this study on the tissue modeling, which is discussed in the following Sections.

C2. Objective

In order to quantify the signal interference challenges faced over the THz in-depth imaging of FFPE block tissues, this work will demonstrate the modeling and simulations performed using a python based Finite-Difference Time-Domain (FDTD) software.

C3. Software Introduction

The software used in this work is a free and an open-source software package called Meep. The name Meep is an acronym for MIT Electromagnetic Equation Propagation. This software is specifically designed for electromagnetic simulations using the finite-difference time-domain (FDTD) method for a wide range of the applications. FDTD is a widely used technique for the electromagnetic simulations in which the space to be simulated is divided into discrete grid cells, called Yee cells and the fields are progressed in time using discrete time steps. Meep provides libraries for inbuilt functions scripted in Python interface, C++ interface, and Scheme interface. It allows the users to perform simulations in 1D, 2D, 3D, and cylindrical coordinates. The complete

manual on the MEEP software package with multiple tutorials on different applications to practice can be found in [2]. The software installation guide is provided in [3], and the software version are provided in [4] for download. All the technical details for Meep's inbuilt functions are provided in [5, 6]. The developers update the software every few months and with each update a new version of the software is released. In this work, we downloaded and installed the January 2021 v1.17.1 version of the software.

C4. MEEP Model Considerations

To define the model in Meep, there are some basic FDTD parameters that are defined in a different way in the Meep software than the original formulation. These changes in the parameter definition need to be considered and applied appropriately in order to achieve satisfactory results.

C4.1. MEEP Units

Meep uses dimensionless units where anything a user want to compute is expressed as a ratio. That means, it defines a characteristic length scale 'a' and uses that as the unit of distance. Since Maxwell's equations are scale invariant, it is convenient in electromagnetic simulations to choose a scale-invariant unit. Additionally, the default value of the speed of light in vacuum (c) is defined as 1 in Meep units. Therefore, the frequency, f, in Meep is specified in units of c/a.

C4.2. Courant Factor

For a given spatial resolution, Δx, the discrete time step Δt in Meep is defined as Δt = S*Δx, where S is called the courant factor and

$$\Delta x = \frac{\lambda_{min}}{(No.of\ cells\ per\ wavelength)}$$

For optimum resolution, the no. of cells per wavelength should be greater than or equal to 10. For numerical stability, $S < \frac{n_{min}}{\sqrt{\#\ of\ dimensions}}$ where n_{min} is the minimum refractive index of the medium [6]. The default value of S used by Meep is 0.5, but it can be defined by the user as

required. Furthermore, it is important to note that Meep does not support non-uniform discretization of the computational cell.

C4.3. Boundary Conditions

In FDTD, only a finite region is simulated, thus there should be a way to terminate the simulations beyond that finite region. The way to do this is by applying boundary conditions. Meep supports three different types of termination methods—Bloch-periodic boundaries, metallic walls, and PML absorbing layers. Meep also allows the utilization of symmetries of a problem to reduce the computational time and memory requirements.

C5. Breast Cancer Tumor Model Configuration

C5.1. Geometry and Material Properties

In this work, we developed a 3D model in Meep that demonstrate an irregular shaped tissue constructed in the shape of the human breast cancer tumor ND14139 [7], as shown in Fig. 2. The size of the tissue geometry simulated in this work is (2.8 x 2.8 x 0.5) mm^3. As shown in Fig. 2, the tissue geometry demonstrates three different mediums—cancer, collagen, and fat. To assign the material properties to these three regions in the geometry, the relative permittivity of the cancer, collagen, and fat obtained in [7] are utilized. In this work, the material properties are defined at

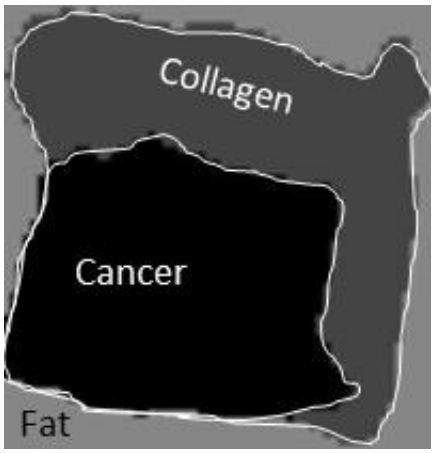

Fig. 2. The configuration of the human breast tumor model geometry.

only one frequency, which is 1 THz. Therefore, at 1 THz the relative permittivity used in this work for cancer is [4.411 + j1.69], for collagen is [4.196 + j1.554], and for fat is [2.455 + j0.2786].

C5.2. User Defined Custom Source and Other Parameters

Meep allows the users to custom-build the time domain source and combine it with the Gaussian beam source in space. In fact, Meep is the only available FDTD software package that provides the users with this function. In this work, we utilized the incident THz experimental time-domain pulse data with the Gaussian beam source in space. This combination of the sources is used as the excitation source for the FDTD computations. At this point, in this work the Gaussian beam source is defined at 1 THz frequency with a beam spot radius equals to ~0.7 mm, which is similar to what is provided by the experimental THz pulse. Therefore, to have the converging computational solution, the grid resolution is defined at 1 THz frequency as well. Furthermore, for boundary condition, the PML absorbing layer is defined at a thickness of 2*λ m, where λ is calculated at 1 THz frequency in air.

C5.3. Tumor Scanning Process

In the model configuration defined in Fig. 3, the source is placed at the upper PML boundary (in the Z-direction), with the center defined at (0, 0, Zsize/2), where the Zsize = 1.55 mm, and the tumor geometry surface is placed at 2.5* λ m below the source. It is to be noted, that the size of the computational cell for this model is (2.8 x 2.8 x 1.55) mm^3, as shown in Fig. 3. The normal incidence THz signal is focused on the surface of the geometry and the total electric field reflected from the tumor surface is collected back at the source center. This collected electric field data has both incident and reflected signals shifted in time. Therefore, another simulation is performed in an empty air box without the tissue geometry to collect the incident electric field data

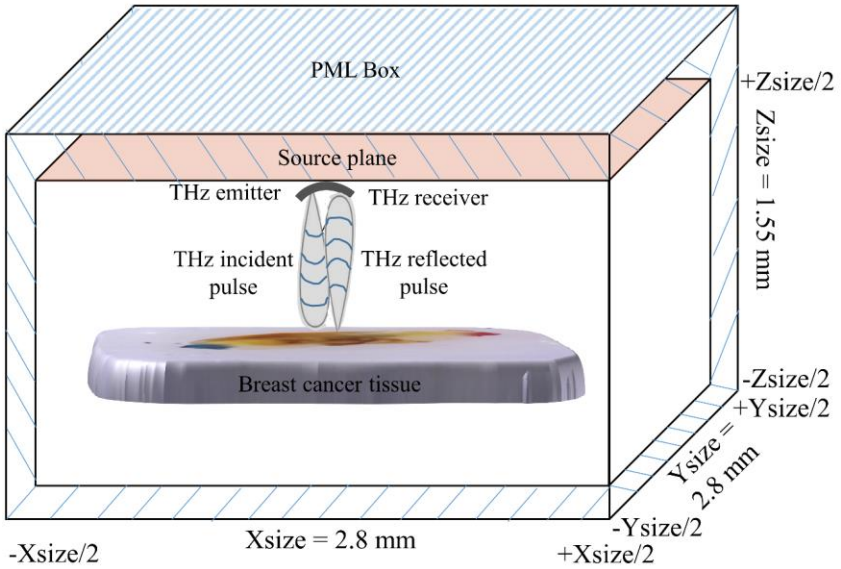

Fig. 3. The configuration of the computational domain for the THz in-depth modeling.

at the source center. This incident electric field data is then subtracted from the total electric field data to obtain the scattered electric field corresponding to the reflections from tumor surface.

To mimic the THz experimental scanning process performed on the tumors, the simulations at several points on the tumor surface, equally separated in the computation domain at 100 µm step size, were performed. That means for a computational cell of size (2.8 x 2.8) mm^2, a total of 29 x 29 scanning points were defined, i.e., for 841 times simulations were performed. These 841 simulations were first performed serially on an Intel Xeon Silver 4110 8-core CPU with 128 GB system memory, running on CentOS 7; the total execution time it took to complete 841 simulations was ~ 3 days.

Therefore, to reduce the total execution time in performing tumor scanning, a multiprocessing based parallel code was constructed such that the simulations at each point on the tissue geometry were performed independently on multiple computers at the same time. This type of parallelization approach is called the embarrassingly parallel method because no communication is required between different processes assigned to different computers.

To accomplish the parallel processing, we worked in collaboration with the Arkansas High Performance Computing Center (AHPCC) at the University of Arkansas. We utilized a single node with 32 cores in the comp 72 partition to perform these simulations simultaneously. The total execution time for the whole simulation was reduced from 3 days to ~ 4 hours upon implementing the parallel computing technique.

C6. Simulation Results and Discussions

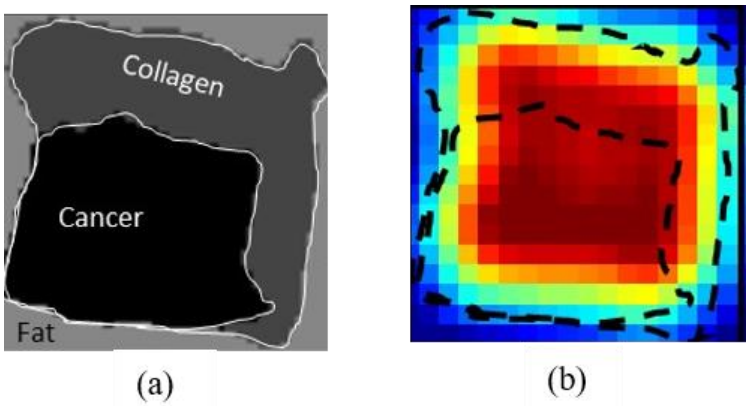

Fig. 4. (a) The configuration of the human breast cancer tumor model geometry, (b) the image constructed from the reflected electric field data simulated for the geometry in (b).

The simulated scanning image of the defined tumor geometry, as shown in Fig. 4a, obtained in this work is shown in Fig. 4b. As can be seen, that the cancer region (dark red color) represents a higher reflection magnitude than the fat region (blue color). The differentiation between the cancer and collagen tissue can also be visualized but not as prominent as between cancer and fat. Furthermore, the interface boundaries between the three regions are not clearly defined in the resulting image, which needs to be addressed in the future work of this project.

These are preliminary results and research continues to improve the resolution of the computer simulations in order to see clear margins between the three regions in the tumor. The future work will specifically be focused on:

1. Improving the excitation source so that it provides the varying beam spot size at each frequency of the THz signal.
2. Defining the tissue properties at all the frequencies covered in the THz time domain pulse, using the Lorentz susceptibility model or Lorentz Drude model compatible with Meep.
3. Performing simulations with the source positioned at an oblique angle of 30°.

References

[1] T. Bowman, Y. Wu, J. Gauch, L. K. Campbell, and M. El-Shenawee, "Terahertz Imaging of Three-Dimensional Dehydrated Breast Cancer Tumors," *J. Infrared Milli. Terahz Waves*, vol. 38, no. 6, pp. 766-786, 2017.

[2] https://meep.readthedocs.io/en/latest/

[3] https://meep.readthedocs.io/en/latest/Installation/

[4] https://github.com/NanoComp/meep/releases

[5] A. F. Oskooi, D. Roundy, M. Ibanescu, P. Bermel, J.D. Joannopoulos, S. G. Johnson, "Meep: A flexible free-software package for electromagnetic simulations by the FDTD method," *Computer Physics Communications*, vol. 181, no. 3, pp. 687-702, 2010.

[6] S. Johnson; A. Oskooi; A. Taflove, *Advances in FDTD Computational Electrodynamics: Photonics and Nanotechnology* , Artech, 2013.

[7] T. Bowman, N. Vohra, K. Bailey, and M. El-Shenawee, "Terahertz tomographic imaging of freshly excised human breast tissues," *J. Med. Imag.*, vol. 6, no. 2, 023501, 2019.

Appendix D: Video Tutorials for Terahertz TPS Pulse Spectra 3000 System

The videos were developed in the Terahertz Imaging and Spectroscopy Computational Electromagnetics Lab at the University of Arkansas in May 2021, under the supervision of Dr. Magda El-Shenawee, by Nagma Vohra. The video recordings and edits are provided by Jose Santos Batista.

The following videos provide the user with complete training on the imaging and spectroscopy procedures performed using the Terahertz Imaging and Spectroscopy core and gantry systems at the University of Arkansas.

The sequence of the videos for the training is provided as follows:

1. TPS Spectra3000 – Overview – Final
2. TPS Spectra3000 – Modelocked – Final
3. TPS Spectra3000 – Transmission Spectroscopy – Final
4. TPS Spectra3000 – Transmission Imaging – Final
5. TPS Spectra3000 – Block Tissue Reflection Imaging – Final
6. TPS Spectra3000 – In-Depth Reflection Imaging – Final
7. TPS Spectra3000 – Fresh Tissue Reflection Imaging – Final
8. TPS Spectra3000 – Gantry System – Final
9. TPS Spectra3000 – Gantry System Leveling – Final

Appendix E: Video Tutorials for Microwave and Millimeter-wave Free-Space System

The videos were developed in the Microwave and Millimeter-wave Free-Space Lab at the University of Arkansas in April 2021, under the supervision of Dr. Magda El-Shenawee, by Nagma Vohra. The video recordings and edits are provided by Jose Santos Batista.

The following videos provide the user with complete training on the microwave and millimeter-wave system calibration and measurements in transmission and reflection modes, using the non-destructive Free-Space System at the University of Arkansas.

The sequence of the videos for the training is provided as follows:

1. Introduction to the Free Space System – Final
2. Free Space System – Cable Connections – Final
3. Measurements Operations – Overview – Final
4. Measurements operations – Calibration – Final
5. Measurements Operations – Measurements – Final

Appendix F: Protocol approved by Animal Care and Use Committee Institution

UNIVERSITY OF ARKANSAS

Office of Research Compliance

To:	Narasimhan Rajaram
Fr:	Craig Coon
Date:	January 17th, 2018
Subject:	IACUC Approval
Expiration Date:	December 19th, 2019

The Institutional Animal Care and Use Committee (IACUC) has APPROVED your protocol # **18063:** *Terahertz imaging for breast cancer margin assessment*.

In granting its approval, the IACUC has approved only the information provided. Should there be any further changes to the protocol during the research, please notify the IACUC in writing (via the Modification form) prior to initiating the changes. If the study period is expected to extend beyond December 19th, 2019 you can submit a modification to extend project up to 3 years, or submit a new protocol. By policy the IACUC cannot approve a study for more than 3 years at a time.

The following individuals are approved to work on this study: Narasimhan Rajaram, Tyler Bowman, Magda El-Shenawee, Christopher Oldfield, Nagma Vohra, and Paolo Monterroso-Dia. Please submit personnel additions to this protocol via the modification form prior to their start of work.

The IACUC appreciates your cooperation in complying with University and Federal guidelines involving animal subjects.

CNC/tmp

18063